Universidad Autónoma de Querétaro

Facultad de ingeniería

Desarrollo de sistema HIL de potencia para la emulación de máquinas eléctricas rotativas

Tesis

Que como parte de los requisitos para obtener el grado de:

Doctorado en Mecatrónica

Presenta:

Arturo Mejía Barrón

Dirigido por:

Dr. Martín Valtierra Rodríguez

Dr. David Granados Lieberman

San Juan del Río, Qro. Febrero 2019

Universidad Autónoma de Querétaro
Facultad de Ingeniería
Doctorado en Mecatrónica

Desarrollo de sistema HIL de potencia para la emulación de máquinas eléctricas rotativas

Tesis

Que como parte de los requisitos para obtener el Grado de
Doctorado en Mecatrónica

Presenta:
M. en C. Arturo Mejía Barrón

Dirigido por:
Dr. Martín Valtierra Rodríguez
Co-dirigido por:
Dr. David Granados Lieberman

Dr. Martin Valtierra Rodriguez — Firma
Presidente

Dr. David Granados Lieberman — Granados Lieberman D.
Secretario — Firma

Dr. Roque Alfredo Osornio Rios — Firma
Vocal

Dr. René de Jesús Romero Troncoso — Firma
Suplente

Dr. Luis Morales Velázquez — Firma
Suplente

Loarca

Dr. Manuel Toledano Ayala
Director de la Facultad

Dra. Ma. Guadalupe Flavia Loarca Piña
Directora de Investigación y Posgrado

Centro Universitario
Querétaro
Febrero, 2019

RESUMEN

La simulación PHIL (por sus siglas en inglés, Power Hardware-in-the-Loop) representa una herramienta versátil, segura y de bajo costo, la cual permite emular el comportamiento eléctrico de diferentes componentes o sistemas eléctricos con la finalidad de generar un entorno seguro de pruebas para validación de dispositivos de control, desarrollo de prototipos y análisis con fines de investigación científica. Aunado a esto el análisis de máquinas eléctricas rotativas representa una importante área de interés para investigadores y el sector industrial ya que gran parte de la energía generada a nivel mundial es consumida por motores, además, el desarrollo de nuevos dispositivos de control y la propuesta de técnicas novedosas para la detección oportuna de fallas representan áreas de oportunidad en las cuales se requiere de bancos de pruebas con características como: precisión, repetibilidad entre pruebas, entornos de prueba seguros, etc. En este sentido, este trabajo presenta el desarrollo de un sistema PHIL monofásico con la finalidad de emular el comportamiento en corriente de máquinas eléctricas rotativas. Se proponen diferentes casos de estudio orientados a circuitos resistivos y resistivos-inductivos los cuales forman parte fundamental de la representación del circuito equivalente de un motor eléctrico, posteriormente se realiza un caso de estudio de emulación de comportamiento de un motor de CC junto con un puente rectificador, y finalmente se propone un caso de estudio basado en un modelo neuronal monofásico de un motor de inducción bajo diferentes condiciones de operación que incluyen diferentes condiciones de carga mecánica y diferentes condiciones de vueltas en devanados en cortocircuito en el estator. Por lo tanto, por medio de este trabajo se establecen bases sólidas para el desarrollo de un sistema PHIL con la capacidad de emular no solo máquinas eléctricas rotativas sino ya que el sistema se basa en un control en base a una corriente de referencia, diversas cargas o fuentes de alimentación pueden ser emuladas por medio del desarrollo propuesto ampliando las aplicaciones del sistema.

Palabras clave: Diagnóstico, Máquinas eléctricas, Power Hardware-in-the-loop, sistema de simulación, sistema en tiempo-real.

SUMMARY

Power Hardware-in-the-loop (PHIL) simulation is a useful, reliable and low-cost tool which allows emulating electrical behavior of different components or systems offering safe work environments for prototyping, drivers control design, and scientific research. In addition to this, the analysis of rotating electric machines represents an important area of interest for researchers and the industrial sector since most of the generated energy worldwide is consumed by motors, besides, the development of new control devices and the proposal of innovative techniques for appropriate fault detection represent some opportunity areas where test bench are required with different characteristics such as: precision, repeatability between tests, safe test environments, etc. In this sense, this work presents the development of a single-phase PHIL system with the capability to emulate the current behavior of rotating electrical machines. Different study cases are proposed. Firstly, a resistive load and resistive-inductive load are emulated which are a fundamental part of the representation of the equivalent circuit of an electric motor. Secondly, a DC motor along with a rectifier bridge is emulated by means of a theoretical model. Finally, a single-phase neuronal model of an induction motor under different operating conditions that include different mechanical load conditions and different winding conditions (short-circuited faults) in the stator is tested in the PHIL simulator. Therefore, through this work, solid bases are established for the development of a PHIL system with the capability to emulate rotating machines electric behavior, besides, other different loads can be simulated in this scheme since the PHIL requires a current signal reference signal that could be sourced by models of different loads being able to expand the applications for the proposed system.

Key words: Diagnosis, Electric Machines, Power Hardware-in-the-loop, simulation system, real-time system.

AGRADECIMIENTOS

A mis padres Angela Barrón Anaya y Arturo Mejía Pérez por su apoyo incondicional y la motivación que me brindan para ser mejor persona.

A mis hermanas Ana Karen Mejía Barrón e Ivonne Mejía Barrón por su valiosa compañía y su apoyo.

A mis amigos y compañeros, José Luis, Jessica, David, Emanuel, Francisco por su compañía y todos los buenos momentos.

Al Dr. Martin Valtierra Rodríguez y al Dr. David Granados Lieberman por el apoyo y dedicación hacia este trabajo.

Al Concejo Nacional de Ciencia y Tecnología (CONACYT) por el apoyo brindado bajo la beca 296868

TABLA DE CONTENIDOS

ÍNDICE DE FIGURAS

ÍNDICE DE TABLAS

CAPITULO I

Introducción

1. INTRODUCCIÓN

Debido a los rápidos aumentos en tecnologías computacionales, particularmente las técnicas de cómputo en paralelo y varias herramientas de simulación en tiempo real, el concepto de simulación HIL (por sus siglas en inglés *Hardware-in-the-loop*) es utilizado más ampliamente en aplicaciones electrónicas y en sistemas de potencia (Ren, et al. 2008). La simulación HIL es un método avanzado para el diseño y prueba de aparatos o prototipos denominados HuT (por sus siglas en inglés *hardware under test*) que a partir de un sistema virtual emula parte de un sistema mediante un lazo cerrado del sistema a estudiar (HuT). Además, este tipo de simulación provee diferentes ventajas ya que permite estudiar el HuT repetidamente y bajo condiciones de prueba reales. Esto minimiza los costos y el riesgo de examinar varias condiciones extremas, a su vez maximiza la oportunidad de identificar defectos ocultos en los dispositivos (Ren 2007; Mahdi 2015). La simulación HIL ha llegado a ser indispensable en la industria aeroespacial, automotriz, marina y de defensa ya que juega un papel importante en el desarrollo de sistemas de control, sistemas de seguridad automotrices, vehículos submarinos y sistemas de defensa; incluso en el área de investigación dentro de las universidades, este tipo de sistemas ha tenido una rápida integración debido a varias de las ventajas que ofrece como el bajo costo, el rápido prototipado, repetibilidad, seguridad y versatilidad (Fathy 2006). Por otra parte, las simulaciones HIL típicas involucran un controlador y la interfaz de señales de baja potencia (que típicamente oscilan entre los ±10V, <50mA) por medio de convertidores analógico digital ADC (por sus siglas en inglés *analog to digital converter*) y digital analógico DAC (por sus siglas en inglés *digital to analog Converter*) comerciales. Sin embargo, en los casos donde se cuenta con dispositivos de potencia (por ejemplo: un motor eléctrico, la red eléctrica, dispositivos de generación de energía), los cuales absorben o generan energía, se requiere de amplificadores de potencia especialmente diseñados y aparatos de conversión (actuadores, convertidores de voltaje). Este tipo de simulación se distingue entonces como HIL de potencia o PHIL (por sus siglas en inglés *power hardware-in-the-loop*). Por otra parte, el estudio de equipos eléctricos a menudo es llevada a cabo por medio de software de simulación tanto para proponer sistemas de control o una plataforma que permitan diversos estudios (como la detección de condiciones de falla de una máquina eléctrica, prueba de filtros activos, compensadores de potencia, etc.). En estos casos generalmente se llevan a cabo varias simplificaciones con el objetivo de reducir los tiempos de cálculo. Por lo que la aplicación de la simulación PHIL en sistemas eléctricos es ideal por las características antes mencionadas. En particular, las máquinas eléctricas rotativas son dispositivos que convierten la energía eléctrica en energía mecánica (motores) o viceversa (generadores) los cuales se han empleado por sus características de alta eficiencia, velocidad y su rápida respuesta dinámica (Vukosavic, 2012). En lo que respecta a motores eléctricos han sido empleados y estudiados en gran medida, siendo el motor de inducción una de las máquinas por excelencia en aplicaciones industriales los cuales consumen más de la mitad de la energía generada a nivel mundial. Además de la alta eficiencia que poseen las máquinas eléctricas rotativas una de las razones por las que siguen siendo las máquinas por excelencia en el sector industrial, es por los desarrollos tecnológicos para dispositivos de control de variables como posición, velocidad y aceleración. Sin embargo, una de los mayores inconvenientes es la aparición de condiciones de falla, ya que, aunque los motores son máquinas robustas, pueden presentar fallas en sus principales componentes como son: el rotor, el estator y los baleros, las cuales si no son detectadas pueden presentar pérdidas económicas por mantenimientos correctivos o comprometer la calidad de los productos en la línea de producción. En este sentido, el análisis de fallas en motores eléctricos no es un tema nuevo, ya que se han desarrollado una gran cantidad de investigaciones alrededor de las causas y las posibles técnicas para una detección oportuna, que ofrezca herramientas de análisis con las cuales sea posible detectar fallas inclusive desde su estado incipiente, programando un mantenimiento adecuado, minimizando los costos y reduciendo los tiempos ocasionados por mantenimientos correctivos. Más aún, el análisis de firmas de corriente en motores MCSA (por sus siglas en ingles *motor* *current signature analysis*) para el caso de los motores de inducción, es una de las técnicas más explorada para la detección de las diferentes condiciones de falla, en la cual se analizan componentes frecuenciales anormales que puedan estar relacionadas con determinada falla en donde un gran número de metodologías han sido propuestas para determinar la condición del motor. Sin embargo, estas técnicas solo son validadas bajo condiciones de operación específicas y en motores de determinadas características. En este sentido, una aplicación novedosa para los sistemas de simulación PHIL es la emulación de máquinas eléctricas que cuente bajo diferentes condiciones de operación y pueda servir como herramienta de validación de técnicas de detección, considerando diversas condiciones de falla, carga, potencia, etc. Además, que sirva para el análisis de los efectos de calidad de la energía que ocasiona una determinada máquina eléctrica, por ejemplo, los armónicos introducidos a la red eléctrica por las máquinas de CD debido a etapas de rectificación, etc. El presente trabajo se enfoca en la puesta en marcha de un sistema de simulación PHIL, con aplicación en la emulación de máquinas eléctricas rotativas visto desde un punto de vista de carga eléctrica y considerando condiciones de operación.

1.1 Antecedentes

El desarrollo de sistemas de simulación PHIL de potencia ha tenido una gran aceptación en un gran número de aplicaciones tanto en el sector industrial para desarrollo o pruebas de nuevos productos como en el sector académico en el área de investigación. Por lo tanto, diferentes trabajos se han realizado con diferentes enfoques como: algoritmos de interfaz, mejoras en la estabilidad, algoritmos de control, e innovación en las aplicaciones de la simulación PHIL. Los algoritmos de interfaz determinan como se intercambian las señales entre la parte virtual y la parte real del sistema. En este sentido, uno de los principales inconvenientes de los algoritmos de interfaz es que pueden llegar a causar problemas de estabilidad y/o resultados con baja precisión; para esto se han propuesto y realizado estudios de la naturaleza de estos inconvenientes con diferentes algoritmos de interfaz tales como: el método del transformador ideal (ITM por sus siglas en ingles *ideal transformer method*) el cual es uno de los métodos más convencionales y sencillos que cuenta con una alta precisión pero baja estabilidad, por el contrario métodos como el método de línea de transmisión y el método de duplicación parcial de circuito (PCD por sus siglas en inglés *partial circuit duplication*) cuentan con una alta estabilidad, pero la precisión depende de los valores de los componentes de enlace, métodos como aproximación a sistemas de primer orden (TFA por sus siglas en ingles *time-variant first-order approximation*) los cuales presentan estabilidad, sin embargo son sensibles al ruido y presentan una alta complejidad para su implementación, y finalmente, el método de impedancia de amortiguación (DIM por sus siglas en inglés *damping impedance method*) el cual es una variante del ITM, siendo uno de los métodos altamente recomendados en las aplicaciones PHIL por su alta precisión y estabilidad (Ren et al. 2008). Aunado a estos algoritmos de interfaz se han propuesto diversos métodos para mejorar la estabilidad en sistemas de simulación PHIL, como la retroalimentación de corriente filtrada, o métodos de deslizamiento de impedancias (Markou et al. 2017).

Por otra parte, aunque existen diferentes algoritmos de interfaz, a su vez los sistemas PHIL se pueden clasificar por su modo de control, modo corriente y modo voltaje en función de la variable que se desee emular, estos modos de control dependen de los componentes usados típicamente con las etapas de amplificación en donde se han analizado los circuitos magnéticos para un buen acoplamiento al HuT (Vodyakho et al. 2012; Schmitt et al. 2016), las variables a retroalimentar y los tipos de controladores que se emplean por ejemplo: control PID (Benigni et al. 2011), control en espacio de estados (Mahdi 2015), control vectorial (Tzou et al. 1998), control por histéresis (Honglin et al. 2017) o control por modos deslizantes (de Souza et al. 2017).

Por otro lado, se ha tenido gran aportación en las aplicaciones en las cuales la simulación PHIL puede ser de utilidad, que van desde simulaciones de máquinas eléctricas con aplicaciones en el área automotriz, el desarrollo de sistemas de control para máquinas eléctricas, la emulación de los diversos componentes de microrredes eléctricas para diversos análisis de calidad de la energía, entre otras. Por ejemplo, Bevis et al. (2010) implementaron un sistema de simulación PHIL para pruebas de motores de reluctancia conmutados, los cuales presentan una gran aplicación en vehículos eléctricos, en donde se pueden examinar los efectos de la variación del bus de CD bajo condiciones estáticas y dinámicas de velocidad y carga. Así también, implementaciones de simulación PHIL de máquinas eléctricas como máquinas síncronas de imán permanente (Schmitt et al. 2016; Amitkumar et al. 2018), máquinas de inducción (Vodyakho et al. 2012) y sistemas de generación por turbina de gas (Steurer et al. 2010), con la finalidad de probar drivers y sistemas de control sin el riesgo asociado a las pruebas físicas y sin la necesidad de usar los componentes reales. Igualmente, aplicaciones de simulación PHIL con relación a las energías alternativas se ha llevado a cabo con la finalidad de mejorar los sistemas de control y las estrategias de integración a la red; por ejemplo, Li et al. (2006) desarrollaron un sistema unificado para pruebas de sistemas de energía eólica el cual contiene la simulación de una red eléctrica y un sistema capaz de emular el comportamiento de un generador eólico. Del mismo modo, la integración de modelos dinámicos de paneles fotovoltaicos se ha llevado a cabo considerando las variaciones de voltaje y las variaciones térmicas de un panel fotovoltaico de acuerdo a la demanda de corriente, la temperatura y la irradiancia (Jung and Ahmed 2012). Además, dado que las microrredes forman parte importante en la calidad y ahorro de energía junto con una menor dependencia de la red de distribución, presenta una gran oportunidad de aplicación de simulación PHIL debido a la gran cantidad de sistemas que la componen tales como: sistemas de generación distribuida, sistemas de almacenamiento de energía, sistemas para la gestión de cargas, sistemas de monitoreo y control de flujos de potencia y técnicas de mantenimientos preventivos, en donde por medio de simulación PHIL puede fortalecer el desarrollo y la innovación de las diferentes partes que conforman una microrred. Por ejemplo: una simulación PHIL es propuesta para emular diversos tipos de sistemas de generación distribuida como paneles fotovoltaicos, generadores eólicos, generadores a diésel y sistemas de almacenamiento de energía por batería (Jeon et al. 2010; Fox and Gislason 2014; Kolb and Kammerer 2014). Así también, la simulación PHIL de diferentes cargas linares y no lineales con la finalidad de observar fenómenos de calidad de la energía y/o probar la funcionalidad de filtros activos orientados a mejorar la calidad de la energía (Camila et al. 2013; Hogan et al. 2014; Heerdt et al. 2014; Kesler et al. 2014). Por último, además de la investigación, las simulaciones PHIL proporcionan herramientas didácticas para la enseñanza del de diversos equipos eléctricos disponibles en los sistemas de potencia modernos, en donde el estudiante puede operar y observar de manera segura los comportamientos de dispositivos virtuales y su interacción con diferentes componentes (Kotsampopoulos et al. 2017).

Finalmente, una de las aplicaciones propuestas en el presente trabajo es la evaluación de las condiciones de operación de máquinas eléctricas rotativas, cuyo estudio ha sido de interés a nivel mundial e incluso a nivel local en trabajos realizados dentro de la Universidad Autónoma de Querétaro. En este sentido una de las técnicas ampliamente usada es el análisis MCSA en donde se han propuesto diversas técnicas para la detección en línea incluso considerando estados transitorios: como por ejemplo: la detección de componentes frecuenciales para el diagnóstico de diferentes niveles de severidad de barra rota (Rivera et al. 2018), así también, el análisis de fallas en los rodamientos se ha empleado por medio de MCSA (Morales et al. 2018), incluso técnicas para el diagnóstico considerando, además de la condición de falla, diferentes condiciones de carga han sido propuestas (Rangel et al. 2014). En este sentido, el uso de simulación PHIL como herramienta de validación de sistemas de diagnóstico podría ser de gran ayuda, ya que diferentes condiciones o capacidades pueden ser analizadas.

1.2 Descripción del problema

La evaluación de las condiciones de las máquinas eléctricas rotativas ha sido un caso de estudio de interés debido a la gran cantidad de procesos industriales que dependen de este tipo de máquinas, y de acuerdo con la literatura existe una gran cantidad de técnicas que proponen una detección oportuna de una falla con la finalidad de evitar mantenimientos correctivos. En este sentido, uno de los enfoques principales de presente trabajo es el desarrollo de un sistema para simulación PHIL, que pueda ser empleado como herramienta de validación para instrumentos de diagnóstico de máquinas eléctricas por medio del monitoreo de corriente eléctrica; en donde se puedan considerar diversas condiciones como: carga mecánica, o severidad de la condición a estudiar. A su vez, contar con una herramienta que pueda reproducir el comportamiento en corriente de determinados tipos de cargas que pueda servir como herramienta didáctica o para fines de investigación considerando cuestiones de calidad de la energía como la distorsión armónica, generada por cargas no lineales. En Fig. 1 se muestra a manera general la integración de los principales componentes que involucran una simulación PHIL, en donde en primer lugar se tiene un simulador en tiempo real el cual contiene el o los

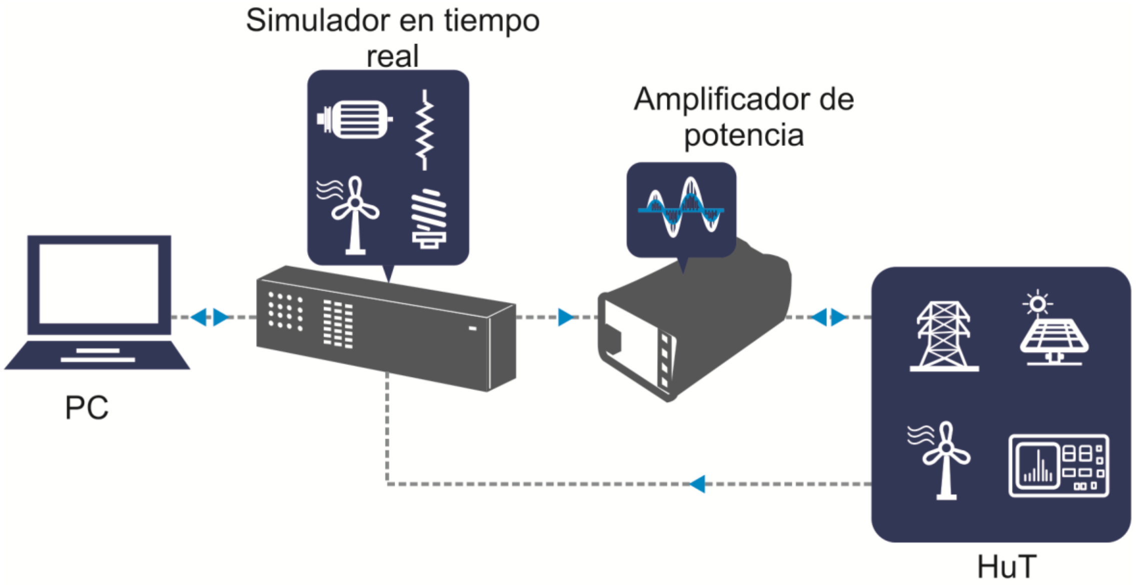

Fig. 1. Sistema de simulación PHIL.

modelos de la parte virtual del sistema o carga a emular, lleva a cabo la el monitoreo, la retroalimentación y el control de la etapa de potencia. Posteriormente, se tiene la etapa de potencia la cual generalmente consta de un inversor fuente de voltaje (VSI por sus siglas en inglés *voltage source inverter*), el cual se conecta al HuT que puede ser la red eléctrica o alguna otra fuente o el sistema de diagnóstico de condiciones a probar.

Aunque existen tres principales componentes en los sistemas de simulación PHIL: simulador en tiempo real, amplificador de potencia y HuT, el desarrollo de la presente investigación involucra diferentes cuestiones, por un lado, está en la implementación del algoritmo de interfaz que se encargara del intercambio de señales entre la parte virtual y la parte real del sistema. Además, la propuesta de una ley de control adecuada que proporcione la estabilidad y precisión al sistema. Igualmente, la selección de componentes adecuados y correcta instrumentación forma parte fundamental en el desarrollo del proyecto. Otra parte fundamental es la selección de los componentes para la simulación PHIL ya que se en base a esta selección se obtendrán las posibles limitantes del sistema propuesto. Por último, el desarrollo e implementación de los modelos que comprenden la parte virtual de la simulación PHIL.

En la parte de la aportación científica, existen diferentes áreas de oportunidad en las cuales se pueden hacer propuestas que van desde los modelos a utilizar en la parte virtual, el monitoreo de variables de retroalimentación, mejoras en la estabilidad y precisión, o innovación en las aplicaciones de simulación PHIL.

1.3 Hipótesis y objetivos

1.3.1 Hipótesis

Mediante el desarrollo de un sistema de simulación PHIL se puede realizar la validación de diferentes métodos de detección en línea de fallas basados en MCSA, ampliando las pruebas de validación, considerando diferentes condiciones de operación. Del mismo modo dado a la amplia gama de aplicaciones de simulación PHIL se puede obtener una herramienta con la capacidad de emular una corriente de determinada carga la cual puede ser empleada para fines de enseñanza o investigación de calidad de la energía en un determinado sistema.

1.3.2 Objetivo general

Desarrollar un sistema HIL de potencia que permita emular la corriente demandada por máquinas eléctricas rotativas para la validación de diferentes modelos teóricos y experimentales, así como el estudio en el impacto de la calidad de la energía eléctrica ante la acción de estas máquinas en diversas condiciones de operación, por medio del estudio empírico y analítico de las cargas propuestas, la implementación de dichos modelos en un sistema en tiempo real y el desarrollo de un sistema basado en electrónica de potencia.

1.3.3 Objetivos particulares

1. Construir una plataforma de potencia para la simulación de cargas eléctricas genéricas documentando sus especificaciones técnicas, a partir del diseño inversor de voltaje CA-CC, para poder emular y controlar el consumo en corriente.

2. Obtener modelos de los motores eléctricos que permitan su implementación en tiempo real por medio de una búsqueda bibliográfica exhaustiva en cuanto a modelos teóricos de las cargas eléctricas propuestas y la adquisición de señales de corriente y voltaje que permitan el modelado experimental.

3. Implementar los modelos en la plataforma de potencia desarrollada para validar los diferentes modelos obtenidos mediante la comparativa con del modelo con el sistema real.
4. Desarrollar estudios del impacto en la calidad de la energía por medio del sistema HIL desarrollado para validar parámetros de calidad de la energía generados por el sistema HIL propuesto y el sistema real.
5. Publicar tres artículos en revistas indexadas, mediante el estudio y desarrollo de la arquitectura e instrumentos generados de este proyecto para difusión de la presente investigación.
6. Generar tesis de grado mediante la presente investigación para la formación de recursos humanos en esta línea de investigación.

1.4 Justificación

La principal motivación para realizar este trabajo de investigación es la necesidad de contar con un sistema que permita emular cargas eléctricas físicas reales, específicamente máquinas eléctricas rotativas. En donde, la contribución científica de este trabajo es el desarrollo de modelos de máquinas rotativas el cual, por un lado, permitirá validar y cuantificar experimentalmente el grado de exactitud de distintos modelos que se han reportado en la literatura y, por otro lado, permitirá desarrollar y validar los modelos que se propongan en este trabajo desde el punto de vista consumo de potencia mediante las formas de onda de las señales de corriente. Otros aspectos como tipo de modelo, complejidad de modelo para emulación en tiempo real, rapidez, exactitud, consideraciones y simplificaciones para facilitar el modelado, confiabilidad y repetitividad de los resultados, entre muchos otros aspectos podrán ser estudiados y discutidos experimentalmente, es decir, cuando se someten a condiciones reales de ejecución y operación dejando atrás las condiciones y simplificaciones del software.

Además de la contribución científica mencionada en el párrafo anterior, en este trabajo se propone el desarrollo tecnológico de un prototipo de un sistema HIL de potencia, en donde, algunos de los puntos que justifican la implementación de este tipo de sistemas se derivan principalmente de ventajas en costos y tiempos de desarrollo de pruebas experimentales. Un sistema HIL permitirá emular distintas máquinas en un mismo sistema sin la necesidad de tener todas las máquinas físicamente, considerando diversas capacidades, tamaños, marcas, modelos, etc. Más aún, no solo las condiciones del equipo pueden ser cambiadas o controladas, sino que las condiciones del laboratorio de pruebas también se pueden controlar para generar condiciones específicas o extremas de prueba que en la vida real son difíciles de alcanzar y por lo tanto difíciles de generar pero que son importantes de analizar porque representan posibles condiciones limites o de riesgo para el equipo bajo prueba. Por otro lado, las emulaciones en sistemas de simulación PHIL no solo permiten realizar pruebas y validaciones en menor tiempo y con menores costos de desarrollo, sino que también reducen costos durante las pruebas al eliminar la necesidad de hardware o equipos reales que se desgastan y/u ocupan mantenimiento. Esto, a su vez, con fines de cuantificar estadísticamente la confiabilidad de algún resultado, posibilita la realización de un gran número de repeticiones de alguna prueba en particular sin alterar o afectar las condiciones iniciales de prueba.

Otro factor que motiva este trabajo, desde el punto de vista calidad de la energía eléctrica, es que este sistema y los modelos implementados de los diversos casos de estudio permitirán hacer investigaciones sobre el impacto negativo de una máquina real en el sistema eléctrico al que se conecte, es decir, si al operar genera desbalance en magnitud y fase, si afecta el factor de potencia y por lo tanto las componentes de potencia, si aumenta la distorsión armónica total, si genera fluctuaciones o variaciones en el valor cuadrático medio (RMS del inglés, *root mean square*) de las líneas de voltaje y corriente, entre algunos otros parámetros basados en índices de la calidad de la energía. En este sentido, investigaciones sobre el dimensionamiento de equipos y buses eléctricos, propuestas de controladores eléctricos y diseño de protecciones podrán ser realizados y probados gracias a este equipo.

Finalmente, la orientación de este trabajo hacia máquinas eléctricas rotativas y algunos de sus controladores de potencia se justifican por las siguientes razones: los motores son los elementos claves de cualquier sistema de automatización y movimiento en los procesos industriales, por lo tanto, un sistema que permita validar modelos que estudian el comportamiento de estas máquinas con el objetivo de aumentar su eficiencia y confiabilidad es altamente deseable. Por último, estas máquinas en conjunto a sus dispositivos de control tienen un gran impacto en la calidad del suministro eléctrico, lo cual afecta al equipo mismo y a otros equipos sensibles conectados al bus eléctrico generando pérdidas económicas por daños en los equipos y posibles paros de producción. Esto, por lo tanto, propicia un interés especial en el diseño de equipos y protecciones en el cual el sistema propuesto podría ser utilizado como herramienta para probar los equipos antes mencionados en condiciones reales de operación.

1.5 Planteamiento general

La metodología de manera general propuesta para este trabajo de investigación se muestra en la Fig. 2. La cual consiste en un sistema de simulación PHIL en donde una plataforma con capacidad de procesamiento de tiempo real sirve para la implementación del algoritmo de control el cual se basa en emular una corriente de referencia a partir de un amplificador de potencia, que es conectado al sistema a estudiar o HuT. La corriente a emular o corriente de referencia es obtenida por medio de un modelo que describe un comportamiento de acuerdo a las características del sistema real.

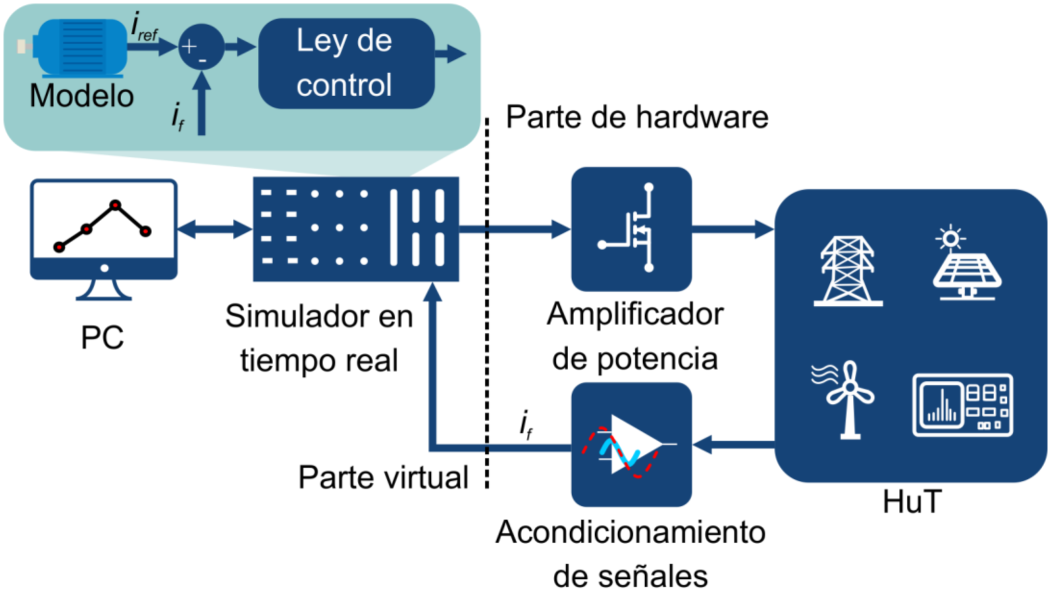

Fig. 2. Planteamiento general de desarrollo de sistema de simulación PHIL.

En la parte del desarrollo y puesta en marcha del sistema de simulación PHIL se llevará a cabo la selección de una plataforma en tiempo real en la cual se pueda implementar el control y los modelos desarrollados y que a su vez permita el monitoreo para la validación del sistema. Además, se debe llevar a cabo la selección de los componentes adecuados del amplificador de potencia que incluye un VSI junto con una etapa de filtrado, y por último el acondicionamiento y adquisición de la o las señales de retroalimentación para el control y la validación del sistema.

Los bloques que componen la estructura del Sistema HIL son los siguientes:

- <u>Simulador en tiempo real:</u> Plataforma encargada de la implementación de la parte virtual del sistema a estudiar, incluye la ley de control para emular la corriente de referencia por medio del amplificador de potencia.
- <u>Acondicionamiento de señales:</u> Este bloque contiene los circuitos necesarios para la adecuación de las señales de corriente y/o voltaje a ser retroalimentadas para el sistema de simulación PHIL.

- Ley de control: Se encarga de controlar la etapa de potencia en base a una corriente de referencia, dar estabilidad y precisión al sistema.

- Modelo: Este módulo contiene los modelos matemáticos discretizados de las máquinas eléctricas.

- Amplificador de potencia: Este módulo se encarga de controlar el consumo real del dispositivo que se esté emulando, este proceso se realizará a través de un VSI.

CAPITULO II

Estado del arte

2. ESTADO DEL ARTE

Un simulador en tiempo real en interfaz con un sistema físico forma una simulación PHIL. Este tipo de test tiene un gran número de ventajas y al mismo tiempo requiere de consideraciones especiales. Donde uno de los principales retos de la simulación PHIL es la operación estable del sistema. Más aún, la estabilidad debe de estar acompañada de resultados precisos. Como se mencionó en el capítulo anterior ambos tanto la estabilidad como la precisión dependen del algoritmo de interfaz (Mahdi 2015); aunque existen diferentes algoritmos como el ITM, el método de la línea de transmisión, el método de duplicación parcial de circuitos, o el método de impedancia de amortiguación en este trabajo se propone emplear el método de transformador ideal debido a su simplicidad y a las posibilidades que tiene para mejorar su estabilidad por medio de etapas de filtrado.

2.1 Método del transformador ideal ITM

Uno de los algoritmos más clásicos de algoritmo de interfaz es el método de ITM. Debido a su estructura simple y si sencillo principio de operación, ha sido usado ampliamente (Ren et al. 2008). Como se observa en la Fig. 3(a) el algoritmo parte de un circuito divisor de voltaje el cual en teoría es estable sin embargo el hecho de llevar a cabo la implementación introduce al sistema inestabilidad y baja precisión. Además, en la Fig. 3(b) y 3(c) se muestran los dos tipos de configuración los cuales se definen como de tipo voltaje y tipo corriente respectivamente, dependiendo la variable que se desee controlar. Entonces, si se analiza la interfaz de voltaje que se muestra en la Fig. 3(b) el amplificador de potencia genera un voltaje v_{HuT} por medio del voltaje virtual v_V el cual se puede expresar de la siguiente manera:

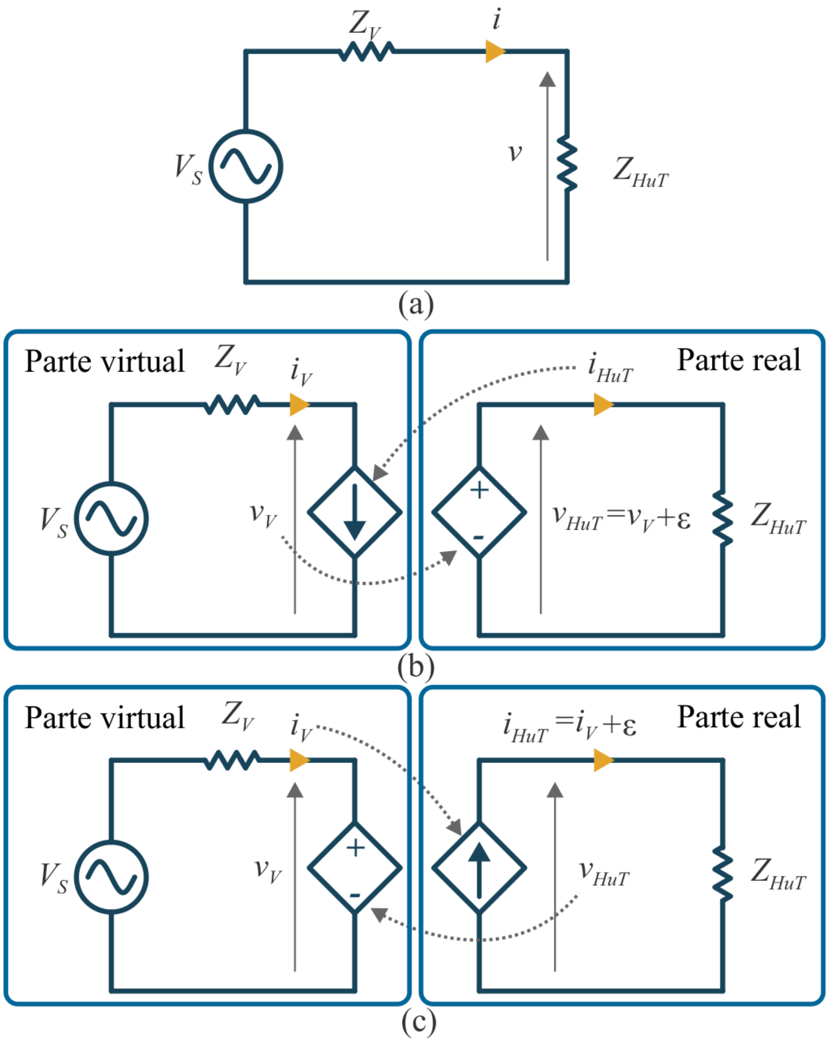

Fig. 3(a) Circuito original de ITM; (b) Interfaz ITM de tipo voltaje; (b) Interfaz ITM de tipo corriente.

$$v_{HuT}(k) = v_V(k) + \varepsilon \quad (1)$$

Donde ε es el error que ocurre en la etapa de amplificación de la simulación PHIL. En consecuencia, un error en la componente de corriente de retroalimentación i_{HuT} ocurre y este puede ser determinado por:

$$\Delta i_{HuT}(k) = \frac{\varepsilon}{Z_{HuT}} \quad (2)$$

Por lo tanto, ya que el voltaje virtual se obtiene por la retroalimentación de la corriente como $v_V(k)=V_S(k)-Z_V I_V(k)$, un error en v_V en el tiempo k+1 es obtenido por:

$$\Delta v_V(k+1) = -\left(\frac{Z_v}{Z_{HuT}}\right)\varepsilon \tag{3}$$

$$Z_{HuT} > Z_V$$

Esta variación en el voltaje virtual amplifica el error en tiempos futuros en un factor de $-(Z_V/Z_{HuT})$ introduciendo inestabilidad cuando $Z_V>Z_{HuT}$. Este mismo efecto se ve presente en la interfaz de tipo corriente ya que ahora la corriente en el *HuT* (i_{HuT}) es controlada por el voltaje de retroalimentación de voltaje v_{HuT}. En este caso, la corriente emulada i_{HuT} es igual a la corriente virtual más una componente de error ε introducida por la etapa de amplificación.

$$i_{HuT}(k) = i_V(k) + \varepsilon \tag{4}$$

Este valor puede introducir errores en el voltaje retroalimentado el cual se puede estimar por medio de:

$$\Delta v_{HuT}(k) = Z_{HuT}\varepsilon \tag{5}$$

Por lo tanto, la corriente virtual $i_V(k)=(v_V(k)-V_S(k))\ /Z_V$ puede introducir errores a estados futuros $k+1$:

$$\Delta i_V(k+1) = \left(\frac{Z_{HuT}}{Z_V}\right)\varepsilon \tag{6}$$

Entonces problemas de inestabilidad pueden ocurrir cuando $Z_{HuT}>Z_V$.

2.2 Inversor CC-CA sinusoidal de modo conmutado

Uno de los amplificadores ampliamente usados en los sistemas de simulación PHIL son los convertidores de CC-CA sinusoidal además de tener una gran aplicación en alimentación de motores o sistemas de fuentes ininterrumpidas. Además, una característica de los inversores de modo conmutado que lo hace ideal en la aplicación de sistemas de simulación PHIL es que el flujo de potencia es reversible; es decir que puede funcionar para proporcionar potencia (como inversor) o para consumir potencia como (rectificador). Estos inversores también se denominan inversores de fuente de voltaje VSI y se subdividen en tres categorías: Inversores modulados por ancho de pulso, inversores de onda cuadrada e inversores monofásicos con cancelación de voltaje. En la Fig. 4 se muestra la operación de un inversor monofásico conmutado y su zona de trabajo, como se ve en la Fig. 4(a), la entrada del inversor esta acoplada por un capacitor a la entrada con la finalidad de filtrar la componente de CC y la salida que comúnmente tiene una etapa de filtrado. Dependiendo el tipo de carga conectado o el modo de operación deseado el inversor puede operar en los cuatro cuadrantes que se muestran en la Fig. 4(b) en donde se observan las zonas donde puede operar como inversor que es cuando el voltaje y la corriente de salida tienen el mismo signo, y el modo rectificador en el cual la transferencia de potencia se hace hacia el bus de CC cuando el voltaje y la corriente de salida tienen signos opuestos.

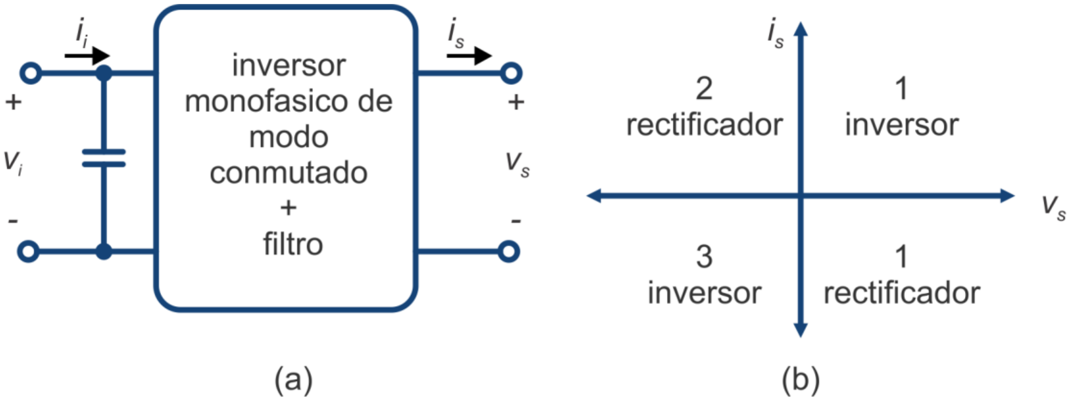

Fig. 4. (a) Inversor monofásico de modo conmutado; (b) cuadrantes de operación de inversor.

En general todas las topologías de inversores CC a CA se deducen mediante el convertidor de medio puente (o una pata) que se muestra en la Fig. 5. En el cual la salida está disponible en el punto medio "*o*" del voltaje de entrada, sin embargo, esto no se necesita en la mayoría de los inversores ni está disponible.

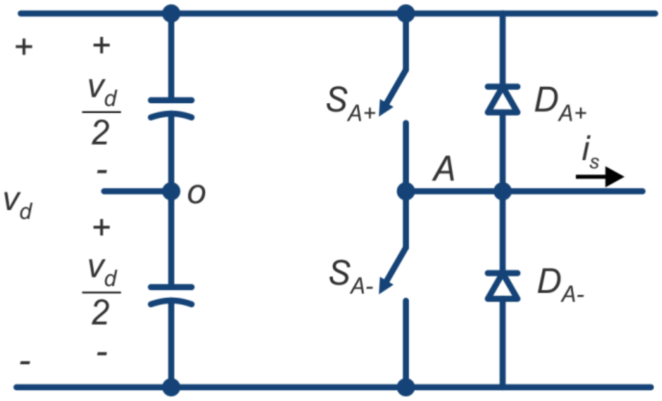

Fig. 5. Inversor de modo conmutado de medio puente.

Respecto a la modulación de ancho de pulso para la conmutación del inversor se debe considerar que la salida esperada es una función sinusoidal con magnitud y frecuencia controlables. Por lo tanto, a fin de producir una forma de onda sinusoidal de voltaje, se compara una señal de control sinusoidal con una forma de onda triangular.

Un factor importante en este tipo de inversor es la selección de la técnica PWM, la cual debe garantizar una forma de onda de voltaje fácil de filtrar que permita tener voltajes con distorsiones armónicas menores al 3%, y poder tener un fácil control sobre la señal de voltaje de salida, para poder modificar según las exigencias de las pruebas tanto la amplitud como la frecuencia. Dentro de las técnicas comúnmente utilizada se tienen: la modulación de ancho de un solo pulso por semiciclo, la modulación de varios pulsos por semiciclo y la modulación de ancho de pulso sinusoidal. La modulación de ancho de pulso sinusoidal presenta varios pulsos por semiciclo y el ancho de pulso varia en forma proporcional a la amplitud de la onda sinusoidal. Esta técnica de modulación puede trabajarse de forma unipolar o bipolar.

En donde el método de modulación unipolar presenta la ventaja de que las frecuencias armónicas introducida debido a la conmutación son el doble de las generada por modulación SPWM bipolar (Mohan et al. 2009), en la Fig. 6 se muestra un inversor de puente completo junto con su etapa de filtrado.

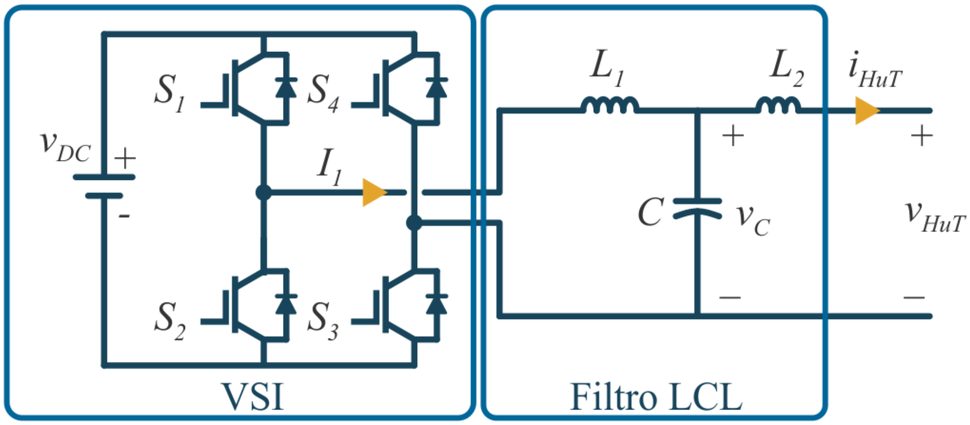

Fig. 6. Inversor de puente completo con etapa de filtrado.

2.3 Modelado de máquinas eléctricas

2.3.1 Modelado teórico

El modelado teórico se trata de un método analítico, en el que se recurre a leyes básicas de la física para describir el comportamiento dinámico de un fenómeno o proceso. A continuación, se presentan algunos métodos empleados en la literatura para el modelado de motores eléctricos de corriente continua (CC), corriente alterna (CA) y motores síncronos, en donde para este tipo de máquinas eléctricas existen diversos circuitos equivalentes que sirven para obtener un modelo eléctrico de la máquina (Haitham, et al., 2012).

2.3.2 Motores de corriente continua

Existen diferentes topologías de conexión de motores de corriente continua, ya sea de excitación independiente, serie o paralelo. En la Fig. 7 se muestra una de las posibles representaciones de un motor de corriente continua, donde se tiene como entrada un voltaje de alimentación $e_a(t)$, y a la salida una velocidad angular $\omega(t)$ con un determinado torque $\tau(t)$, los cuales se encuentran relacionados con la corriente de alimentación $i(t)$ por la ecuación (7).

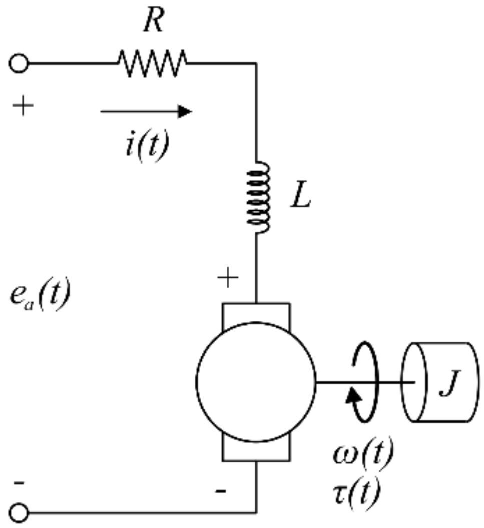

Fig. 7. Circuito equivalente de motor CC.

$$\frac{i(s)}{e_a(s)} = \frac{\frac{K_\tau}{JL}}{s^2 + \frac{R}{L}s + \frac{K_V K_\tau}{JL}} \tag{7}$$

donde:

R: es la resistencia equivalente del motor de CC.
L: es la inductancia equivalente del motor de CC.
J: es el momento polar de inercia.
K_τ: es la constante de proporcionalidad de torque.
K_V: es la constante de fuerza electromotriz.

2.3.3 Motores de corriente alterna

Entre los motores de corriente alterna, los motores de inducción del tipo jaula de ardilla son los que tienen en la actualidad una mayor presencia en la industria debido a sus características como: bajo costo, versatilidad y robustez. Debido a esto, se han desarrollado un gran número de técnicas para el modelado de este tipo de máquinas eléctricas. En la Fig. 8 se muestra un circuito equivalente del motor de inducción de una fase. Este consiste de la resistencia del lado del estator e inductancia de fuga, mutua inductancia, la resistencia e inductancia rotórica, y voltaje inducido.

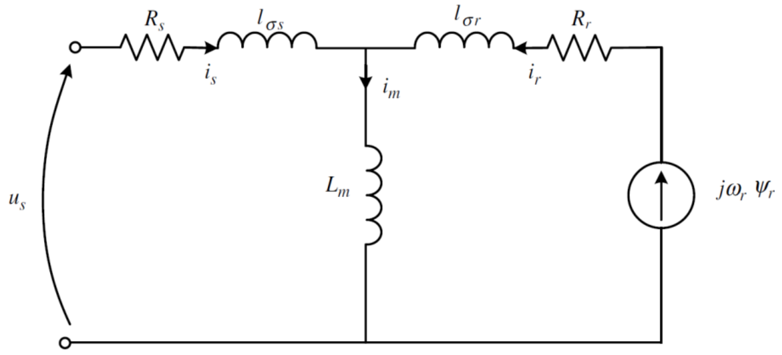

Fig. 8. Circuito equivalente por fase de motor de inducción.

El motor de inducción en un marco arbitrario de referencia K puede ser presentado en una velocidad angular $\omega_K$como:

$$u_{sk} = R_{sk} i_{sk} + \frac{d\psi_{sk}}{dt} + j\omega_k \psi_{sk} \tag{8}$$

$$u_{sk} = R_{sk} i_{sk} + \frac{d\psi_{sk}}{dt} + j(\omega_k - \omega_r)\psi_{sk} \tag{9}$$

$$\psi_{sk} = L_s i_{sk} + L_m i_{rk} \tag{10}$$

$$\psi_{rk} = L_r i_{rk} + L_m i_{sk} \tag{11}$$

$$\frac{d\omega_r}{dt} = \frac{1}{T_M}\left[I_m(\psi_{sk} i_{sk}) - t_l\right] \tag{12}$$

Donde T_M es una constante de tiempo mecánico; donde u_s, i_s, i_r, ψ_s y ψ_r son los vectores de voltajes, corrientes, y flujo (estator y rotor); R_s, R_r son las resistencias del estator y del rotor; ω_r es la velocidad angular del rotor; ω_a es una velocidad angular del marco de referencia; J es el momento de inercia; y t_l es el torque de carga.

Las relaciones de corriente son:

$$i_s = \frac{1}{L_s}\Psi_s - \frac{L_m}{L_s} i_r \tag{13}$$

$$i_r = \frac{1}{L_r}\Psi_r - \frac{L_m}{L_r} i_s \tag{14}$$

El modelo de motor de inducción por unidad presentado en un marco de referencia de velocidad arbitrario es dado por:

$$\frac{di_{sx}}{d\tau} = \frac{R_s L_r^2 + R_r L_m^2}{L_r w_\sigma} i_{sx} + \frac{R_r L_m}{L_r w_\sigma}\psi_{rx} + \omega_k i_{sy} + \omega_r \frac{L_m}{w_\sigma}\psi_{ry} + \frac{L_r}{w_\sigma} u_{sx} \tag{15}$$

$$\frac{di_{sy}}{d\tau} = \frac{R_s L_r^2 + R_r L_m^2}{L_r w_\sigma} i_{sy} + \frac{R_r L_m}{L_r w_\sigma}\psi_{ry} - \omega_k i_{sx} - \omega_r \frac{L_m}{w_\sigma}\psi_{rx} + \frac{L_r}{w_\sigma} u_{sy} \tag{16}$$

$$\frac{d\psi_{rx}}{d\tau} = -\frac{R_r}{L_r}\psi_{rx} - \omega_r\psi_{ry} + \frac{R_r L_m}{L_r} i_{sx} \tag{17}$$

$$\frac{d\psi_{ry}}{d\tau} = -\frac{R_r}{L_r}\psi_{ry} + \omega_r\psi_{rx} + \frac{R_r L_m}{L_r} i_{sy} \tag{18}$$

$$\frac{d\omega_r}{d\tau} = \frac{L_m}{J L_r}\left(\psi_{rx} i_{sy} - \psi_{ry} i_{sx}\right) - \frac{1}{J} t_0 \tag{19}$$

En donde, u_s, i_s, i_r, ψ_s y ψ_r son los vectores de voltajes, corrientes y flujos (del estator y del rotor); R_s, R_r son las resistencias del estator y del rotor; ω_r es la velocidad angular del rotor; ω_k es una velocidad angular del marco de referencia; J es el momento de inercia; y t_0 es el torque de carga.

2.3.4 Máquinas síncronas

Las máquinas síncronas son máquinas eléctricas rotativas de corriente alterna cuya velocidad de rotación del eje y frecuencia eléctrica están sincronizadas y son mutuamente dependientes, esta máquina puede operar tanto como motor y generador. Los modelos matemáticos de motores síncronos de imanes permanentes por unidad en un marco de referencia rotativo ω_k son:

$$\overline{u_s} = R_S\overline{i_s} + \frac{d\overline{\psi_s}}{dt} + j\omega_k\overline{\psi_s} \tag{20}$$

$$\overline{\psi_s} = L_s\overline{i_s} + \overline{\psi_f} \tag{21}$$

$$\frac{d\omega_r}{dt} = \frac{1}{J}(t_e - t_l) \tag{22}$$

$$\frac{d\theta}{dt} = \omega_r \tag{23}$$

Donde ω_r es la velocidad angular del rotor; θ es la posición angular del rotor; y ψ_r es el flujo del imán permanente.

2.4 Herramientas de modelado de sistemas

Se trata de un método experimental que permite obtener el modelo de un sistema a partir de datos reales recogidos del sistema bajo estudio. En la literatura se han empleado algunas técnicas matemáticas tradicionales. Estas técnicas van desde técnicas estadísticas como: regresión lineal, regresión múltiple, suavización exponencial, y técnicas de mínimos cuadrados; Técnicas de series de tiempo como: modelos autorregresivos, modelos autorregresivos de media móvil o máquinas de soporte de vectores; métodos de computación flexible como algoritmos genéticos, lógica difusa y redes neuronales (Singh, et al., 2012).

2.4.1 Técnicas estadísticas

Una de las técnicas más empleadas es la *regresión lineal***,** se define como un procedimiento mediante el cual se trata de determinar si existe o no relación de dependencia entre dos o más variables. Es decir, conociendo los valores de una variable independiente, se trata de estimar los valores de una o más variables dependientes. La regresión en forma gráfica, trata de lograr que una dispersión de las frecuencias sea ajustada a una línea recta o curva. La regresión lineal es una de las técnicas estadísticas más empleadas y es a menudo sencilla de implementar. Los métodos de regresión son usualmente empleados para relacionar un modelo con el consumo de una carga y otros factores como condiciones ambientales. Este método asume que la carga se puede dividir en una tendencia estándar y una tendencia linealmente dependiente de algunos factores que influyen a la carga. El modelo matemático se puede escribir como:

$$L(t) = Ln(t) + \sum a_i x_i(t) + e(t) \tag{24}$$

Donde $L(t)$ es la carga normal o estándar en un tiempo t, a_i son los coeficientes de variación lenta estimados, $x_i(t)$ son los diferentes factores que tienen influencia en el modelo tales como efectos ambientales, $e(t)$ es una componente de ruido blanco, n es el número de observaciones, usualmente 24 o 168.

La regresión lineal múltiple es un método muy popular y a menudo usado para el modelado y predicción afectación en cargas en función de diversos factores ambientales, crecimiento de capital, precios de la electricidad, crecimiento económico, etc. Este tipo de regresión se presenta cuando dos o más variables independientes influyen sobre una variable dependiente. El análisis de regresión múltiple utiliza la técnica de estimación de mínimos cuadrados.

El método de suavización o *suavización exponencial* simple puede considerarse como una evolución del método de promedio móvil ponderado, en este caso se calcula el promedio de una serie de tiempo con un mecanismo de autocorrección que busca ajustar los pronósticos en dirección opuesta a las desviaciones del pasado. La suavización exponencial es uno de los enfoques empleados para la estimación de cargas. En este método, la carga es modelada con datos previos, y es usado comúnmente para hacer predicciones futuras de carga. Este modelado por suavizado exponencial se ha empleado usando la siguiente función de ajuste

$$y(t) = \beta(t)Tf(t) + e(t) \tag{25}$$

Donde $f(t)$ es el vector de función de ajuste del proceso, $\beta(t)$ son coeficiente tés del vector, $e(t)$ es ruido blanco y T la transpuesta del operador.

2.4.2 Técnicas de series de tiempo

Las técnicas de series de tiempo están entre las más populares metodologías aplicadas al modelado. Las técnicas basadas en el supuesto de que los datos tienen una estructura interna, como autocorrelación, tendencia, o variación estacional. El primer ímpetu del enfoque es ensamblar los datos disponibles de coincidencia de patrones y luego obtener el valor previsto con respecto al tiempo utilizando un modelo establecido. Dentro de estas técnicas de modelado se encuentra el *modelo autorregresivo* (AR). El modelo AR puede ser empleado para modelar el perfil de carga si se asume una combinación lineal de las cargas previas; la cual es dada por Liu como (Liu, et al., 1996):

$$L_k = \sum_{i=1}^{m} a_{ik} \, L_{k-i} + e_k \tag{26}$$

Donde L_k, es la carga en un tiempo k, a_{ik}, $i = 1 \dots m$ son coeficientes desconocidos y sobre la ecuación dada es el modelo autorregresivo de orden m. En donde, los coeficientes desconocidos de la ecuación pueden ser obtenidos usando el algoritmo de mínimos cuadrados.

Por otra parte una variante del modelo AR es el *modelo autorregresivo de media móvil* (ARMA), el cual representa el valor actual de la serie de tiempo $y(t)$ de forma lineal en términos de sus valores en los valores pasados [$y(t-1), y(y-2)$ ...] y en términos de valores previos de ruido blanco [$a(t-1)$, $a(t-2), \dots$], por ejemplo, para el modelo ARMA de orden (p,q) el modelo se escribe como:

$$y(t) = \varphi_1 y(t-1) + \cdots + \varphi_p y(t-p) + a(t) - \varphi_1 a(t-1) - \cdots - \varphi_q (t-q) \qquad (27)$$

Den donde se emplea un esquema recursivo para identificar los parámetros, empleando métodos como mínimos cuadrados recursivos.

Además, otra técnica aplicada al modelado de cargas eléctricas ha sido el empleo de técnicas basadas en *máquinas de soporte de vectores* (SVM por sus siglas en ingles *Support Vector Machines*), que fue presentada por primera vez por Vapnik (Vapnik, 1998). Es un método basado en teoría de aprendizaje estadístico, el cual analiza los datos y reconoce patrones, usado para clasificación y análisis de regresión.

2.4.3 Técnicas de computación flexible

Es un hecho que cada sistema es de manera generalizada imprecisa, incierta y difícil de modelar con precisión. Un enfoque flexible son las técnicas de computación flexible (*Soft Computing*), las cuales se han sugerido para hacer frente a este tipo de modelos con eficacia y de manera más eficiente en el escenario de la investigación en las últimas décadas. El Soft Computing es un enfoque emergente que es paralelo a la notable capacidad de la mente humana para razonar y aprender en un entorno de incertidumbre e imprecisión. Está emergiendo rápidamente como una herramienta para ayudar a los sistemas inteligentes basados en computadoras que imitan la capacidad de la mente humana para emplear modos de razonamiento que son aproximados y no exactos. El tema básico de Soft Computing es que la precisión y certeza llevar a un costo y que los sistemas inteligentes deben explotar, siempre que sea posible, la tolerancia a la imprecisión e incertidumbre. El Soft Computing constituye un conjunto de disciplinas que incluyen la lógica difusa, redes neuronales, algoritmos evolutivos como los algoritmos genéticos (AG), etc.

Los sistemas basados en *lógica difusa* con técnicas de defusificación de centroide son bien conocidos en la identificación y aproximación a cualquier sistema dinámico a partir de un conjunto compacto para una precisión arbitraria. Se ha observado que los sistemas basados en lógica difusa tienen una gran capacidad en encontrar similitudes en conjuntos de datos de grandes proporciones.

Otra técnica empleada en el modelado son las *redes neuronales artificiales*, las cuales tienen una amplia aplicación gracias a su habilidad de aprendizaje. De acuerdo a Damborg, las redes neuronales ofrecen el potencial para superar la dependencia en forma funcional de un modelo (Damborg, et al., 1990). Existen diferentes tipos de redes neuronales: redes de perceptrón multicapa, redes auto-organizadas, etc. A su vez, existen múltiples capas ocultas en la red. En donde, por cada capa oculta puede haber varias neuronas. Las entradas son multiplicadas por pesos ω_i y son agregadas a un umbral θ para formar un número de producto interno llamado función de red.

Los *algoritmos genéticos* o programación evolutiva son usados para identificar los modelos autorregresivos de media móvil con variable exógena (ARMAX del inglés *Autoregressive Moving Average with Exogenous Variable*) para modelado de cargas. A través de la simulación del proceso evolutivo, el algoritmo ofrece una capacidad de converger hacia la extrema global de una superficie de error compleja. Estos son una técnica de búsqueda global que simula el proceso de la evolución natural y constituye un algoritmo de optimización estocástica. Dado que los algoritmos genéticos evalúan simultáneamente muchos puntos en el espacio de búsqueda y no necesitan asumir el espacio de búsqueda son capaces de asintóticamente converger hacia una solución óptima global, por lo tanto, puede mejorar la precisión de ajuste del modelo.

Finalmente se han propuesto *sistemas expertos basados en conocimiento* los cuales son técnicas que han emergido como resultado de los avances en el campo de la inteligencia artificial. Un sistema experto es un programa de computadora que tiene la habilidad de razonar, explicar y tener una base de conocimiento para expandir como nueva información. Para la construcción de modelos, el “conocimiento técnico” extrae conocimiento para la predicción por lo que se llama el componente base de conocimientos para el sistema experto. Este conocimiento se representa como hechos y reglas si-entonces, y está formado por el conjunto de las relaciones.

CAPITULO III

Metodología

3. METODOLOGÍA

Acorde con las necesidades descritas anteriormente, en la Fig. 9 se muestra la metodología propuesta para el siguiente trabajo de investigación. En la Fig. 9(a) se muestran los componentes principales que conforman el sistema de simulación PHIL. En primer lugar, se cuenta con el algoritmo de interfaz, el cual es el encargado de controlar como se intercambian las señales entre la interfaz virtual y la etapa de potencia del sistema de potencia; en base a este algoritmo se deben considerar cuestiones como la estabilidad y la precisión del sistema PHIL. En el algoritmo de interfaz se incluyen las partes del sistema en tiempo real y la etapa de potencia a utilizar. Respecto al sistema en tiempo real, este se encarga de producir una señal de corriente que emula a la señal de referencia la cual es generada a partir de un modelo por medio de un sistema de control en lazo cerrado. Mientras la etapa de potencia se conforma de un convertidor conmutado VSI junto con un filtro de potencia. Con la finalidad de obtener las señales de retroalimentación para el control en lazo cerrado se propone una etapa de acondicionamiento de señales de corriente y de voltaje. En la Fig. 9(b) se muestra el diagrama de bloques de las principales etapas para el desarrollo del sistema de simulación PHIL en donde una de las etapas principales para el desarrollo es del sistema de simulación es la selección o propuesta de un algoritmo de interfaz ya que de este depende la ley de control propuesta y el filtrado en la etapa de potencia. Además, parte importante del desarrollo del presente trabajo de investigación es la validación por medio de modelos matemáticos que permitan servir de referencia, por lo que se proponen tres casos de estudio en donde se tiene como primer objetivo validar la simulación PHIL mediante señales sintéticas con diferentes características, posteriormente usar modelos teóricos de cargas y por último proponer modelos basados en análisis experimental de máquinas eléctricas.

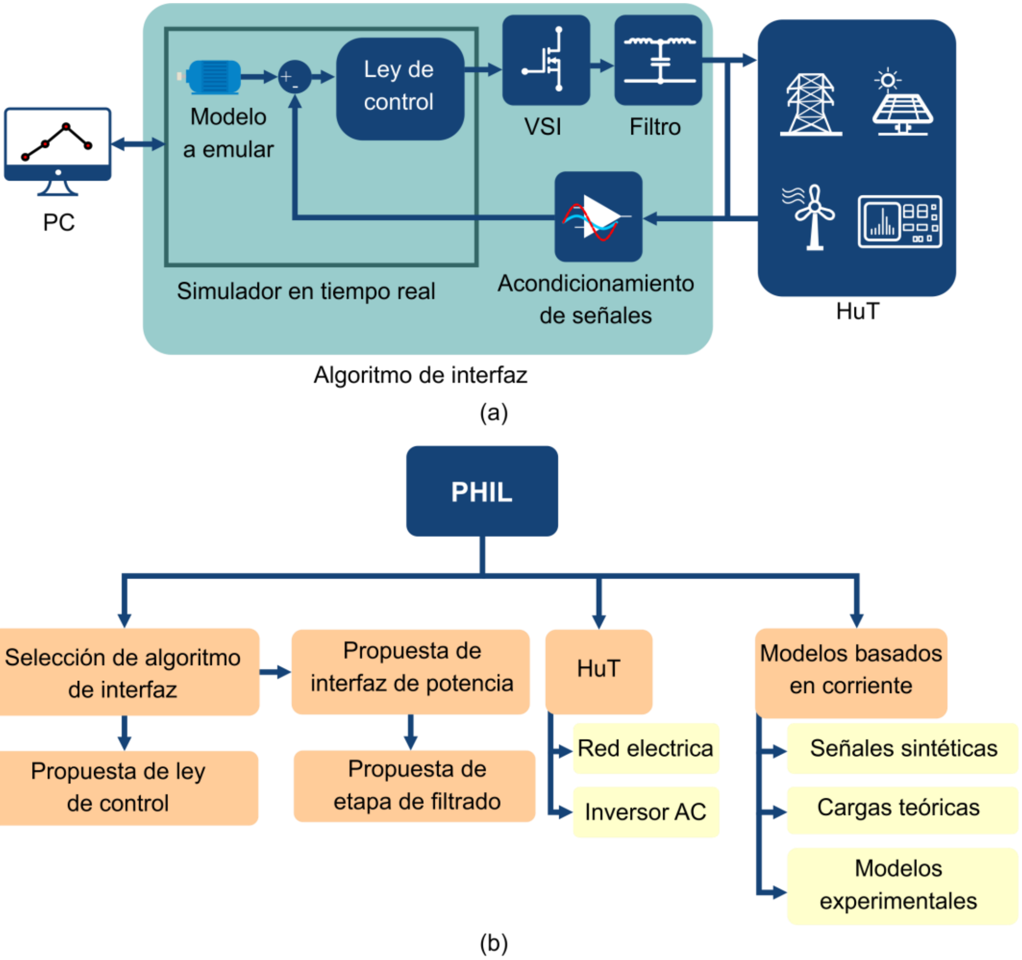

Fig. 9. (a) Diagrama general del sistema PHIL; (b) Metodología propuesta para la simulación PHIL.

3.1 Algoritmo de interfaz y ley de control

Uno de los algoritmos de interfaz más usados y simples de implementar es el modelo del transformador ideal como se menciona en la sección anterior. Por lo tanto, este algoritmo de interfaz es propuesto para el desarrollo del sistema PHIL propuesto en su configuración tipo corriente. Por lo tanto, en la Fig. 10 se muestra un esquema de las partes a implementar en el sistema virtual y los componentes en hardware necesarios para la emulación de corriente. En donde se implementa en el simulador en tiempo real la parte de retroalimentación filtrada con la finalidad de mejorar la estabilidad como lo sugiere (Mahdi, 2015), además del control del VSI el cual depende de la retroalimentación y la referencia del modelo, la parte del sistema virtual se ejemplifica con una fuente y una impedancia virtual la cual será el modelo del sistema o carga a emular. En la parte de hardware para sistemas de control tipo corriente se sugiere con el objetivo de hacer i_{HuT} lo más cercano posible a $i_{virtual}$. En este caso se propone para un simulador PHIL monofásico se emplea un convertidor de puente completo como se muestra en la Fig. 11, junto con un filtro LCL (L_{f1}-C_f-L_{f2}) para suprimir la alta frecuencia de los dispositivos de conmutación.

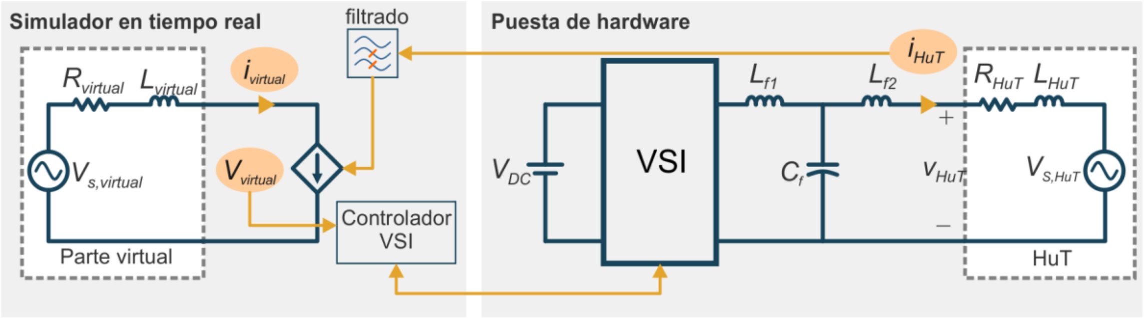

Fig. 10. Esquema de implementación práctica de simulación PHIL

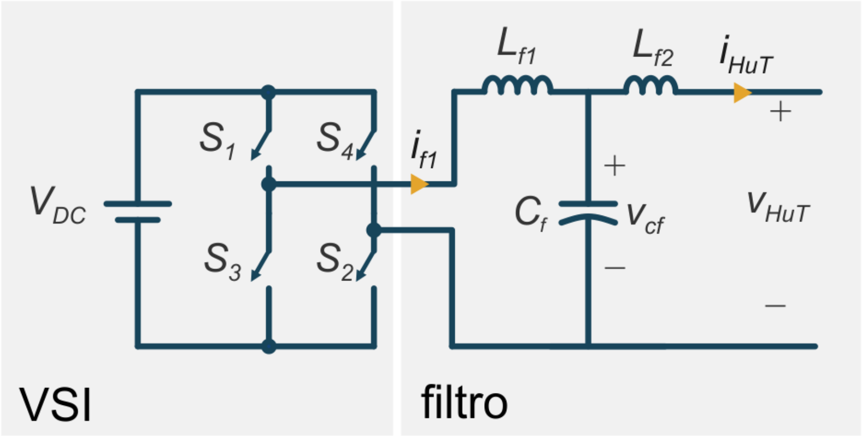

Fig. 11. Inversor de voltaje VSI con filtro LCL.

En este caso el lazo de control propuesto se basa en simulador que propone Mahdi (2015), el cual se basa en dos estrategias principales. En primer lugar, se propone que la frecuencia portadora v_p del control de los dispositivos de conmutación sea el doble de la frecuencia de muestreo *Fs*. Además, la retroalimentación para la ley de control propuesta se basa en espacio de estados, por lo tanto, como se muestra en la Fig. 12, x_c representa el vector de estados retroalimentados y x_{ref} es el vector de referencia, con los cuales se obtiene el vector de error el cual es multiplicado por la matriz *-K* para obtener uc, la cual es comparada con la señal portadora v_p, para obtener una conmutación SPWM de modo unipolar, en donde las salidas *ua* y *ub* son usadas para conmutar los dispositivos de potencia del VSI usando la siguiente lógica:

Si $u_a > 0$ entonces S1: ENCENDIDO, S4: APAGADO
Más si $u_a < 0$ entonces S1: APAGADO, S4: ENCENDIDO

Si $u_b > 0$ entonces S2: APAGADO, S3: ENCENDIDO
Más si $u_b < 0$ entonces S2: ENCENDIDO, S3: APAGADO

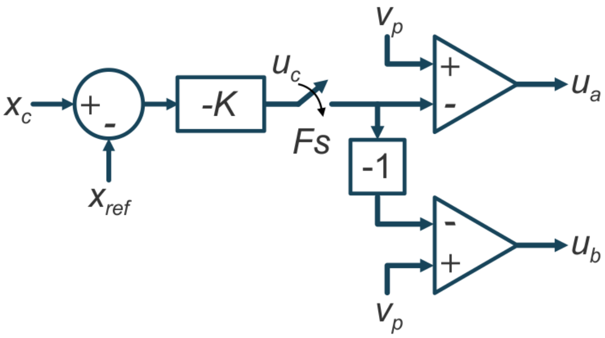

Fig. 12. Esquema de control del VSI

Entonces sabiendo que i_{f1} es la corriente que fluye por el inductor L_{f1}, que el voltaje en el capacitor C_f esta denotado por v_{cf}, y que la corriente i_{HuT} fluye por el inductor L_{f1}. Se define el vector de estados x_c como $[i_{f1}\ v_{cf}\ i_{HuT}]^T$ y asumiendo que la salida del inversor de voltaje es V_{dc}xu_c, la ecuación de espacio de estados se puede definir como:

$$\dot{x} = Ax + Bu_c \tag{28}$$

donde

$$A = \begin{bmatrix} 0 & -\frac{1}{L_{f1}} & 0 \\ \frac{1}{C_f} & 0 & \frac{1}{C_f} \\ 0 & \frac{1}{L_{f2}} & 0 \end{bmatrix}, B = \begin{bmatrix} \frac{V_{dc}}{L_{f1}} \\ 0 \\ 0 \end{bmatrix} \tag{29}$$

Como se nota el modelo del circuito solo usa los componentes del filtro sin embargo en este caso se considera L_{f2} como la impedancia equivalente debida al HuT, y no solo la inductancia del filtro. Entonces, el modelo en discreto se puede obtener para este sistema a una frecuencia de muestreo *Fs* el cual está dado por:

$$x(k+1) = Fx(k) + Gu_c(k) \tag{30}$$

donde:

$$F = e^{ATs}, G = \int_0^{Ts} e^{A(Ts-\tau)} B d\tau \tag{31}$$

En este sentido, se puede proponer un regulador cuadrático lineal en tiempo discreto como ley de control como se muestra a continuación:

$$u_c(k) = -K[x(k) - x_{ref}(k)] = -[k_1 \;\; k_2 \;\; k_3] \times [x(k) - x_{ref}(k)] \tag{32}$$

Donde x_{ref} es el vector de referencia para i_{f1}, v_{cf} y i_{HuT}, en donde la única referencia disponible es i_{HuT}, la cual es $i_{Virtual}$. En este caso es difícil definir las referencias i_{f1} y v_{cf} las cuales requerirían estimaciones adicionales. Más aún, ya que el seguimiento de corriente se debe realizar en base a $i_{Virtual}$, las otras dos variables deben contener su componente fundamental forzando las componentes de alta frecuencia a cero. En este sentido, una etapa de filtros pasa altas son incluidos en el lazo de corriente como se muestra:

$$\frac{i_{f1HP}}{i_{f1}} = \frac{s}{s+\alpha} = 1 - \frac{\alpha}{s+\alpha} \tag{33}$$

$$\frac{v_{cfHP}}{v_{cf}} = \frac{s}{s+\alpha} = 1 - \frac{\alpha}{s+\alpha} \tag{34}$$

La referencia de estados en este caso se formaría por x^T_{ref}= [$0\ 0\ i_{Virtual}$] y los estados estarían dados por x^T_c= [$i_{f1HP}\ v_{cfHP}\ i_{HuT}$]. Donde la ley de control se expresa como:

$$u_c(k) = -K[x_c(k) - x_{ref}(k)] = -[k_1\ \ k_2\ \ k_3] \times [x_c(k) - x_{ref}(k)] \tag{35}$$

Para investigar la estabilidad en la modificación de la ley de control se puede rescribir las equivalencias de los filtros pasa altas como la resta entre la señal original y las componentes de baja frecuencia i_{f1LP} y v_{cfLP}:

$$i_{f1HP} = i_{f1} - i_{f1LP} \tag{36}$$

$$v_{cfHP} = v_{cf} - v_{cfLP} \tag{37}$$

donde:

$$i_{f1LP} = \frac{\alpha}{s+\alpha} i_{f1} \tag{38}$$

$$v_{cfLP} = \frac{\alpha}{s+\alpha} v_{cf} \tag{39}$$

Por lo tanto, se incluyen i_{f1LP} y v_{cfLP} al vector de estados x_e = [$i_{f1}\ v_{cf}\ i_{HuT}\ i_{f1LP}\ v_{cfLP}$], en donde las ecuaciones en espacio de estados están dadas por:

$$\dot{x}_e = A_e x_e + B_e u_c \tag{40}$$

donde

$$A=\begin{bmatrix} 0 & -\frac{1}{L_{f1}} & 0 & 0 & 0 \\ \frac{1}{C_f} & 0 & -\frac{1}{C_f} & 0 & 0 \\ 0 & \frac{1}{L_{eq}} & -\frac{R_{eq}}{L_{eq}} & 0 & 0 \\ \alpha & 0 & 0 & -\alpha & 0 \\ 0 & \alpha & 0 & 0 & -\alpha \end{bmatrix}, B=\begin{bmatrix} \frac{V_{dc}}{L_{f1}} \\ 0 \\ 0 \\ 0 \\ 0 \end{bmatrix} \tag{41}$$

Donde R_{eq} y L_{eq} representan los parámetros equivalentes del HuT, en este caso la ley de control queda dada por:

$$u_c = -k_1[i_{f1HP}(k)-0]-k_2[v_{cHP}(k)-0]-k_3[i_{HuT}(k)-i_{Virtual}(k)] \tag{42}$$

Sustituyendo por las equivalencias del filtro pasa altas:

$$\begin{aligned} u_c &= -k_1 i_{f1}(k)-k_2 v_c(k)-k_3 i_{HuT}(k)+k_1 i_{f1LP}(k)+k_2 v_{cfLP}(k)+k_3 i_{Virtual}(k) \\ &= -K_e x_e(k)+k_3 i_{Virtual}(k) \end{aligned} \tag{43}$$

donde $K_e = [k_1\ k_2\ k_3\ -k_1\ -k_2]$. En donde la tarea principal es obtener los valores de las ganancias K_e.

*

3.2 Filtro LCL

Con referencia al filtro LCL empleado en el sistema PHIL su función principal es eliminar las componentes de alta frecuencia debidas a la conmutación del VSI, también, a partir de los componentes utilizados depende la estabilidad del sistema PHIL. Sin embargo, en aplicaciones de lazo cerrado de corriente de filtros LCL se tienen algunas recomendaciones ya que, a diferencia de los filtros LC, este filtro cuenta con una frecuencia de resonancia, la cual si no se toma en consideración puede afectar el desempeño del PHIL amplificando componentes frecuenciales no deseadas, en la Fig. 13 se muestra el circuito del filtro LCL junto con la respuesta en frecuencia del filtro. Esta respuesta en frecuencia se obtiene a partir del modelo continuo del filtro que se muestra a continuación:

$$G(s) = \frac{i_{HuT}}{V_{dc} \times u_c} = \frac{1}{L_{f1} L_{f2} C_f s^3 + s(L_{f1} + L_{f2})} \tag{44}$$

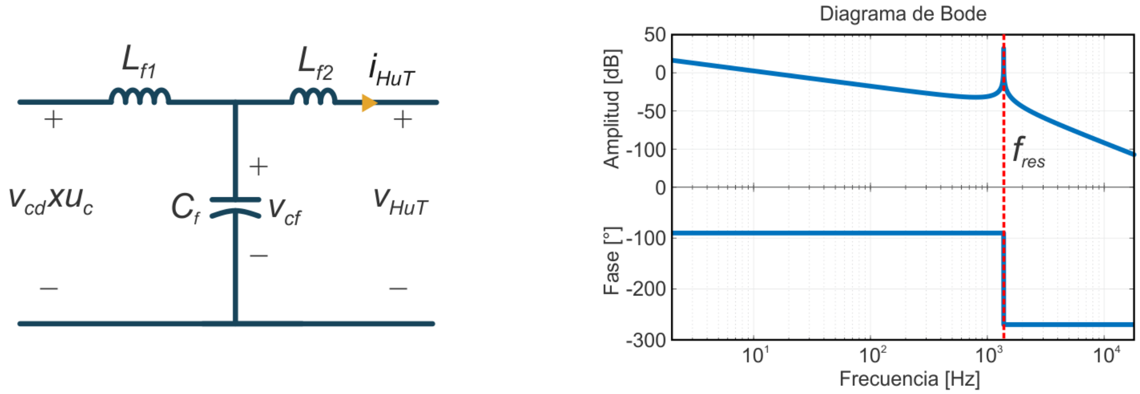

(a) (b)

Fig. 13 (a) Filtro LCL; (b) Diagrama de Bode de filtro LCL.

Existen diversas recomendaciones para la propuesta de un filtro LCL que tienen como objetivo la atenuación de armónicos de altas frecuencias. En este sentido se han presentado algunas consideraciones para la propuesta de filtros LCL enfocados al seguimiento de frecuencia (Li, 2011). En primer lugar, el valor general de inductancia $L_s=L_{f1}+L_{f2}$ se puede elegir en base a la frecuencia de conmutación fc, la corriente pico $i_{HuT,\,p}$, la corriente de rizado, i_r, la cual se establece a un 20% de la corriente pico. Entonces se sugiere:

$$\frac{V_{dc}}{4\sqrt{3} i_r f_c} \leq L_s \leq \frac{\sqrt{V_{dc}{}^2 - E_m{}^2}}{\omega I_{HuT,p}} \tag{45}$$

En segundo lugar, el valor de la capacitancia se elige en base a la potencia reactiva que genera, con el objetivo de evitar valores de factor de potencia bajos, en este sentido la potencia reactiva del capacitor Q_c debe ser menor que el 5% de la potencia nominal del sistema.

$$Q_c \le \frac{0.05 \cdot P_n}{3 \cdot 2\pi \cdot f_n \cdot {E_n}^2} \tag{46}$$

Donde f_n es la frecuencia nominal, E_n el valor RMS de voltaje y P_n es la potencia del sistema. Finalmente, se sugiere una relación de los valores de inductancias Lf1, y Lf2. La cual se selecciona de acuerdo a la frecuencia de atenuación que se desea obtener fa, obteniendo un factor r el cual se define como Lf1/Lf2. Entonces se propone la siguiente ecuación en donde se consideran las soluciones positivas para r:

$$ {f_a}^2 + (2{f_a}^2 + 1 - f_a {\omega_c}^2 L_s C_f)r + f_a + 1 = 0 \tag{47}$$

Donde ω_c es $2f_c$, entonces obteniendo *r* se puede estimar Lf1 y Lf2:

$$L_{f1} = \frac{L_s}{1+r} \tag{48}$$

$$L_{f2} = rL_s \tag{49}$$

En este caso es necesario revisar la frecuencia de resonancia la cual debe satisfacer el siguiente criterio:

$$10 f_n \le f_{res} \le 0.5 f_c \tag{50}$$

3.3 Convertidor VSI

Aunque el comportamiento del inversor VSI es reversible este debe ser alimentado con una fuente especial, que opere en cuatro cuadrantes, o en su defecto proponer el uso de un convertidor “back-to-back” el cual transforma la energía CA-CD-CA, lo cual es de utilidad para generar un comportamiento completamente reversible del sistema PHIL. En este caso se propone el uso de equipo de laboratorio ya que incluye los dispositivos de protección adecuados en caso de generar escenarios de inestabilidad. En el caso de la fuente de cuatro cuadrantes se emplea un equipo de Lab-Volt 8960-22, que puede proporcionar alimentación de CD variable hasta de ±150 V a ±5 A. El inversor de potencia VSI lo conforma un equipo de laboratorio marca Lab-Volt 8837-B2 el cual cuenta con tres ramas de dos elementos de conmutación IGBT, este inversor soporta un voltaje de CD de 420 V a 6 A, con un ancho de banda de conmutación de 0 a 20 kHz, en la Fig. 14 se muestran los diagramas de la configuración empleada junto con los componentes utilizados.

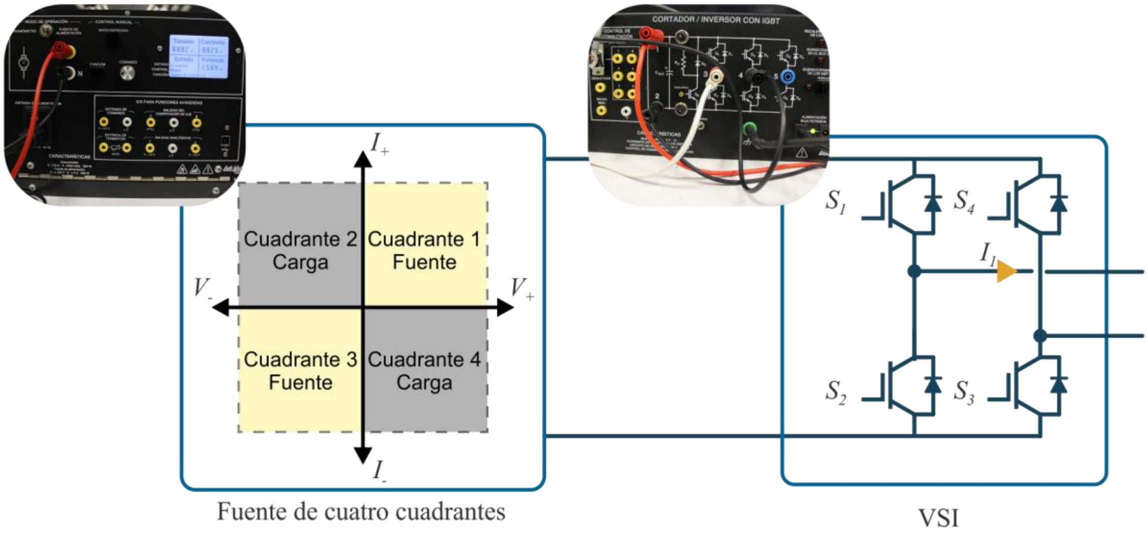

Fig. 14. Fuente de cuatro cuadrantes conectado a VSI.

3.4 Sistema en tiempo real

El sistema en tiempo real para adquisición de datos y la interfaz de control lo conforma un controlador de la marca dSPACE RTI1103 cual se el cual es una plataforma software/hardware basada en un procesador PowerPC 750GX de 32 bits que opera a una frecuencia de reloj de 1GHz, el cual opera en conjunto con procesador digital de señales (DSP por sus siglas en ingles *digital signal processor*) de Texas Instruments TM320F240. La plataforma incluye diversos periféricos como: 50 entradas y salidas digitales I/O de alta velocidad, 36 canales de convertidor analógico-digital ADC de 16 bits, 8 canales de convertidor digital analógico DAC de 16 bits de resolución, salidas PWM, interfases de comunicación serial RS232, RS422, SPI, etc. Una de las principales ventajas del sistema dSPACE es que permite el prototipado rápido de sistemas de control, ya que ofrece una plataforma compatible con el entorno de desarrollo a bloques de Simulink, donde se puede configurar gráficamente los puertos de entrada y salida por medio de bloques facilitando la implementación de diferentes funciones en la plataforma. En la Fig. 15 se muestra en conjunto el sistema en tiempo real junto con la etapa de potencia anteriormente descrito.

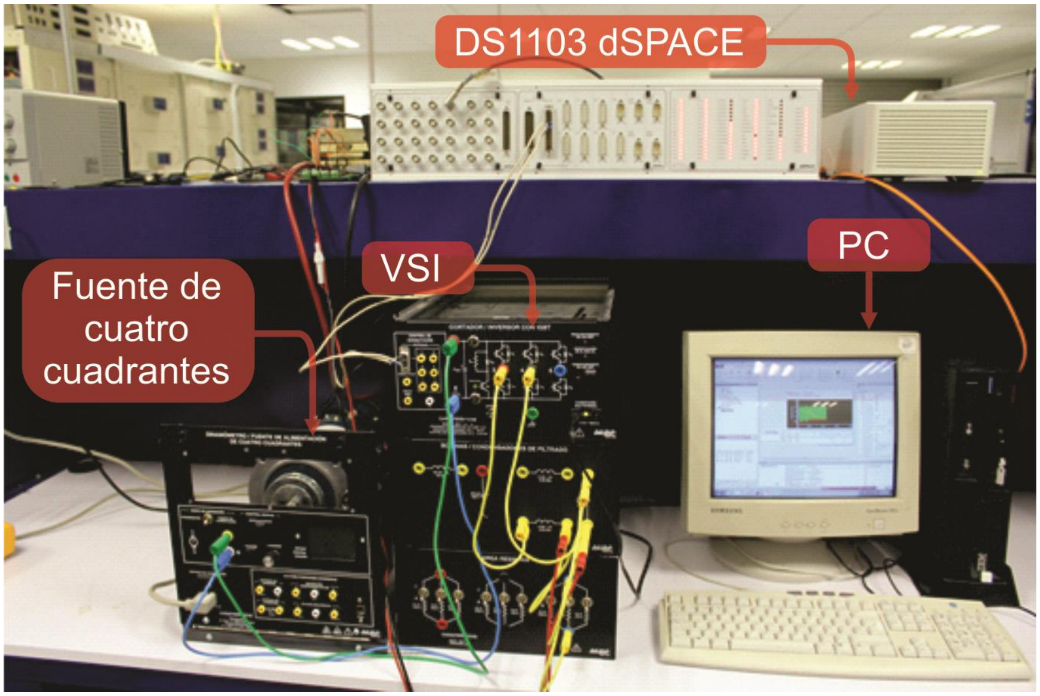

Fig. 15. Plataforma DS1103 dSPACE junto con VSI y fuente de cuatro cuadrantes.

3.5 Casos de estudio de simulación PHIL

Para el caso de la validación del sistema de simulación PHIL propuesto se propones tres escenarios para su posible validación. En donde se busca a su vez generar un aporte científico en las diferentes áreas de aplicación del sistema propuesto, para lo cual se presentan los siguientes casos de estudio:

- CASO 1: Validación del sistema PHIL por medio de señales sintéticas.
- CASO 2: Uso de cargas a partir de modelos teóricos.
- CASO 3: Uso de cargas por medio de modelos experimentales.

3.5.1 Señales sintéticas

En esta etapa se tiene como objetivo la puesta en marcha del sistema de simulación PHIL, por lo cual una manera sencilla de validación es a través de señales sintéticas para las cuales se consideran tanto en la simulación e implementación del sistema, en donde se consideran tres casos particulares como

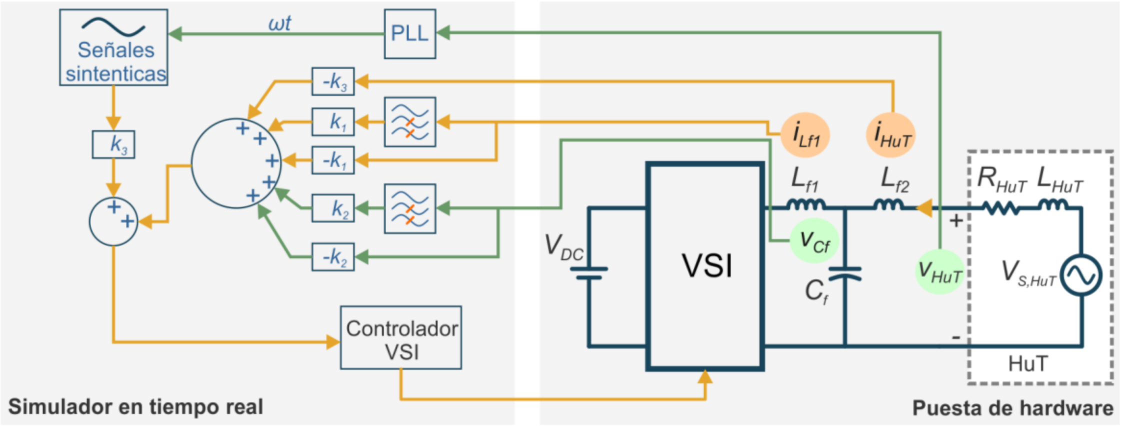

Fig. 16 Implementación de simulación PHIL mediante señales sintéticas.

se muestra en la Fig. 16, en primer lugar, una señal senoidal pura, posteriormente una señal con variaciones de tipo escalón de magnitud y por último una señal con contenido armónico, estas señales representan la corriente de referencia a emular y se sincronizaran con el voltaje de alimentación por medio de un algoritmo de amarre de fase (PLL, por sus siglas en ingles *phase-locked loop*) .

3.5.2 Cargas basadas en modelos teóricos

Una de las potenciales aplicaciones del sistema propuesto es poder emular el comportamiento eléctrico de una máquina eléctrica rotativa; sin embargo, en realidad se puede emular algún otro tipo de carga, por lo tanto, se propone utilizar algunos modelos teóricos como se muestra en la Fig. 17, con la finalidad de validar el sistema con diferentes condiciones que ofrecen los diferentes tipos de cargas, tales como desfase entre el voltaje y la corriente o la introducción de componentes armónicas debido a las cargas no lineales. En este caso las cargas no se sincronizan con el PLL como la simulación por señales sintéticas, sino que se utilizan mediciones de voltaje en el punto de conexión con el sistema PHIL para que la alimentación de las cargas virtuales sea la alimentación real del HuT.

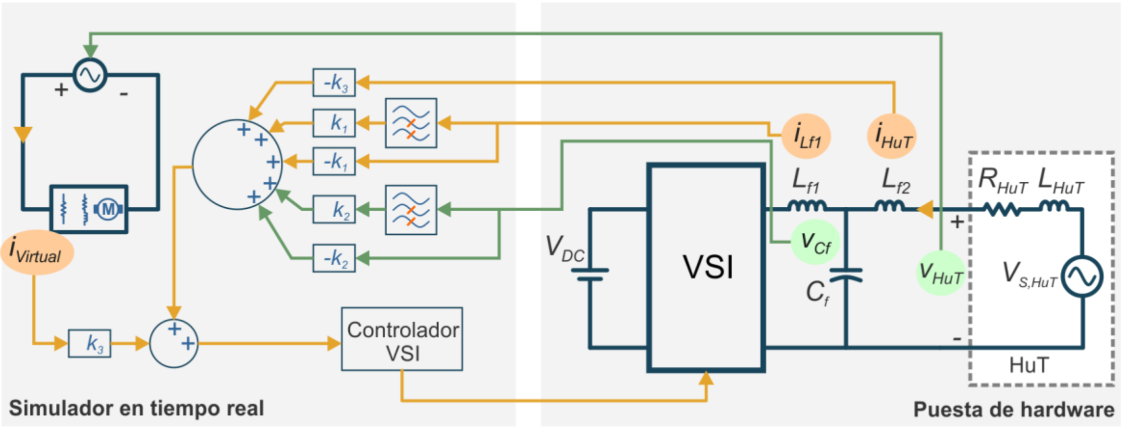

Fig.17. Implementación de simulación PHIL mediante cargas teóricas.

3.5.3 Modelo experimental de motor de inducción

Una de las potenciales aplicaciones del sistema de simulación PHIL propuesto es emular el comportamiento eléctrico de una máquina eléctrica rotativa bajo diferentes condiciones de operación incluidas diferentes condiciones de falla. Esto es debido a la importancia con que cuentan los motores de inducción aunado a la importancia que tienen el diagnostico de condiciones de falla en estas máquinas. En este sentido se propone el desarrollo de un modelo teórico de un motor de inducción bajo diferentes condiciones de falla de corto circuito junto con diferentes condiciones de carga mecánica, lo cual es una condición común en los ambientes industriales y apega más a la realidad la propuesta en la aplicación de validación de sistemas de diagnóstico de máquinas eléctricas. En este sentido se tomó en cuenta la integración del modelo propuesto al sistema PHIL como se muestra en la Fig. 18. sincronizado al HuT mediante un PLL.

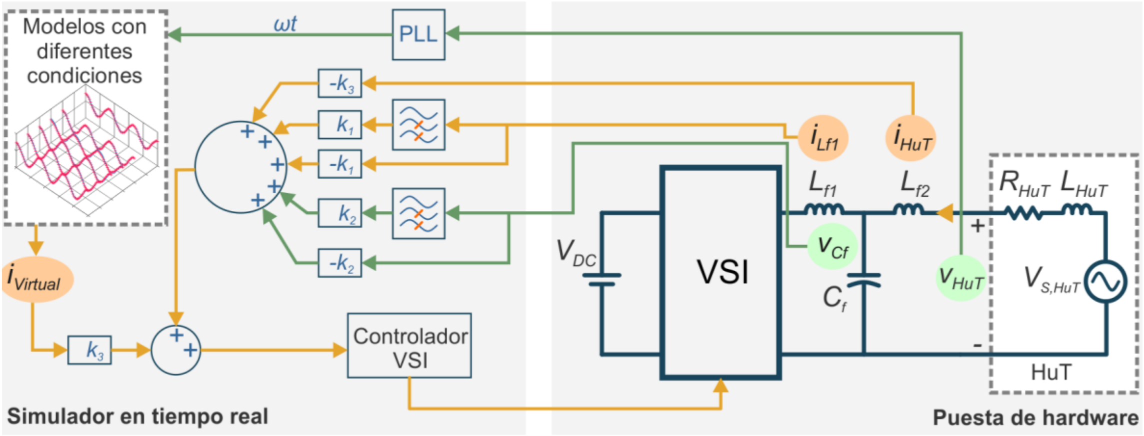

Fig. 18. Implementación de simulación PHIL mediante modelos experimentales.

El modelo propuesto se llevará a cabo de manera experimental mediante el monitoreo de corriente bajo las diferentes condiciones de cortocircuito en un motor de inducción de 2 HP como se muestra en la Fig. 19(a). En donde se cuentan con diferentes taps conectados a diferentes vueltas del devanado estatórico de una sola fase con el objetivo de producir cortocircuitos con diferente número de vueltas del devanado (5, 10, 15, 20 y 30 vueltas). Adicionalmente, diferentes condiciones de carga mecánica se consideraron por medio de un dinamómetro (sin carga, un tercio de carga, un sexto de carga y carga plena), como se muestra en las señales de corrientes obtenidas en la Fig. 19(b). Por lo tanto, sabiendo que la falla de cortocircuito en devanados no afecta solamente a motores propone el análisis y modelado de corriente de un transformador eléctrico cuyo circuito equivalente es muy similar al que se encuentra en un motor de inducción, además de la importancia que tiene en la comunidad científica ya sea para el diseño de protecciones o la discriminación de la falla.

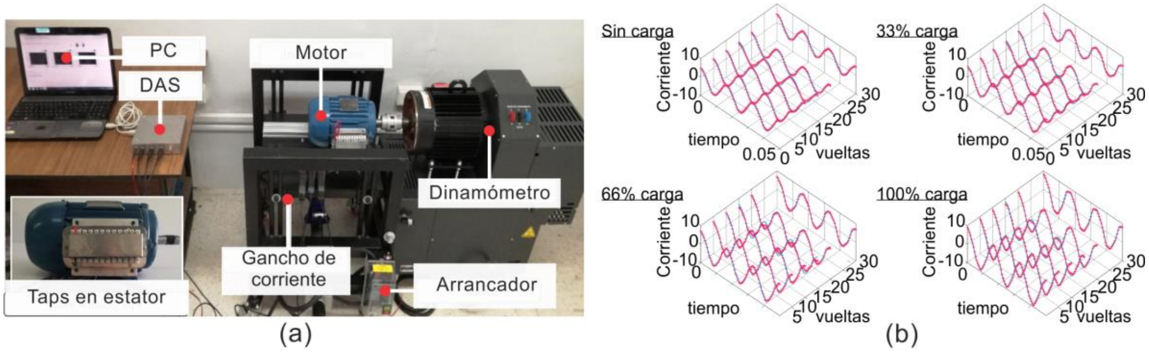

Fig. 19(a). Puesta experimental motor de inducción; (b) Señales experimentales de corriente bajo diferentes condiciones de operación.

3.5.4 Modelo experimental de motor de transformador

Como un caso adicional a este proyecto se realiza un análisis experimental a un transformador, esto debido a la importancia de la presencia de las condiciones de falla tanto en motores de inducción como en transformadores, aunado a la semejanza del circuito equivalente monofásico de un motor de inducción con un transformador. En este sentido se propone el monitoreo en un transformador con diferentes condiciones de cortocircuito (2, 3, 4, 5, 10, 15, 20, 25, 30, 35 y 40) como se muestra en la Fig. 20(a), en donde se considera la condición de magnetización del núcleo obteniendo diferentes señales de corriente de energización como se muestra en la Fig. 20(b).

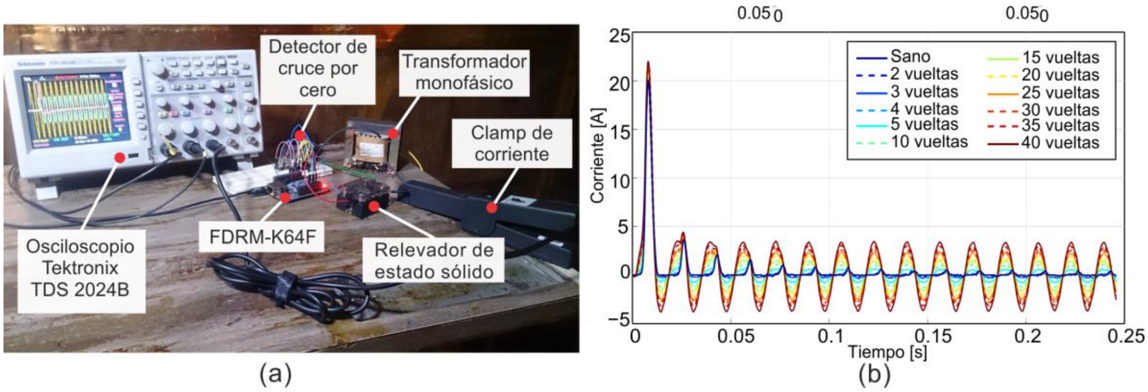

(a) (b)

Fig. 20(a). Puesta experimental motor de transformador; (b) Señales experimentales de corriente bajo diferentes condiciones de falla.

CAPITULO IV

Resultados

4. Resultados

A continuación, se presentan los resultados obtenidos del trabajo de investigación propuesto, en donde, en primera instancia se llevó a cabo la puesta en marcha del sistema PHIL, el cual se simuló por medio de los parámetros en espacio de estados que se proponen en el modelo del inversor junto con el filtro LCL en (44). En donde en primer lugar se deben establecer los valores de los parámetros a utilizar en el sistema, así como las ganancias de la ley de control propuesta; para esto se implementó en Matlab una interfaz gráfica de usuario (GUI, por sus siglas en inglés *Graphic User Interface*) como se muestra en la Fig. 20(a), en donde el criterio principal tomado en cuenta para la sintonización se basa en la estabilidad del sistema por medio de la posición de los eigenvalores los cuales deben encontrarse dentro del área de estabilidad indicada con un circulo unitario. Además, se observa la respuesta escalón en lazo cerrado en donde se puede observar el error en estado estable del sistema en donde, las ganancias de la ley de control se varían hasta obtener una respuesta deseada. Adicionalmente se muestra la respuesta en frecuencia del filtro LCL en base a los parámetros de entrada, esto con la finalidad de que el usuario este consiente de la frecuencia de resonancia del filtro y en base a esto proponer los valores de frecuencia de muestreo y la frecuencia de conmutación del inversor. Por otra parte, se llevó a cabo la implementación del sistema de simulación PHIL en el entorno Simulink de Matlab en donde se incluye la simulación de la etapa de potencia por medio de un inversor de puente completo y el filtro LCL junto con un HuT el cual está conformado por una fuente de alimentación sinusoidal junto con una resistencia, así como la ley de control con las ganancias obtenidas a través de la GUI como se muestra en la Fig. 21(b). Entonces, se obtiene una comparativa entre la señal de referencia que representa la corriente a emular por el PHIL y la señal de corriente medida en el punto de conexión entre el PHIL y el HuT en la Fig. 21(c) se muestran ambas señales en donde se obtiene un factor de ajuste aproximado del 97%. Adicionalmente los parámetros utilizados

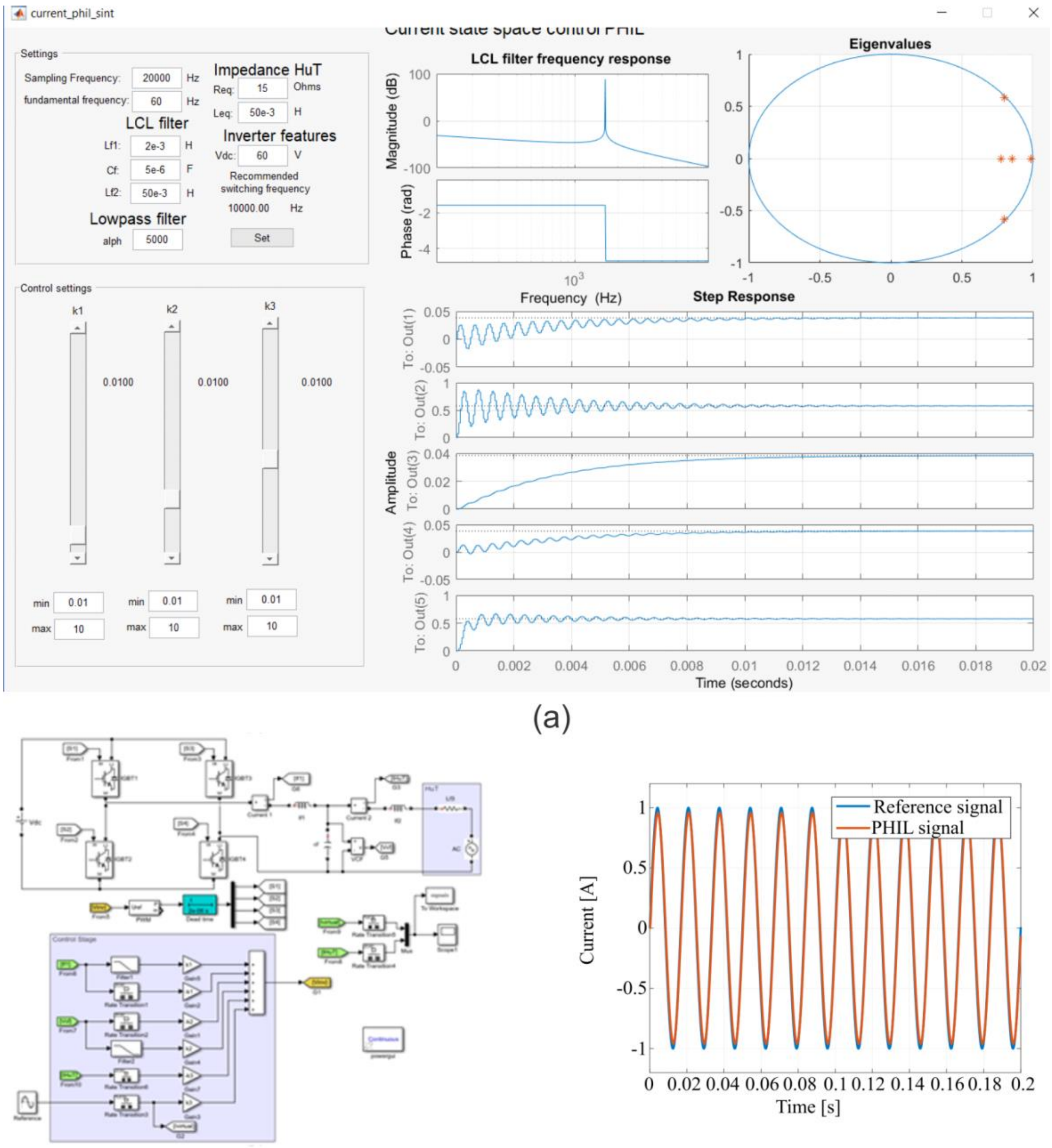

current_phil_sint

Settings
Sampling Frequency: 20000 Hz
fundamental frequency: 60 Hz

LCL filter
Lf1: 2e-3 H
Cf: 5e-6 F
Lf2: 50e-3 H

Lowpass filter
alph 5000

Impedance HuT
Req: 15 Ohms
Leq: 50e-3 H

Inverter features
Vdc: 60 V
Recommended switching frequency 10000.00 Hz

Control settings
k1 0.0100 min 0.01 max 10
k2 0.0100 min 0.01 max 10
k3 0.0100 min 0.01 max 10

(a)

(b)

(c)

Fig. 21. (a) GUI para sintonización de ley de control; (b) Implementación en Simulink de sistema PHIL; (c) Corriente de referencia y corriente obtenida del PHIL.

para la simulación se resumen en la Tabla I, en donde se muestran los valores de los componentes del filtro LCL empleado junto con la impedancia del HuT, la frecuencia de corte del filtro digital empleado, las frecuencias de muestreo y conmutación, así como las ganancias de la ley de control seleccionadas.

Tabla I. Parámetros de simulación

Parámetro	**Valor**
L_1	4 mH
C	5 uF
L_2	8 mH
R_{eq}	15 Ω
L_{eq}	8 mH
α	5000 rad/s (800 Hz)
F_s	12 kHz
F_{pwm}	6 kHz
V_{dc}	60 V
$k1$	1.5
$k2$	0.1
$k3$	3.8

4.1 Puesta en marcha de PHIL

La puesta en marcha del simulador PHIL se llevó a cabo mediante los componentes descritos en la sección anterior, en la Fig. 22 se muestra el sistema integrado junto con los componentes HuT utilizados para la validación los cuales constan de la red eléctrica de las instalaciones del laboratorio de eléctrica del Instituto Tecnológico Superior de Irapuato, la cual es aislada y reducida por medio de un autotransformador y aislada mediante un transformador monofásico a niveles de tensión RMS de 35 V, con el objetivo de tener un sistema a escala. Por otra parte, un inversor aislado conectado a una batería de ciclo profundo fue empleado de igual forma como HuT, con la finalidad de observar el efecto de la emulación ante diferentes fuentes de alimentación. Algunas consideraciones realizadas para la implementación práctica fue adicionar impedancia en serie, por medio de una resistencia de 15 Ω, lo cual se usa como estrategia de mejorar la estabilidad del sistema ya que se aumenta la impedancia del HuT, sin embargo, agregar este tipo de impedancias limita la capacidad máxima de corriente. En la Tabla II se muestran los parámetros empleados para la implementación práctica del simulador PHIL.

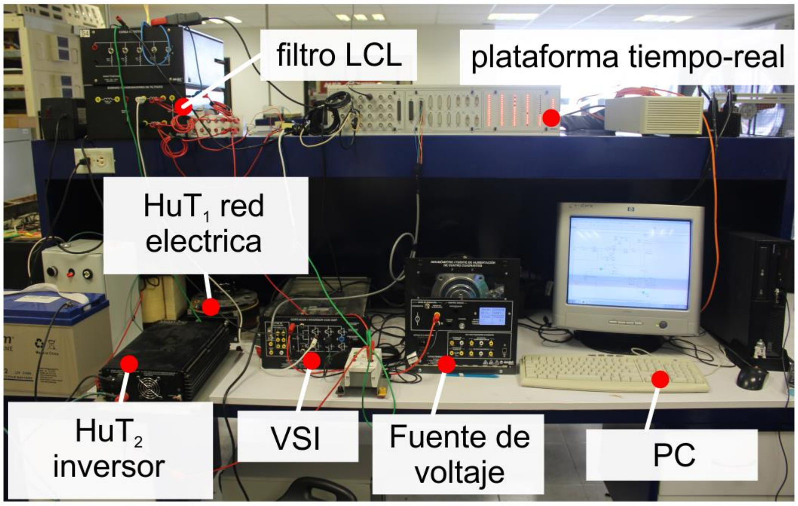

Fig. 22. Puesta experimental del sistema PHIL para emulación de cargas.

Tabla II. Parámetros de puesta experimental

Parámetro	**Valor**
L_1	4 mH
C	5 uF
L_2	8 mH
R_2	15 Ω
α	5000 rad/s (800 Hz)
F_s	18 kHz
F_{pwm}	9 kHz
V_{dc}	60 V
$k1$	1.1
$k2$	0.046
$k3$	1.6

4.2 Simulación PHIL mediante señales sintéticas

En el caso de la simulación por medio de señales sintéticas se implementó una señal sinusoidal pura y un caso de señal sinusoidal con contenido armónico como se muestra en la Fig. 23. Como se observa en la Fig. 23(a) la señal sinusoidal pura tiene un ajuste del 94% respecto a la señal de referencia, sin embargo, el espectro obtenido muestra la presencia de contenido armónico en la señal de corriente emulada que, aunque es de magnitud pequeña como se muestra en la Fig. 23(b). Entonces, aunque la señal de referencia se considera una señal pura por medio de la sincronización mediante el PLL, el contenido armónico del voltaje proporcionado por el HuT afecta a la señal a emular del simulador PHIL. Por otra parte, una señal rica en contenido armónico fue evaluada mediante el sistema PHIL de igual forma se observa que aunque se obtienen ajustes superiores al 80%, la magnitud de los armónicos se ve de alguna forma afectada, esto se puede deber al igual que en el caso anterior que aunque se proponen diferentes amplitudes de armónicos, la amplitud y fase de los armónicos propios de la fuente de voltaje del

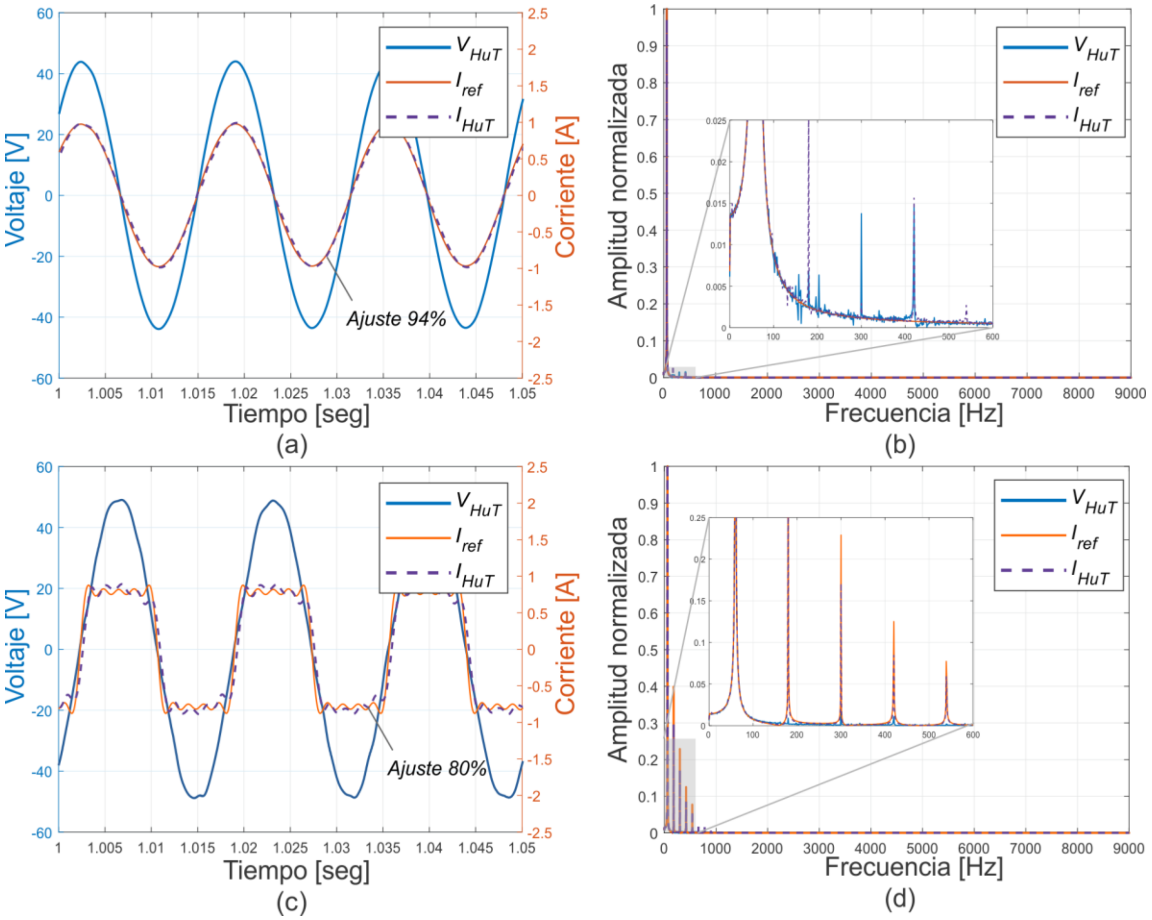

Fig. 23. Validación por medio de señales sintéticas de sistema PHIL: (a) Señal sinusoidal sintética; (b) Espectro señal sintética sinusoidal; (c) Señal con armónicos; (d) Espectro de señal con armónicos.

HuT puede afectar el desempeño del simulador PHIL, en este tipo de conexión. En la Tabla III se resumen los errores porcentuales entre las componentes de amplitud en las pruebas de las señales sintéticas, como se observa las componentes fundamentales presentan un error bastante bajo, sin embargo, en el caso de las componentes armónicas el error está por debajo del 31.7%

Tabla III. Error porcentual de amplitud por armónico para señales sintéticas.

Armónico		1	3	5	7	9
Error [%]	Senoidal sintética	2.9	-	-	-	-
	Señal sintética con armónicos	0.5	25.6	25.1	31.7	22.7

4.3 Simulación PHIL mediante cargas teóricas

Se implemento la simulación PHIL de modelos de cargas teóricas por medio de tres diferentes cargas que ofrecen diferentes tipos de comportamiento en fase y armónicos, por medio de tres diferentes cargas virtuales: una carga resistiva de 45Ω, una carga RL con una resistencia de 20Ω y una inductancia de 50mH, así como una carga no lineal conformada por una fuente lineal de CD junto con un motor de corriente directa con corriente nominal de 0.8 A. Estas cargas fueron evaluadas mediante dos HuT como se muestra en las Fig. 24 y Fig. 25. En primer lugar, se obtienen los resultados para el HuT1, el cual consiste como se menciona anteriormente en la red eléctrica junto con un transformador de aislamiento y un autotransformador en modo reductor, como se muestra en la Fig. 24(a) el comportamiento de la carga resistiva está en fase con el voltaje de la fuente como se espera obteniendo un ajuste por encima del 95%, adicionalmente se puede observar el comportamiento armónico, en donde dado que el voltaje de alimentación contiene componentes armónicas estas se ven reflejadas en la señal de referencia, sin embargo como se muestra en la Fig. 24(b), existe un mayor error en las componentes armonices; de igual forma al realizar la simulación de una carga RL virtual se observa que se obtiene el desfase esperado respecto al voltaje como se observa en la Fig. 24(c), igualmente las componentes armonices se ven afectadas aun que se obtiene un ajuste del 96% como se ve en la Fig. 24(d); En el caso de la carga representada por un motor de DC se obtiene un ajuste del 71% como se muestra en la Fig. 23(e), sin embargo al presentar alto contenido armónico, los

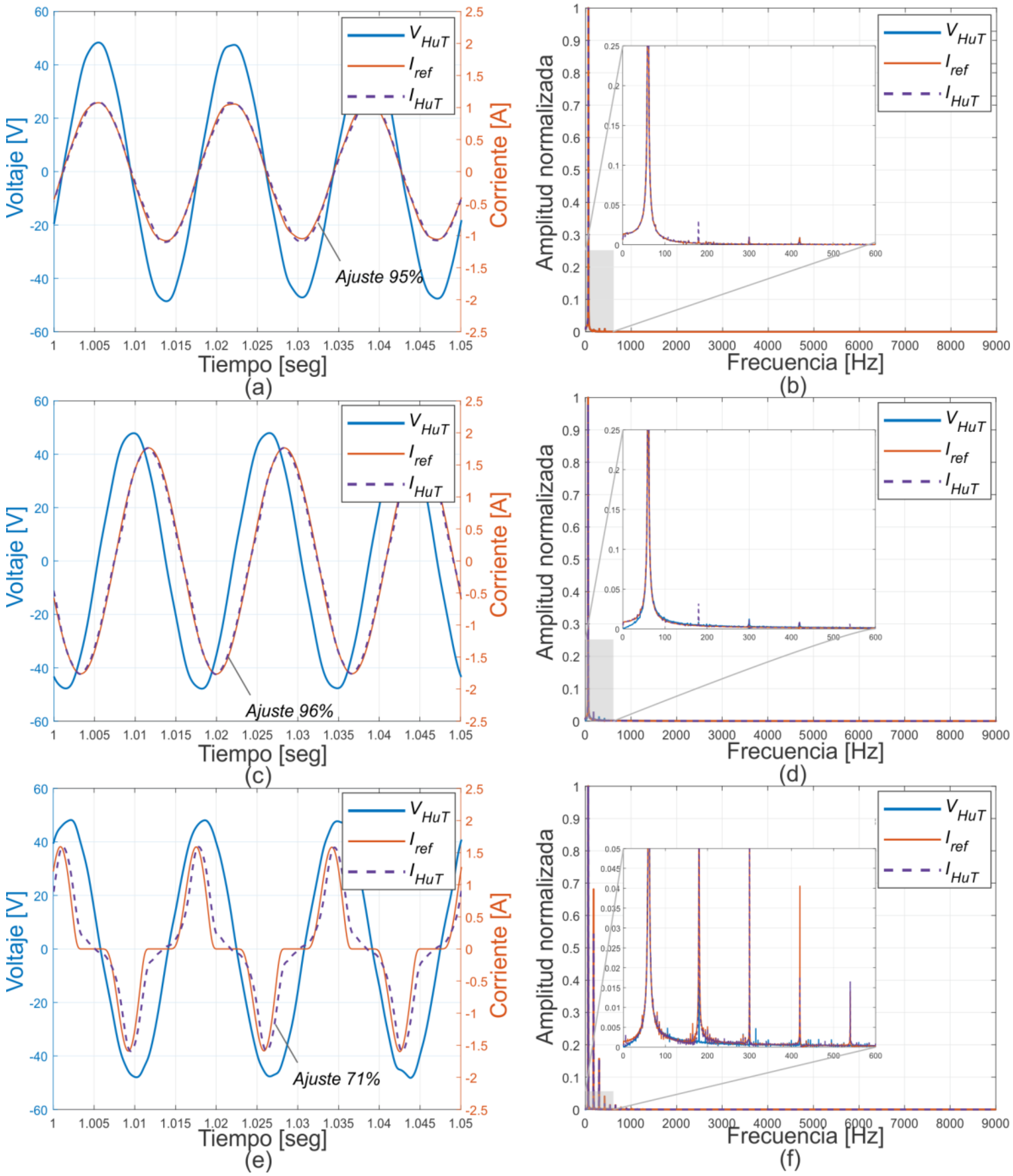

Fig. 24. Simulación cargas teóricas HuT$_1$: (a) Carga resistiva; (b) Espectro de carga resistiva; (c) Carga RL; (d) Espectro de carga RL; (e) Motor de CD; (f) Espectro de Motor de CD.

errores presentados en las componentes armónicas son más bajas que los casos de las cargas anteriores. En segundo lugar, se realiza la simulación PHIL por medio de un inversor junto con una batería de ciclo profundo que genera un voltaje nominal

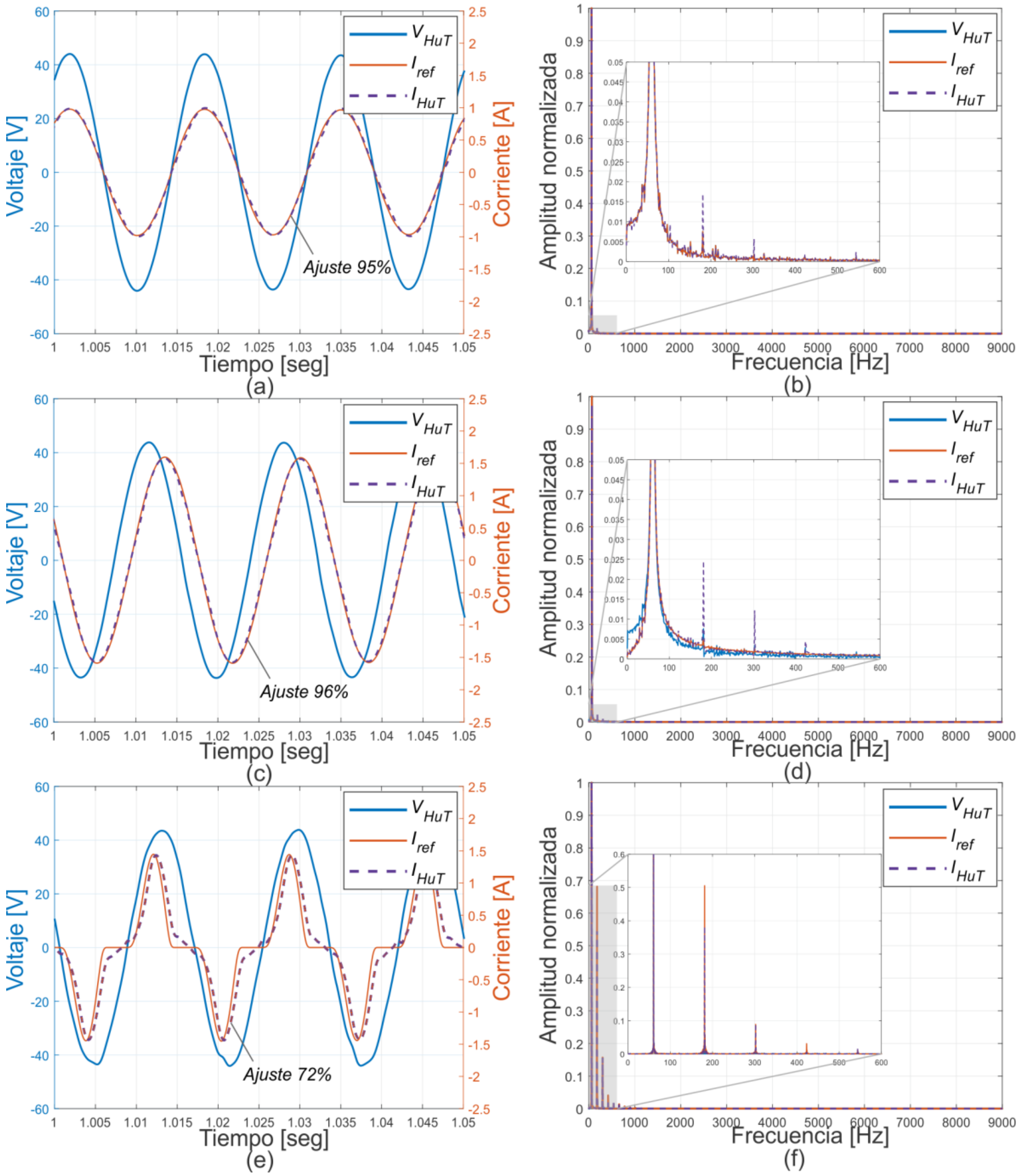

Fig. 25. Simulación cargas teóricas HuT$_2$: (a) Carga resistiva; (b) Espectro de carga resistiva; (c) Carga RL; (d) Espectro de carga RL; (e) Motor de DC; (f) Espectro de Motor de DC.

a la salida de 127V y al igual que la conexión a la red, es conectado a un transformador de asilamiento y a un autotransformador para reducir el voltaje de alimentación a 35Vrms, en este caso los resultados son simulares en cuestión de ajuste de la señal del PHIL con la señal de referencia, presentando errores de 95%, 96% y 72% para las señales de carga resistiva, RL y motor de CD, como se muestra en las Fig. 25(a), (c) y (e), aunque en este caso las componentes armónicas en el voltaje son mayores respecto al HuT1, como se muestra en las Fig. 25(b), (d) y (f), en la Tabla IV se muestran los porcentajes de error para las diferentes cargas para el HuT 1 y 2, en este caso se presenta errores simulares en el comportamiento armónico sin embargo en la componente fundamental el error es bajo.

Tabla IV. Error porcentual de amplitud por armónico para modelos teóricos.

Armónico			1	3	5	7	9
HuT$_1$	Error [%]	Carga Resistiva	0.02	454.8	17.2	10.3	88.4
		Carga RL	2.2	701	164	490.7	244
		Carga Motor DC	7.5	20.1	0.2	52.6	27.5
HuT$_2$	Error [%]	Carga Resistiva	0.2	123	214	27	100.5
		Carga RL	2.6	403	366	175	5.6
		Carga Motor DC	5.7	20	7	60	47

4.4 Simulación PHIL mediante modelos experimentales

Una propuesta del presente trabajo de investigación es el desarrollo de un modelo genérico para la emulación de un motor de inducción bajo diferentes condiciones de operación, por medio de diferentes niveles de carga, así como diferentes condiciones de falla de corto circuito, en donde como se muestra en la Fig. 26 se obtiene un modelo neuronal monofásico de la corriente el cual tiene como entrada el número de vueltas de cortocircuito así como el nivel de carga mecánica el cual genera las salidas de amplitud, fase y frecuencia de contenido armónico e inter-armónico. En la Fig. 27 se muestran los resultados obtenidos de la simulación PHIL para todas las condiciones propuestas de nivel de carga (en vacío, 33% de

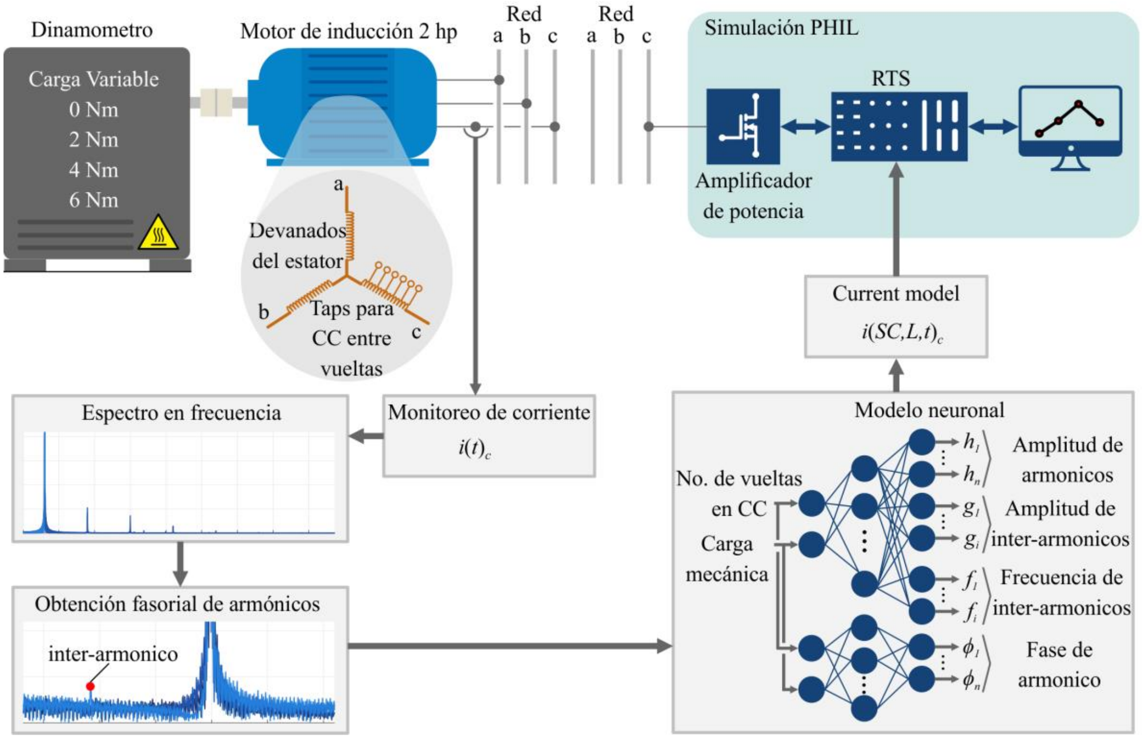

Fig. 26. Implementación de modelo experimental de motor de inducción con falla de cortocircuito.

carga nominal, 66% de carga nominal y plena carga) así como las diferentes condiciones de corto circuito (0, 5, 10, 15, 20, 25, 30), como se observa en las Fig. 27(a), (c), (e) y (g) la mayoría de las señales tienen un ajuste adecuado a la señal, así como las componentes armónicas e inter-armónicas mostradas en la Fig. 27 (b), (d), (f) y (h), en donde como se observa en los zooms hechos a cada armónico la componente inter-armónica debida a la falla también puede ser generada mediante la simulación PHIL; sin embargo, el modelo propuesto no toma en cuenta el voltaje de alimentación lo que da algunos inconvenientes como se observó en las prueba de señales sintéticas. En la tabla V se muestran los errores obtenidos para cada uno de los armónicos los cuales son bajos para las componentes fundamentales a excepción de la condición de 15 vueltas en cortocircuito la cual es una condición que no se usó para el proceso de modelado, sin embargo con la finalidad de observar si el modelo neuronal era capaz de interpolar entre condiciones de cortocircuito se incluyó en los resultados finales obteniendo errores por debajo del

23% para la componente fundamental, en este caso los errores en las componentes

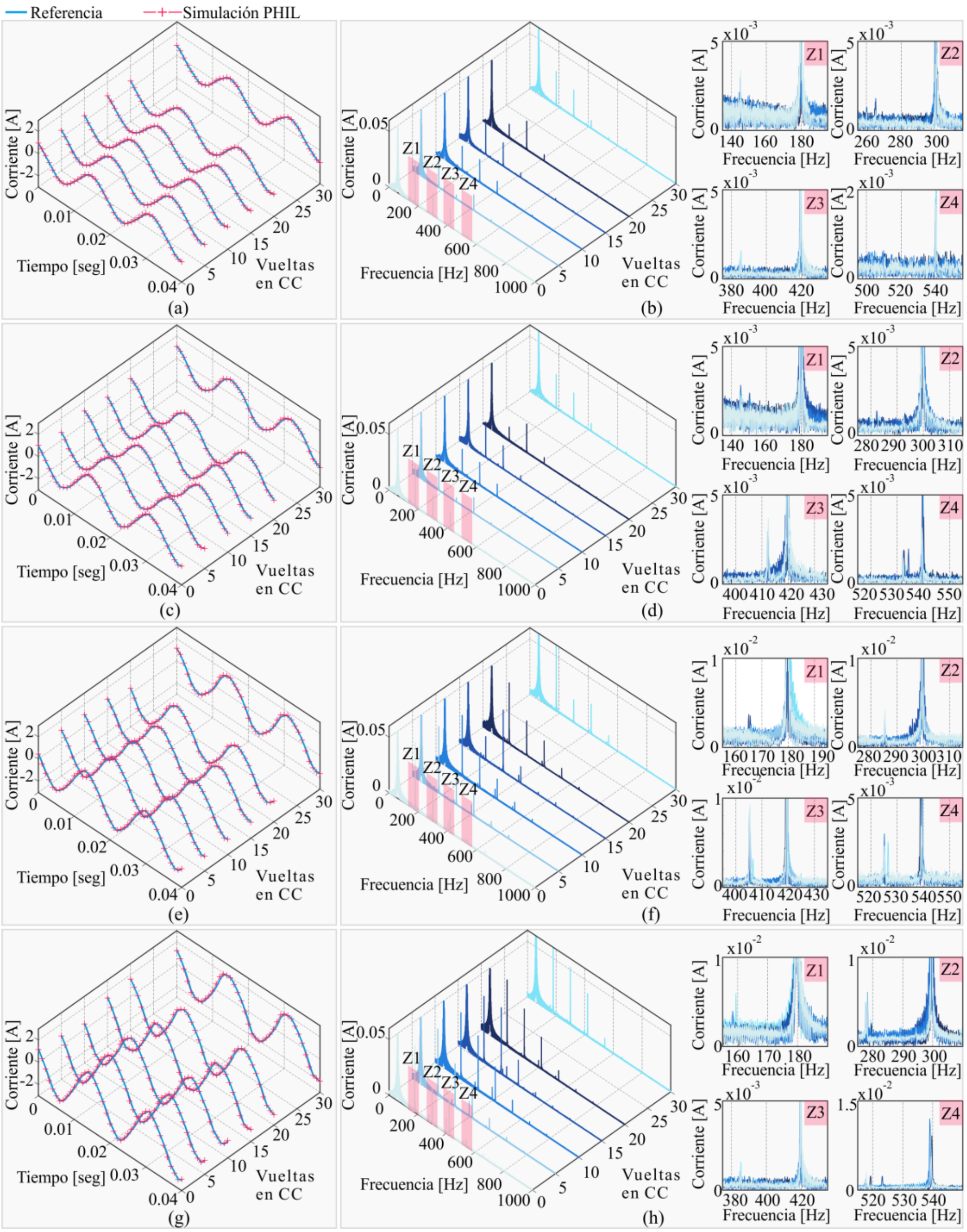

Fig. 27. Simulación cargas de modelos experimentales, sin carga: (a) Señales de corriente, (b) espectro en frecuencia, 33% de carga: (c) Señales de corriente, (d) espectro en frecuencia, 66% de carga: (e) Señales de corriente, (f) Espectro en frecuencia, plena carga: (g) Señales de corriente, (h) Espectro en frecuencia.

armónicas presentan en general buenos resultados a excepción del caso antes mencionado con lo cual se valida el sistema y la simulación PHIL con una novedosa aplicación en la emulación de comportamientos eléctricos asociados a una condición de falla.

Tabla V. Error porcentual de amplitud por armónico para modelos experimentales.

Frecuencia [Hz]	**60**				**180**				**300**				**420**				**540**			
Carga mecánica [%]	**0**	**33.3**	**66.7**	**100**	**0**	**33.3**	**66.7**	**100**	**0**	**33.3**	**66.7**	**100**	**0**	**33.3**	**66.7**	**100**	**0**	**33.3**	**66.7**	**100**
0 vueltas CC, error [%]	0.8	0	0.86	1.3	0.19	0.8	11.8	3.9	5.89	2.92	6.36	7.92	15.5	1.81	3.05	4	4.34	3.76	18.1	18
5 vueltas CC, error [%]	0.1	0	0.18	1.19	4.33	0.03	24	8.09	2.79	2.13	5.66	3.93	4.83	3.69	0.39	14.9	2.7	29.9	2.45	56.3
10 vueltas CC, error [%]	1.5	1.75	0.57	0.55	2.55	17.2	0.08	1.25	15.6	1.91	1.11	1.71	30.8	11.5	5.36	0.72	9.79	42.7	3.4	19.2
15 vueltas CC, error [%]	16.5	23.5	23	8.26	34.8	76.4	54.3	18.6	41.8	27	56.6	28.9	95	57.6	80.7	85.6	93.8	94.5	89.7	57.3
20 vueltas CC, error [%]	0.9	0.19	2.69	1.65	1.74	1.49	16.2	11	2.31	5.89	0.04	0.64	3.2	3.42	3.55	3.27	34	8.3	22.3	37.9
30 vueltas CC, error [%]	1.9	0.78	0.29	0.77	6.77	0.05	0.4	1.38	3.45	0.41	2.03	0.75	11.8	0.97	4.19	4.17	15.3	11.8	3.08	4.6

Finalmente debido a la importancia de las fallas de cortocircuito en máquinas eléctricas no solo rotativas sino también en transformadores se analizó el modelado de un caso particular de gran relevancia en la comunidad científica, el cual es el caso de corriente de magnetización de un transformador, la cual ocurre cuando este es conectado a la red, en este caso es posible producir grandes corrientes que activen las protecciones diferenciales de cortocircuito sin que en realidad exista esta condición, adicionalmente, una condición de cortocircuito en los devanados puede producir diferentes condiciones armónicas, en las cuales se basan las protecciones diferenciales, esto puede afectar el correcto funcionamiento de las protecciones a su vez que el transformador cuente con una falla que pueda evolucionar de manera rápida convirtiéndose en una condición de corto circuito a tierra por ejemplo. En este caso se propone un modelo genérico en base a la corriente de magnetización y diferentes condiciones de cortocircuito basado en series de Fourier y funciones gaussianas debido a las características especiales que se generan en la magnetización de un transformador, en la Fig. 28 se muestra el proceso propuesto

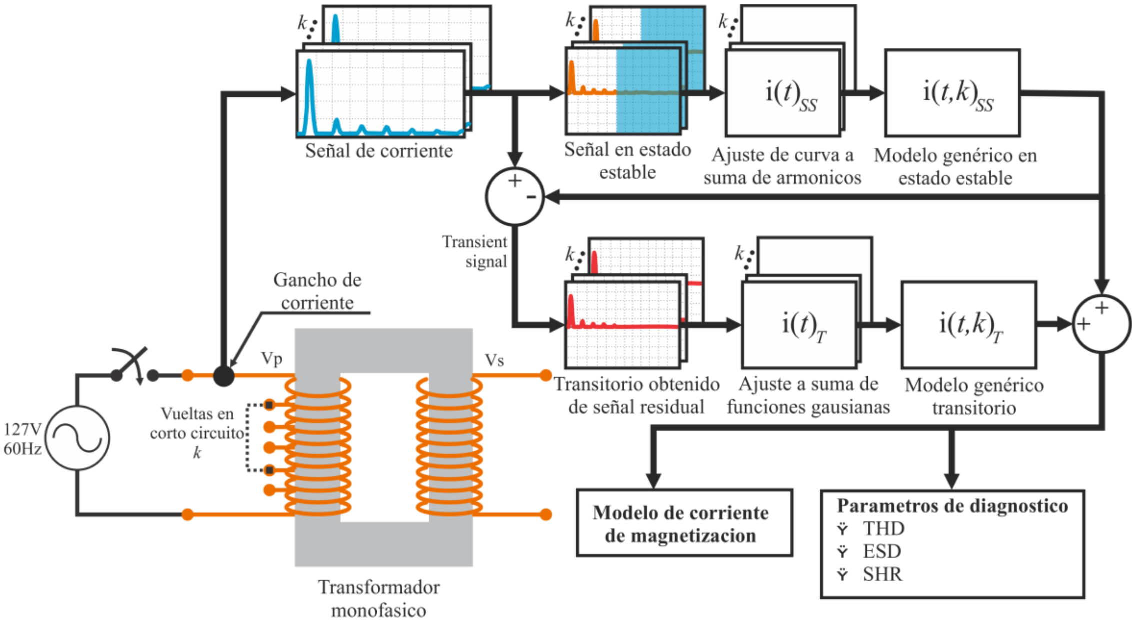

Fig. 28. Implementación de modelo experimental de transformador monofásico con falla de cortocircuito.

para el modelado a partir de señales experimentales. Por consiguiente, se realiza la implementación del modelo propuesto en el simulador PHIL en el cual, aunque buenos resultados son obtenidos en el modelo propuesto, se observan que en la simulación se tienen bajos niveles de ajuste, en particular se emulan dos condiciones de cortocircuito de 0 vueltas y 20 vueltas cortocircuitadas; en la Fig. 29(a) se observa el ajuste a la condición de 0 vueltas en cortocircuito sin embargo se obtiene un ajuste muy bajo lo cual se debe problemas de sintonización de control, sin embargo la condición de 20 vueltas en corto circuito presenta un ajuste del 70% como se observa en la figura 29(b), el cual puede ser mejorado a partir de mejoras en la sintonización de control del PHIL o la propuesta de nuevos algoritmos de interfaz, mejorando la herramienta de simulación PHIL con una potencial aplicación en pruebas de dispositivos de protección o metodologías para la detección de fallas de cortocircuito

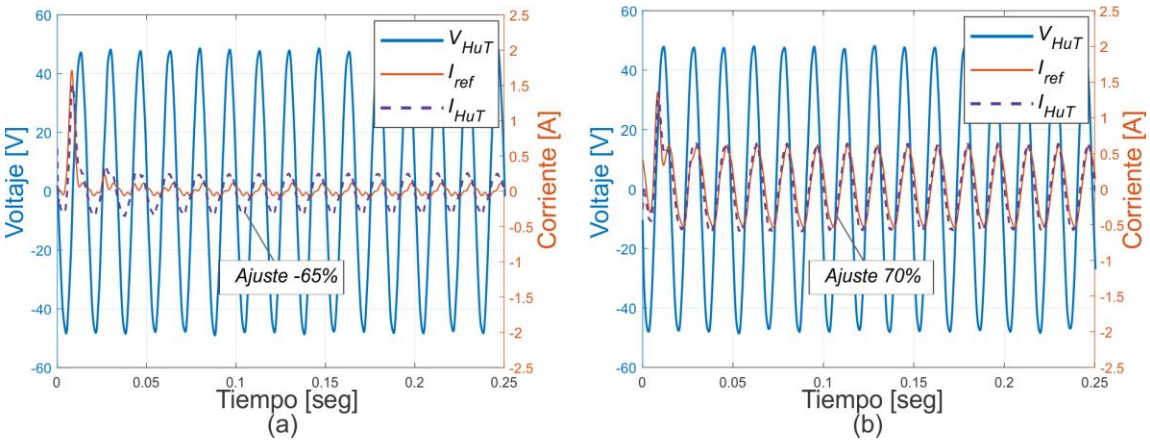

Fig. 29. Simulación PHIL corriente de magnetización: (a) 0 vueltas en cortocircuito, (b) 20 vueltas en cortocircuito.

CAPITULO V

Conclusiones

5. CONCLUSIONES

Por medio de este trabajo de investigación se obtuvo la integración de un sistema PHIL de corriente el cual está enfocado en poder emular el comportamiento eléctrico de una determinada carga virtual. Aunque el principal enfoque de este trabajo está orientado a la propuesta de un sistema para emular máquinas eléctricas rotativas con una novedosa aplicación que incluye el comportamiento bajo condiciones de falla, se realizaron validaciones mediante diferentes cargas que incluyen cargas resistivas, RL, no lineales por medio de un motor de CD y un transformador con diferentes condiciones de falla, donde se observa una amplia gama de aplicaciones dentro del área de eléctrica, ya sea como herramienta de validación de instrumentos o metodologías de análisis, pruebas de diferentes fuentes de alimentación o HuT, compensadores de potencia entre otras.

Dentro de los casos de estudio analizados se propone el uso de modelos a partir del comportamiento teórico de diferentes cargas los cuales se alimentan de manera virtual mediante el monitoreo de voltaje en el punto de conexión entre el sistema de simulación PHIL y el HuT, lo cual presenta una condición más real en cuanto a la corriente virtual que se debe obtener, dando un control no solo de amplitud sino de la fase real que debe obtener la carga respecto al voltaje. Por lo contrario, en los modelos experimentales propuestos se propone la sincronización de la señal mediante un PLL ya que los modelos propuestos no incluyen la relación de fase entre el voltaje y la corriente, lo que es de utilidad para simplificar los modelos propuestos cuyo objetivo principal es generar las firmas eléctricas de acuerdo a una condición de operación. En este caso se analizó una de las condiciones con gran porcentaje de recurrencia en motores de inducción, la cual se basa en condiciones de cortocircuito entre vueltas de los devanados del estator, tomando en cuenta diferentes condiciones de carga mecánica lo cual da a la simulación PHIL un acercamiento a condiciones presentes en ambientes industriales. Asimismo, dado a la importancia de la condición de falla de cortocircuito en devanado no solo en motores eléctricos sino también en transformadores, se propone un modelo basado en diversas condiciones de cortocircuito junto con la corriente de magnetización, en donde, aunque el simulador PHIL es capaz de reproducir condiciones de vueltas cortocircuitadas en condiciones de bajo número de vueltas se cuenta con poco ajuste el cual se puede mejorar por medio de lo descrito en el párrafo anterior.

Finalmente, el desarrollo de este proyecto representa un precedente para el inicio de una línea de investigación dentro de la universidad orientada a simulaciones PHIL las cuales son requeridas tanto en la industria para el desarrollo o pruebas de diferentes prototipos orientados al área eléctrica, como en las universidades como herramienta didáctica o de investigación; la cual con el incremento de las nuevas tecnologías en las redes eléctricas, tanto de generación, protección y distribución, representa una invaluable herramienta debido a las ventajas que conlleva tener un sistema de simulación PHIL, como bajo costo en puestas experimentales, repetitividad en pruebas, bajo riesgo, etc. Como trabajo a futuro existen diferentes contribuciones tanto científicas como tecnologías que pueden ser aplicadas como el desarrollo y la innovación en nuevas formas de control o mejoras que ayuden a la precisión y estabilidad del sistema, o en las aplicaciones que se le puede dar al sistema.

6. REFERENCIAS

Amitkumar K. S, Kaarthik R. S. and Pillay P., 2018. A versatile power hardware-in-the-loop based emulator for rapid testing of transportation electric drives. IEEE transactions on transportation electrification. vol. 4. no. 4.

Benigni A., Helmedag A., Abdalrahman A. M. E., Pilatowicz G. and Monti A., 2011, FlePS: a power interface for power hardware in the loop. Proceedings of the 2011 14th European conference on power electronics applications. Birmingham, United Kingdom.

Bevis R., Edrington C. S. and Leonard J., 2010. Application of power hardware-in-the-loop for electric vehicles: a case study utilizing switched reluctance machines. 36th annual conference on IEEE industrial electronics society. Glendale, AZ, USA.

Damborg, M., El-Sharkawi, M., Aggoune, M. and Marks, R. I., 1990. Potential of artificial neural networks in power system operation. Circuits and Systems. IEEE International Symposium on, pp. 2933-2937.

De Souza I. D. N., de Almeida P. M. and Barbosa P. G., 2017. Sliding mode control of a grid-emulator converter applied to a PHIL. Brazilian power electronics conference. Juiz de Fora, Brazil.

Fathy H. K, Filipi Z. S., Hagena J. and Jeffrey Stein, 2006. Review of hardware-in-the-loop simulation and its prospects in the automotive area. Modeling and simulation for military applications.

Fox J. and Gislason B., 2014. Introduction to the Clemson University 15 MW Hardware-In-the-Loop Grid Simulator. Power Systems Conference (PSC). Clemson University.

Haitham, A.-R., Atif, I. & Guzinski, J., 2012. High Performance Control of AC Drives with Matlab / Simulink Models. s.l.:John Wiley & Sons.

Heerdt J., Ferreira Coutinho D., Mussa S. and Lobo Heldwein M., 2014. Control Strategy for Current Harmonic Programmed AC Active Electronic Power Loads. Industrial Electronics, IEEE Transactions on, vol. 61. No. 8. pp. 3810-3822.

Hogan D. et al., 2014. A rapid prototyping tool for load and source emulation in a microgrid test laboratory. Applied Power Electronics Conference and Exposition (APEC), 2014 Twenty-Ninth Annual IEEE, pp. 2245-2252.

Honglin Z., Tian W. X. and Tongzhen D., 2017. A novel time expansion method to cope with simulator delay in the hardware-in-the-loop study of hysteresis current control. 20th International conference on electrical machines and systems. Sydney, NSW, Australia.

Jeon J. H., Kim J. Y., Kim H. M., Kim S. K., Cho C., Kim J. M., Ahn J. B. and Nam K. Y., 2010. Development of hardware-in-the-loop simulation system for testing operation and control functions of microgrid. IEEE transactions on power electronics. vol. 25. No. 12.

Jung J. H. and Ahmed S., 2012. Real-time simulation model development of single crystalline photovoltaic panels using fast computation methods. Solar Energy. Vol. 86, no. 6.

Kesler M., Ozdemir E., Kisacikoglu M. and Tolbert L., 2014. Power Converter-Based Three-Phase Nonlinear Load Emulator for a Hardware Testbed System. Power Electronics, IEEE Transactions on , 29(11), pp. 5806-5812.

Kolb J. and Kammerer F., 2014. The Modula Multinivel Converter as Universal High-Precision 3AC Voltage Source for Power Hardware-in-the-Loop Systems. PCIM Europe 2014.

Kotsampopoulos P. C., Kleftakis V. A. and Hatziargyriou N. D. Laboratory education of modern power systems using PHIL simulation. IEEE transactions on power systems, vol. 32. No. 5. Pp. 3992-4001.

Li. H., Steurer M., Shi K. L., Woodruff S. and Zhang D., 2006. Development of a unified design, test, and research platform for wind energy systems based on hardware-in-the-loop real-time simulation. IEEE transactions on industrial electronics. vol. 53. no. 4.

Liu, K. et al., 1996. Comparison of very short-term load forecasting techniques. Power Systems, IEEE Transactions on, vol. 11. No. 2, pp. 877-882.

Mahdi D., 2015. Stability analysis and implementation of power-hardware-in-the-loop for power system testing, Queensland University of Technology. Queensland, Australia.

Markou A., Kleftakis V., Kotsampopoulos and N. Hatziargyriou, 2017. Improving existing methos for stable and more accurate power hardware-in-the-loop experiments. IEEE 26th international symposium on industrial electronics. Edinburgh, United Kingdom.

Mohan N., Underland T. M. and Robbins W. P., 2009. Electronica de potencia convertidores, aplicaciones y diseño. Mc Graw Hill.

Morales-Perez C., Grande-Barreto J., Rangel Magdaleno J. and Peregrina-Barreto H., 2018. Bearing fault detection in induction motors using MCSA and statistical analysis. IEEE instrumentation and measurements technology conference. Houtson, TX, USA.

Rangel-Magdaleno J. J, Peregrina-Barreto H., Ramirez-Cortes J. M., Gomez-Gil P. and Morales-Caporal R. FPGA-based broken bars detection on induction motors under different load using motor current signature analysis and mathematical morphology. IEEE transactions on instrumentation and measurement. vol. 63. no. 5. pp. 1032-1040.

Ren W., 2007. Accuracy evaluation of power hardware-in-the-loop (PHIL) simulation, Electronic theses. Florida state university.

Ren W., Steurer M. and Bladwin T. L 2008. Improve the stability and the accuracy of power hardware-in-the-loop simulation by selecting appropriate interface algorithms. IEEE transactions on industry and applications. vol. 44. no. 4.

Rivera-Guillen J. R., de Santiago-Perez J. J. and Amezquita-Sanchez J. P., 2018. Enhanced FFT-based method for incipient broken rotor bar detection in induction motors during the startup transient. Measurement. Pp. 277-285.

Schmitt A., Richter J., Gommeringer M. Thomas Wersal and Braun M, 2016. A novel 100kW power hardware-in-the-loop emulation test bench for permanent magnet synchronous machines with nonlinear magnetics. 8th IET international conference on power electronics, machines and drives. Glasgow, United Kingdom.

Singh, A., Ibraheem, I., Muazzam, M. and Chaturvedi, D., 2012. Load Forecasting Techniques and Methodologies: A Review. Power, Control and Embedded Systems (ICPCES), 2012 2nd International Conference on, pp. 1-10.

Steurer M., Edrington C. S., Sloderbeck M., Ren. W. and Langston J., 2010. A megawatt-scale power hardware-in-the-loop simulation setup for motor drives. IEEE transactions on industrial electronics. Vol. 57. No. 4.

Tzou Y. Y. and Jung S. L., 1998. Full control of a PWM DC-AC converter for ACE voltage regulation. IEEE transactions on aerospace and electronic systems. vol. 34. no. 4.

Vodyakho O., Steurer M., Edrington C. S. and Fleming F, 2012. An induction machine emulator for high-power applications utilizing advanced simulation tools with graphical user interfaces. IEEE transactions on energy conversion. vol. 27. no. 1.

Vukosavic, S. N., 2012. Electrical Machines. Springer Science & Business Media.

7. APENDICE A. Productos del trabajo de investigación.

Anexo A

Electric Power Systems Research 152 (2017) 306–315

Contents lists available at ScienceDirect

Electric Power Systems Research

journal homepage: www.elsevier.com/locate/epsr

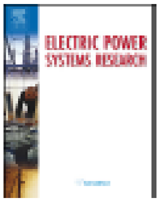

Experimental data-based transient-stationary current model for inter-turn fault diagnostics in a transformer

Arturo Mejia-Barron[a], Martin Valtierra-Rodriguez[a,*], David Granados-Lieberman[b], Juan C. Olivares-Galvan[c], Rafael Escarela-Perez[c]

[a] ENAP-Research Group, Facultad de Ingeniería, Universidad Autónoma de Querétaro (UAQ), Campus San Juan del Río, Río Moctezuma 249, Col. San Cayetano, C. P. 76807 San Juan del Río, Qro., México
[b] ENAP-Research Group, Departamento de Ingeniería Electromecánica, Instituto Tecnológico Superior de Irapuato (ITESI), Carr. Irapuato-Silao km 12.5, Colonia El Copal, C. P. 36821 Irapuato, Gto., México
[c] Departamento de Energía, Universidad Autónoma Metropolitana-Azcapotzalco, Av. San Pablo 180, Col. Reynosa Tamaulipas, C. P. 02200 Ciudad de México, México

ARTICLE INFO

Article history:
Received 5 April 2017
Received in revised form 12 July 2017
Accepted 20 July 2017
Available online 31 July 2017

Keywords:
Inrush current
Inter-turn fault
Transformer
Short-circuited turns
Transformer diagnostics
Transformer winding

ABSTRACT

Inrush current has been well-studied in transformers using different methods to diagnose internal faults. In this paper, a new methodology is proposed using experimental data for obtaining a time-model based on inrush currents. The main contribution of this paper consists of providing a model that accurately reproduces the inrush and steady state currents of single-phase transformers, offering the unique ability to analyze several severity levels of turn to turn faults. The obtained model considers eleven cases of inter-turn fault (2, 3, 4, 5, 10, 15, 20, 25, 30, 35, and 40 short-circuited turns) and allows the study of indices to detect inter-turn faults. The proposed model is based on two functions: a steady-state function based on Fourier series and a residual transient function based on a sum of Gaussian functions. The model allows the study of harmonic content because of its direct time-frequency representation. The model is developed using experimental signals measured from a single-phase transformer, which is validated by means of error criteria that assesses experimental and modeled signals. Its capability to reproduce non-modeled signals with different inter-turn fault cases is also evaluated. The modeling of these signals can be a useful tool for simulation-based applications where a reliable waveform reproduction is needed. On the other hand, indices such as total harmonic distortion, energy spectral density and second harmonic ratio are obtained from the proposed model to study its behavior, depending on the severity of the inter-turn faults. Results demonstrate its usefulness to characterize the level of fault severity.

1. Introduction

Transformers play a key role in the electric system, as they connect generation stations with the points of use and provide proper voltage levels for different applications [1,2]. The growing demand of energy, proliferation of complex loads, inadequate maintenance and environmental issues such as lightning or moisture make transformers prone to failures since they are subjected to mechanical, electrical or thermal stresses which may damage their components, causing severe outage problems [2]. Inter-turn winding faults appear because of the insulation breakdown between contiguous turns of the winding. This breakdown is commonly associated to high levels of current and voltage as result of atmospheric overvoltages, ground faults, and ageing or deterioration of the cellulosic insulation due to chemical influence of the transformer oil [3]. High current levels inside of short-circuited turns are often strong enough to damage the winding. The current amplitude is associated with both fault severity and location, which can be several times higher than the winding rated current [4]. Although, a small inter-turn winding fault presents imperceptible effects on transformers in the initial stages, they can quickly lead to more serious faults such as low impedance, phase-to-ground, low voltage winding to high voltage winding, or phase-to-phase faults [5]. One of the main protection schemes is the differential protection which has been applied successfully on transmission

---

* Corresponding author.
E-mail addresses: arturo.mejia@enap-rg.org (A. Mejia-Barron), martin.valtierra@enap-rg.org (M. Valtierra-Rodriguez), david.granados@enap-rg.org (D. Granados-Lieberman), jolivares@correo.azc.uam.mx (J.C. Olivares-Galvan), r.escarela@ieee.org (R. Escarela-Perez).

http://dx.doi.org/10.1016/j.epsr.2017.07.020
0378-7796/

lines and generators. However, a key problem for fault detection is to distinguish between a fault current and an inrush current due to the energization of transformers [6], which can occur in high- and low-power transformers. In this regard, methodologies that provide fault indices related to fault severity using inrush current are sought to operate the transformer under safer conditions.

Several methods for the analysis of transformer faults have been reported in the literature [6–14] in order to prevent catastrophic conditions, avoid further damages, reduce repair costs and outage times. For instance, the analysis of electromagnetic transients has been carried out to understand and estimate internal faults, where methodologies such as symmetric components analysis [5], harmonic analysis [6], curve fitting methods [7], equivalent instantaneous inductance [8], differential current method [9], Hidden Markov model [10], Park transform [11], frequency response analysis [12,13] and higher-order statistics [14] have been explored. These methods usually use a threshold value in accordance with some reference parameters to detect a fault condition. For example, different numerical values obtained using kurtosis-based indices are used to distinguish an inrush current from an internal fault current [14]. However, the severity of the fault is not quantified. On the other hand, model-based approaches have also been studied to represent the power transformer behavior. For instance, equivalent electric circuit representations in combination with magnetic equivalent circuit and finite element models have been proposed to represent the nonlinearities caused by the magnetizing characteristics of the transformer silicon steel core [15–18]. Also, studies of internal faults have been carried out [19–24] and accompanied by the development of topology-based models. A three-phase transformer model for winding fault studies using the processing of inductances matrix is introduced in Ref. [19]. It allows the simulation of any kind of internal fault such as turn-to-earth or turn-to-turn fault. A permeance-based transformer model is proposed to investigate the behavior of power transformers under permanent or intermittent winding insulation faults [20], where a methodology based on the Park's vector is used for fault detection. Variations of the transfer function of inter-turn faults are studied through an improved lumped circuit model, where the resonance frequency is proposed as a parameter to detect an early inter-turn fault [21]. In addition, lumped circuit parameters, obtained by frequency response interpretation, are analyzed for mechanical failure diagnosis [12]. Also, the frequency response analysis is used for locating inter-turn faults [13]. The inter-turn fault is studied with an autotransformer circuit represented with state-space equations for different types of magnetically coupled circuits, such as transformers and rotating machines [22]. Topology-based methods can provide an accuracy and reliable approximation to investigate inter-turn faults. Although the vast majority of the proposed methods are validated through experimentation, the accuracy of these methodologies depends upon transformer parameter estimation, as different types of transformers with different power ratings, insulation types, cooling systems, etc. are considered. In general, topology-based techniques are excellent design tools which can provide a very accurate response for simulation purposes. However, they have a high complexity during their implementation. Curve-fitting techniques have been carried out to reduce complexity of topology-based models, where nonlinearities are constructed using diverse mathematical functions [8]. These functions adjust their parameters in order to model different types of transformers and different fault conditions. Although, there are several model-based works that study inter-turn faults in transformers using the inrush current phenomenon, issues such as model complexity and the assumptions taken for simulation purposes may compromise their usage as tools for transformer fault diagnostics in real practice. Therefore, the development of methods and models that provide more efficient and reliable results in terms of simplicity and performance for the analysis and diagnostics of inter-turn faults is still an important topic of research, if different severity levels and experimental signals are considered.

In this paper, a new methodology for the obtaining of transient-stationary current time-models using experimental data is proposed. The proposal is applied to inrush current signals with different severe cases of inter-turn fault, where the in-test transformer is a low-power single-phase transformer of 120VA with epoxy resin insulation, operating at 127 V as input and 24 V as output. As a result, a new transient-stationary inrush current model is obtained, which allows the study and development of indices to diagnose inter-turn faults. These indices are an important tool for correct diagnostics of transformers. The proposed model for the transformer inrush current is obtained by means of mathematical functions. Firstly, the inrush current is divided into two parts: steady-state and residual transient. The steady-state signal is modeled using harmonic sinusoidal functions, which is considered as part of the inrush phenomenon of the entire signal. Secondly, the residual transient signal is modeled using a sum of Gaussian functions. Then, the aforementioned models are combined to obtain a transient-stationary time model. The model also considers the inter-turn fault severity which depends on the number of short-circuited turns, where 2, 3, 4, 5, 10, 15, 20, 25, 30, 35, and 40 short-circuited turns are considered in the proposal. In this regard, the proposed model allows constructing inrush current waveforms with different inter-turn fault severity levels. The study of transformer energization is important for design purposes and fault analysis. Hence, the proposed model can be used to provide inrush current waveforms with different inter-turn fault severity levels. Finally, the indices of energy spectral density of harmonic components, total harmonic distortion (THD) and rate between the second harmonic and the fundamental component are presented as tools for diagnosing the severity of faults using the information provided by the proposed model. It is worth noting that these indices allow the determination of the fault severity, which is a deciding factor to perform maintenance operations. In addition, they can diagnose inter-turn faults from the first cycle of the inrush current and during the steady-state. The severity level from two short-circuited turns can also be assessed. Results demonstrate the usefulness and effectiveness of both the proposed models and the diagnostic indices.

2. Theoretical background

2.1. Transformer inrush current

Inrush current refers to a transient phenomenon occurred when a transformer is switched-on, where high levels of current, even greater than the nominal current, can be produced for a few cycles. In addition, a partial decay on the current magnitude is experienced depending on the transformer design [11,23]. Simulation of this phenomenon represents an important and complex issue due to the nonlinear behavior of the transformer core. As a matter of fact, the transformer should be modeled with a great detail in order to correctly reproduce the behavior associated to the core saturation [15–18]. Analytical formulas of inrush peak and rate of decay can be derived from single phase transformer theory [24], but they are not valid for the entire waveform. In general, it is fair to say that theoretical models offer satisfactory results when compared to the behavior of actual transformers. However, their accuracy depends on truthfulness of the chosen design parameters which are usually subjected to assumptions and simplifications.

2.2. Steady-state model based on harmonic components

Harmonic models have been proposed for power transformers to understand the influence of harmonic content on other compo-

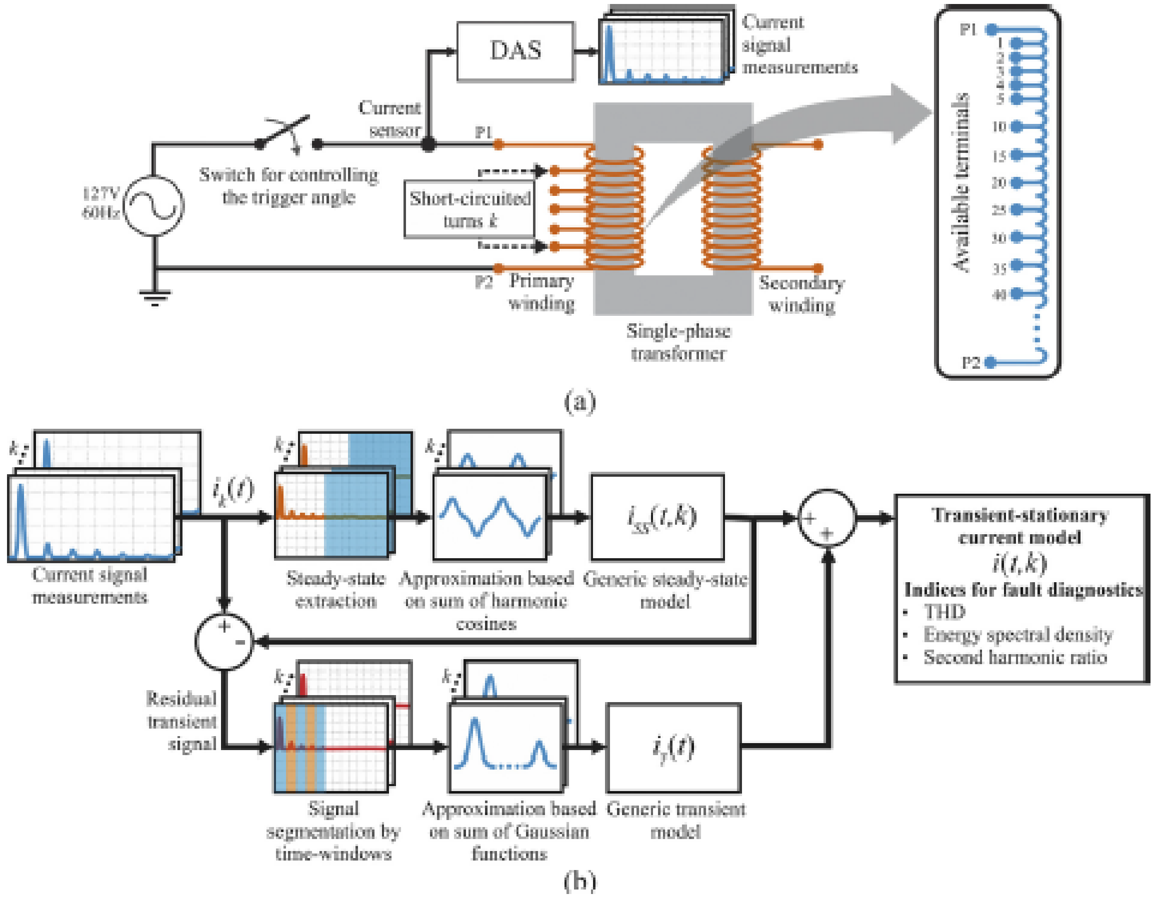

Fig. 1. Proposed methodology: (a) flowchart for acquisition of inrush currents and (b) methodology for obtaining the proposed model.

nents of the grid [25]. Fourier series is a mathematical tool that allows modeling an arbitrary periodic signal by means of an infinite series of harmonic components [26]. Each of these components is composed of a sine wave and a cosine wave of equal integer frequency is given by:

$$\lambda(t)=\frac{1}{2}a_0+\sum_{n=1}^{\infty}A_n\cos\left(n\omega_f t\right)+\sum_{n=1}^{\infty}B_n\sin\left(n\omega_f t\right)\tag{1}$$

where the last two terms can be combined into a single term for each harmonic component, i.e., a cosine with an amplitude c_n and a phase angle ϕ_n. Therefore, the above equation can be expressed as:

$$\lambda(t)=c_0+\sum_{n=1}^{\infty}c_n\cos\left(n\omega_f t-\phi_n\right)\tag{2}$$

where n represents the harmonic component order, c_0 is defined to be (½) a_0, t is the time and ω_f represents the fundamental angular frequency.

2.3. Transient model based on Gaussian model

Gaussian models have been applied to obtain expressions that describe the magnetic flux density and permeability in power transformers [27]. Given a sequence of uniformly spaced points ($j=1,\ldots,J$), it is possible to approximate a time series using a sum of Gaussians. In this sense, an inrush current can be expressed as a train of Gaussian pulses. In other words, it is the sum of Gaussian functions with different center times, amplitudes, and standard deviations as follows:

$$\xi(t)=\sum_{j}^{J}d_je^{-\left(\frac{t-t_j}{2\sigma_j}\right)^2}\tag{3}$$

where d_j denotes the amplitude, t_j represents the center time, σ_j is the shape parameter, and J is the number or order of the sum of the Gaussian functions. J depends on the transient state duration, i.e., the number of lobes that the transient state has.

3. Proposed transient-stationary current model

3.1. Transient-stationary current time-model with inter-turn fault

The proposed methodology to obtain a transient-stationary current time-model is shown in Fig. 1. Inrush current measurements, $i_k(t)$, under different fault conditions (5, 10, 15, 20, 25, 30, 35 and 40 short-circuited turns) and healthy state, are considered in the proposal, where k represents the number of short-circuited turns. The inrush current signals are generated by switching on the voltage source as shown in Fig. 1(a), where the trigger angle is controlled to get a voltagez ero-crossing. Then, the data acquisition system (DAS) along with a current sensor perform the current signal measurements. To obtain the inrush current time-model, the flowchart of Fig. 1(b) is proposed. Firstly, the steady-state model of each current signal is extracted in a limited period of time. Secondly, a curve-fitting model based on a sum of harmonic cosine waves is carried out for each signal using Eq. (2), where nine harmonics are considered for the cosine function. A straight-line function is proposed

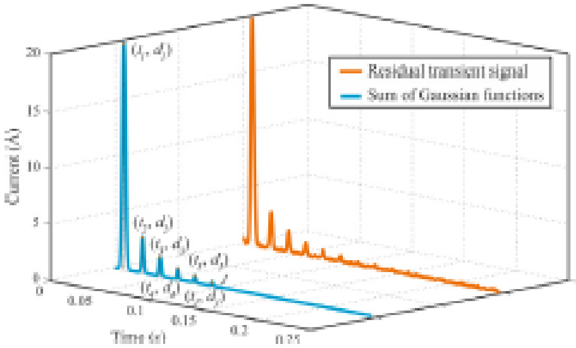

Fig. 2. Approximation based on sum of Gaussian functions.

to represent the amplitude behavior, depending on the inter-turn fault condition, as follows:

$$i_{SS}(t,k) = c_0(k) + \sum_{n=1}^{9} c_n(k)\cos\left(n\omega_f t - \phi_n\right) \tag{4}$$

where $c_0(k) = c_0 + kc'_0$ and $c_n(k) = c_n + kc'_n$ represent a linear behavior in the amplitude parameters of the steady-state model that change in function of the number of short-circuited turns, k. This behavior is experimentally obtained. The fundamental angular frequency parameter, ω_f, is set to $2\pi 60$ rad/s.

Subsequently, the obtained steady-state model is used to construct a residual transient current signal through the difference between the original inrush current signals and the steady state model which is evaluated using its respective fault condition. In a similar way, the residual transient signals are fitted to a sum of Gaussian functions given by Eq. (3), where a segmentation of the signal using time windows is proposed to approximate each lobe of the transient state. It results in a single waveform function of the transient model, $i_T(t)$; in this regard, a constant behavior between inter-turn faults is assumed and validated for the transient model. Fig. 2 shows a residual transient signal and its relationship with a sum of Gaussian functions. Finally, the complete transient-stationary model in time domain is represented as the sum of the previously estimated time models, $(t, k) = i_{SS}(t,k) + i_T(t)$, as follows:

$$i(t,k) = c_0(k) + \sum_{n=1}^{9} c_n(k)\cos\left(n\omega_f t - \phi_n\right) + \sum_{j}^{J} d_j e^{-\left(\frac{t-t_j}{2\sigma_j}\right)^2} \tag{5}$$

In total, six Gaussian functions are used, as six periods in the residual transient signal are considered. Additionally, frequency domain indices such as *THD*, energy spectral density of harmonic components and the second harmonic ratio with the fundamental frequency are estimated from the proposed model to evaluate the fault condition and provide information about the fault severity.

3.2. Frequency domain model and fault diagnostic indices

Fault diagnosis indices are evaluated directly from the proposed model in the frequency domain through the amplitude and phase of the harmonic frequencies. The harmonic amplitude is directly extracted by the cosine amplitude using $c_n(k)$ in Eq. (5). The Gaussian function must be transformed into its frequency domain expression, where the whole expression of the model in frequency domain is given by:

$$i_j(k,\omega) = c_0(k)\delta(\omega) + \sum_{n=1}^{9} c_n(k)\delta\left(n\omega_f - \omega\right)e^{i\phi_n} + d_j/\left(\sqrt{2/\sigma_j^2}\right)e^{jt_j\omega\,[illegible]} \tag{6}$$

where $c_0(k)$, $c_n(k)$, ϕ_n, d_j, t_j, and σ_j represent the steady-state and residual transient model parameters presented in Eq. (5), δ represents the Dirac delta functions as a result of the steady-state model, and ω is the frequency in which the function is evaluated. It is worth noticing that j represents a time window that encloses each of the Gaussian functions. In total, six Gaussian functions are considered since six periods are only considered in the residual transient signal. Therefore, for $j > 6$, the amplitude values of the Gaussian functions are equal to zero while the nine harmonics for the steady-state part of the model persist during all periods of the signal. Thus, a time-frequency function is obtained by the proposed transformation. In this regard, the function can be evaluated at the desired harmonic frequencies, obtaining their corresponding amplitudes. Therefore, the frequency domain-based fault diagnostic indices can be analyzed from Eq. (6).

The *THD* is given by:

$$THD = \frac{\sqrt{\sum_{n=2}^{N} h_n^2}}{h_1} \tag{7}$$

where N is the number of harmonic components, h_n represents the *nth* harmonic amplitude and h_1 denotes the fundamental frequency. The energy spectral density, *S*, for the harmonic content is computed by:

$$S = \sum_{n=1}^{N} h_n^2 \tag{8}$$

Likewise, the ratio between harmonics and the fundamental frequency is evaluated. In particular, the ratio between the second harmonic and the fundamental frequency, which has been studied in previous works for fault detection [12], is considered. Therefore, the second harmonic ratio, *SHR*, can be computed as:

$$SHR = \frac{h_2}{h_1} \tag{9}$$

4. Experimental setup

The overall experimental setup used in this work is shown in Fig. 3(a). The inrush current signal is generated by a low-power single-phase transformer of 120VA with epoxy resin insulation, operating at 127 V as input and 24 V as output. The primary and secondary windings have 474 and 91 turns, respectively. Although the construction and materials of the transformer analyzed differ from power transformers, the inrush current signal waveform is similar, meaning that the proposed methodology can also be applied to larger transformers. Additionally, twelve terminals at the primary winding can be accessed, this is for k = 2, 3, 4, 5, 10, 15, 20, 25, 30, 35, and 40 turns from the third layer of winding. These terminals are short-circuited to produce different inter-turn fault severity levels. Although there are different insulating mediums, such as oil-immersed, dry type, SF_6 Gas, and resin type [1], and the sources and mechanisms of fault, e.g., sources of overheating, mechanisms of lightning and switching [4], can be different, similar effects on the inrush current signal are generated. The transformer is switched-on using a microcontroller-based system model FRDM-K64, which drives a solid-state relay by means of a zero-crossing detector that controls the trigger angle. In this work, a trigger angle of 0° is used for all tests. The trigger control is powered by the primary voltage source. The DAS is implemented using an oscilloscope Tektronix TDS 2024 with a sampling frequency of 5 kHz. The current sensor is a Tektronix A622 with a range from 50 mA to 100 A. The measurements for different fault conditions and healthy state have a duration of 0.25 s, which is large enough to acquire transient and steady states. The acquired current signals are shown in Fig. 3(b), where the evolution of both the transient state and steady-state parts with different fault severity conditions can be observed in the marked zones by Z1 and Z2. It can be observed that there are notable different behaviors depending upon the fault severity. In Z1, the amplitude variation is not too large but Z2 shows a linear

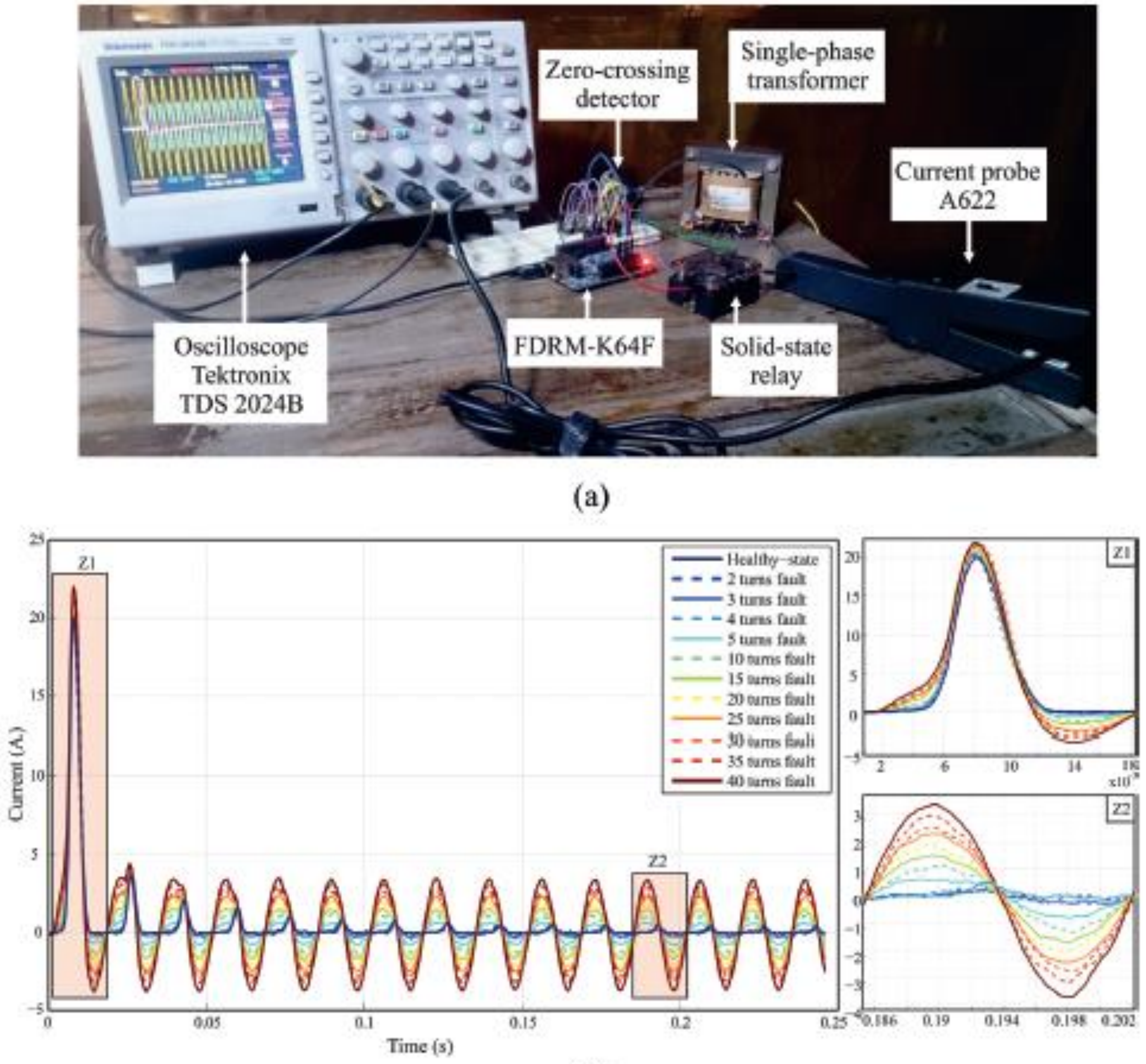

(a)

(b)

Fig. 3. (a) Experimental setup and (b) Current measurements under different inter-turn fault conditions.

increment in the amplitude accompanied with an evident change in the current waveform.

5. Simulation and results

5.1. Experimental inrush model

The transient-stationary time-model is obtained with the test conditions of $k = 5, 10, 15, 20, 25, 30, 35$ and 40 short-circuited turns and healthy state as shown in Fig. 4(a). The remaining tests 2, 3 and 4 short-circuited turns are used later in the model validation. As mentioned in the previous sections, the model consists of two parts: the steady-state and residual transient; where a linearization of each selected condition is proposed to obtain a transient-stationary model depending on the fault severity, k. The obtained model is validated by error criteria such as mean absolute error (*MAE*), root-mean-square error (*RMSE*), and by evaluating the goodness of fit (*FIT*) between the experimental signal and the signal obtained for the proposed model. The overall analysis is performed using MATLAB software.

The steady-state is extracted from the experimental signals as shown in Fig. 4(b), where a linear behavior in the increment of amplitude can be observed. The steady-state is considered from 1.33 s to 2.5 s. In this case, nine harmonic components are considered for each inrush current signal since it is observed that higher components of harmonics do not show an improvement on the curve fitting. Then, a three-dimensional curve fitting is proposed to express Eq. (4). A least square method is employed to obtain a complete time expression as shown in Fig. 4(c). The numerical values for the steady state model are shown in Table 1. Subsequently, the residual transient model is determined using the signal resulting from the difference between the initial inrush current and steady-state signals generated through the steady-state model for the entire time of the experimental signal as shown in Fig. 4(d), where a similar behavior can be noticed among fault conditions. Then, the approximation is carried out by means of the curve fitting of Gaussian functions for each lobe, where an average residual transient current is obtained first from the residual signals with different inter-turn fault conditions. In this case, a sixth-order sum of Gaussian functions is proposed as shown in Fig. 4(e). It is worth noticing that higher variations of current are again presented in steady-state as shown in Fig. 4(b). Table 1 shows the numerical values for the proposed model. The overall responses are shown in Fig. 4(f).

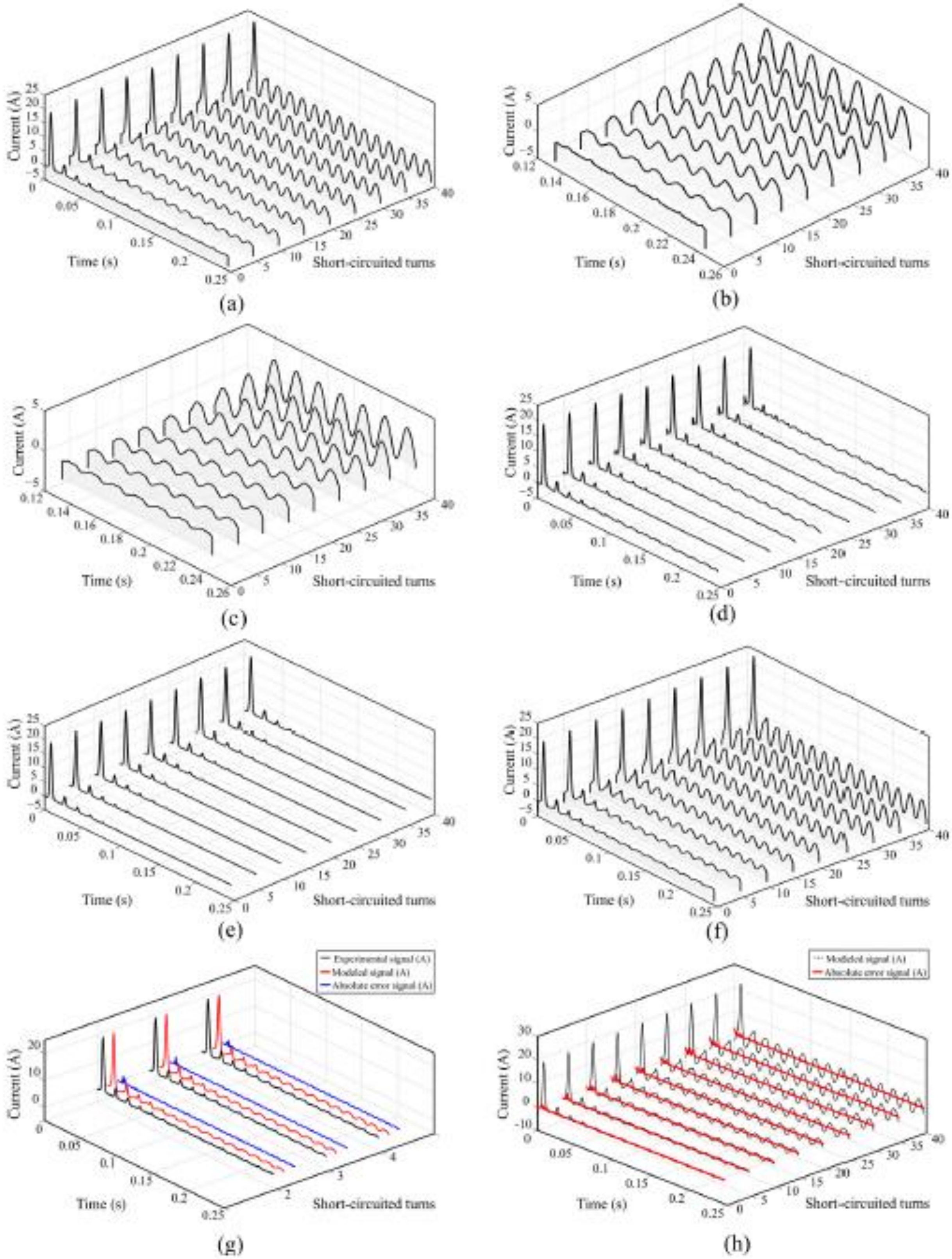

Fig. 4. (a) Experimental inrush current signals, (b) steady-state signals, (c) steady-state model responses, (d) residual transient signals, (e) residual transient model responses, (f) generic model responses, (g) model validation with not modeled signals, and (h) error signals.

5.1.1. Model validation

To assess the robustness of the proposed model absolute error signals and error criteria are computed. Fig. 4(g) shows the results for 2, 3, and 4 short-circuited turns. These signals are not considered during the modeling stage. In Fig. 4(g), the signals in black color are the experimental signals. The signals in red color are signals obtained using the proposed model. The signals in blue color represent the absolute error values between experimental and simulated

Table 1
Numerical values for the proposed model.

Steady-state parameters

Parameter	Value (A)	Parameter	Value (A)	Parameter	Value (rad)
c_0	–0.002115	c'_0	–0.001745		
c_1	–0.246000	c'_1	–0.082670	ϕ_1	–2.449300
c_2	0.079720	c'_2	0.000009	ϕ_2	–1.392500
c_3	0.040800	c'_3	–0.000596	ϕ_3	–1.392500
c_4	0.068200	c'_4	–0.000616	ϕ_4	–2.393200
c_5	0.010010	c'_5	0.000223	ϕ_5	–0.022800
c_6	–0.010130	c'_6	0.000105	ϕ_6	–0.343800
c_7	–0.000254	c'_7	–0.000804	ϕ_7	–1.642600
c_8	–0.007495	c'_8	0.000178	ϕ_8	–1.287500
c_9	0.002944	c'_9	–0.000214	ϕ_9	–1.528500

Residual transient parameters

Parameter	Value (A)	Parameter	Value (s)	Parameter	Value
d_1	20.130000	t_1	0.008302	σ_1	0.002067
d_2	3.209000	t_2	0.026330	σ_2	0.001645
d_3	1.694000	t_3	0.043090	σ_3	0.001471
d_4	1.003000	t_4	0.059840	σ_4	0.001338
d_5	0.596200	t_5	0.076540	σ_5	0.001258
d_6	0.360500	t_6	0.093180	σ_6	0.001159

signals. As can be observed, small differences are obtained, indicating that the proposed model has a high capability to simulate inrush current signals with interpolated numbers of short-circuited turns. In a similar way, Fig. 4(h) shows simulated signals for 5, 10, 15, 20, 25, 30, 35, and 40 short-circuited turns. It also depicts in red color the absolute error values obtained between the real inrush current signals with inter-turn faults and the simulated signals using the proposed model. These values have an average absolute error of 0.1972A. In order to compare the closeness of the model with experimental tests, the percentage root mean square error, %RMSE, and the percentage mean absolute error, %MAE, are evaluated using the following relations:

$$\%RMSE = \sqrt{\frac{\sum_{m=1}^{M}\left(\hat{i}_m - i_m\right)^2}{N}} \cdot \frac{100}{\max\left(\hat{i}\right) - \min\left(\hat{i}\right)} \tag{10}$$

$$\%MAE = \frac{1}{M}\sum_{m=1}^{M}\left|\hat{i}_m - i_m\right| \cdot \frac{100}{\max\left(\hat{i}\right) - \min\left(\hat{i}\right)} \tag{11}$$

where $\hat{i}_m$ represents the samples of the experimental signals, i_m denotes the samples obtained by the proposed model, and M indicates the signal length. Additionally, the goodness of fit is evaluated by means of:

$$\%FIT = 1 - \frac{\|\hat{i}_m - i_m\|}{\|\hat{i}_m - mean\left(\hat{i}_m\right)\|} \tag{12}$$

The numerical values obtained from Eqs. (10)–(12) are listed in Table 2, where the results for the inter-turn fault signals which are not used to obtain the model are also included. A percentage of *RSME* no greater than 10.737% is obtained. This value corresponds to the signal of healthy condition, which is somehow congruent since the current signal in steady-state contains a different harmonic content, leading to errors in the harmonic-based model. Therefore, a greater error in conditions of lower fault severity is expected due to the linearization process. However, the error is low enough to provide a very good waveform representation for each condition. Regarding *MAE* values, errors no greater than 1.191% are obtained. For the goodness of fit, evaluated as the percentage of *FIT*, values greater than 83.628% are calculated, being 100% a perfect fit. The above criteria indicate that the proposed model provides a reliable modeling for inrush waveforms associated to short-circuited faults, even for non-modeled signals, i.e., 2, 3, and 4 short-circuited turns.

Table 2
Validation parameters.

Number of short-circuited turns	%RMSE	%MAE	%FIT
0 (healthy)	10.737	0.947	87.983
2[a]	8.541	1.145	83.628
3[a]	3.469	1.075	85.846
4[a]	1.984	1.191	85.442
5	0.623	0.351	91.303
10	2.483	0.501	89.758
15	2.777	0.752	88.972
20	0.748	1.144	86.341
25	3.928	0.753	91.173
30	4.074	0.559	89.625
35	5.025	0.937	90.202
40	4.307	1.101	89.507

[a] Test conditions used only for validation purposes.

5.2. *Evaluation of fault diagnostic indices*

The indices to diagnose the fault condition are based on harmonic amplitudes which can be obtained directly from the model in Eq. (6). The model is represented in the frequency domain by considering windows of a period of time large enough to enclose an entire Gaussian function, e.g., in Fig. 3(b), one period is the zone depicted by Z1. The results for *THD*, *S* and *SHR* are shown in Fig. 5. The *THD* indices are obtained using time windows which enclose a cycle of signal as shown in Fig. 5(a). An exponential decay can be observed in the function of the fault severity level. Also, the behavior of *THD* per cycle is depicted in Fig. 5(b), where it can be observed that the *THD* value remains constant throughout the signal duration. The results for *S* are shown in Fig. 5(c). This index presents an exponential increment in function of the inter-turn fault severity. It also remains constant during the signal periods as shown in Fig. 5(d). The second harmonic ratio shown in Fig. 5(e) also presents an exponential decay as the *THD*. In a similar way, the second harmonic ratio remains relatively constant over time as shown in Fig. 5(f). Therefore, it can be noticed that the proposed indices estimated using the transient-stationary model remain constant for almost all the periods, which means that the inrush phenomenon has a negligible effect over the diagnostic indices. Consequently, the used indices provide a reliable way to identify inter-turn fault conditions. Hence, transformer condition and the fault severity can

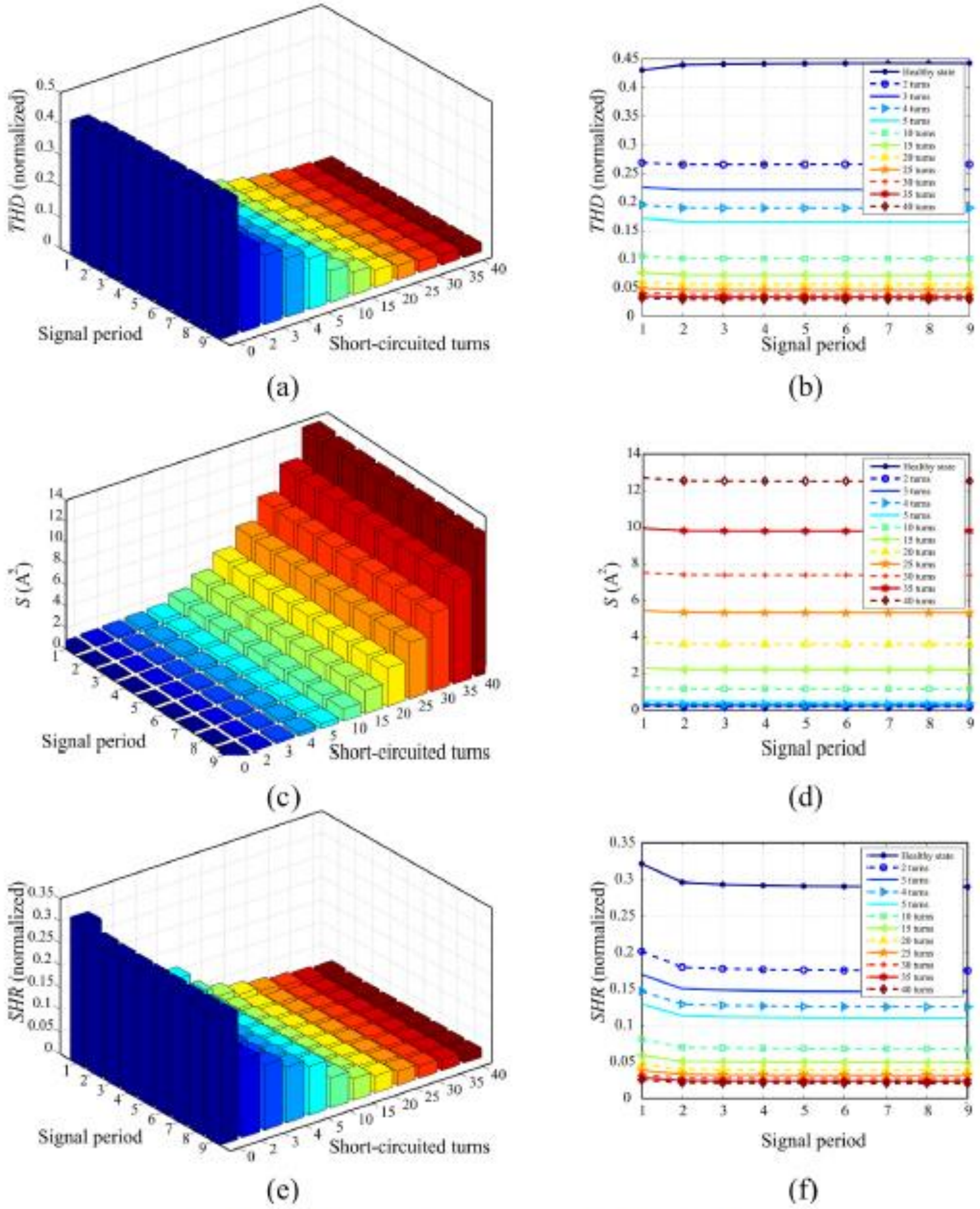

Fig. 5. (a) *THD* index, (b) *THD* per period, (c) *S* index, (d) *S* per period, (e) *SHR* index, and (f) *SHR* per period.

be evaluated during all the cycles of the inrush current using the proposed model.

5.3. Discussion

A comparison with different modeling techniques is shown in Table 3. Models based on harmonic components [25], state space circuit representation [22], transfer functions [21], and state space system based on numerical methods [18], have been reported in literature. However, they do not provide parameters or methodologies for diagnostics of inter-turn faults. Park vector [20] and the negative sequence current [4] approaches have been presented for diagnosing inter-turn faults. In this work, the proposed model in both time domain and frequency domain allows obtaining indices such as *THD*, *S*, and *SHR* for diagnosing inter-turn faults. These indices allow the inter-turn fault detection from the first cycles

Table 3
Comparison of other works and the proposed one for model-based current analysis.

References	Model	States		Model source		Representation of inter-turn faults	Transformer rating power (VA)	Parameters or methodologies proposed for fault identification	Inter-turn fault cases
		T	S	ED	TD				
[25]	Harmonic	–	X	X	–	–	500	–	–
[22]	State space circuit representation	–	X	X	X	Emulated with taps between turns	120	–	30, 40, 60, 88, 108, 118, 148, 196, 226, 236, 256, 266, 296 turns
[21]	Transfer function	–	X	X	X	Simulated by a resistor	–	–	Discrete values od resistor between 200 Ω–0 Ω
[20]	Permeance-based transformer model	–	X	X	X	Emulated with taps between turns	10300	Park vector approach	2 and 4 turns
[18]	State space system based on numerical methods	X	X	X	X	–	300	–	–
[4]	Finite element modeling	X	X	–	X	Simulated by different winding excitations	–	Negative sequence current	Primary winding 2.27%, 4.54%, 6.81%, 9.08%
									Secondary winding 1.92%, 3.84%, 5.76%, 7.69%
Proposal	Transitory-stationary function model	X	X	X	–	Emulated with taps between turns	120	Time-frequency domain parameters: THD, S, SHR	2, 3, 4, 5, 10, 15, 20, 25, 30, 35, 40 turns

T: transitory, S: stationary, ED: experimental data, TD: theoretical data, –: no reported, and X: reported.

of the inrush current signal. Similar to the proposal, the transient state of an inrush current is also considered in Refs. [4,18]. In the latter, experimental data are not considered. Unlike these works, the proposal is based on experimental signals in time domain, which leads to a low complexity for its computation and implementation, only requiring a basic knowledge for its interpretation. These features can be exploited for the development of simple and reliable methodologies for automatic diagnostics of inter-turn faults in transformers. Finally, different levels of severity of inter-turn fault have been considered in previous works [4,20–22], where different power ratings are used. In the proposed work, several cases are also considered, such as: 2, 3, 4, 5, 10, 15, 20, 25, 30, 35, and 40 short-circuited turns.

6. Conclusions

A methodology for modeling transient-stationary current signals using experimental data is proposed. The obtained model considers inter-turn winding fault conditions, where 2, 3, 4, 5, 10, 15, 20, 25, 30, 35, and 40 short-circuited turns are employed to study the transformer performance for different fault levels. The proposed model is based on two curve fitting functions. The proposed model is linearized to obtain a transient-stationary model that considers the number of short-circuited turns as an independent variable. The transient-stationary model is validated using both the error criteria and robustness to interpolate non-modeled inrush current signals. Small differences between experimental and modeled signals are found and quantified: values below 10.737% and 1.191% are obtained for $\%RMSE$ and $\%MAE$, respectively. The goodness of the fit, $\%FIT$, is also obtained with a minimum value of 83.628%. The highest error rates are present for conditions of low fault conditions due to both the level of harmonic content in the steady-state of the current signal and the linearization process to obtain the transient-stationary model. Nevertheless, the waveform representation obtained from the transient-stationary model is quite good even for interpolated cases ($k = 2, 3$, and 4). Moreover, although a low-power transformer is used to obtain the proposed model, the methodology can be applied to power transformers, as they have similar inrush current signal waveforms, i.e., transient and stationary parts; however, the resulting model will have different coefficients, as the model will fit for a specific transformer. On the other hand, the proposed model in frequency domain allows studying inter-turn winding faults by means of the analysis of harmonic components and frequency domain-based indices. Indices such as THD, S, and SHR are analyzed as a function of fault severity, where time-windows of one period are considered. It is worth noting that other indices can be researched from the proposed model. In general, the analyzed indices present a constant behavior over time, giving the opportunity to visualize fault conditions from the first cycles of the inrush current signal, regardless of the inrush phenomenon. This behavior is an important characteristic for protection schemes since it allows the differentiation between inrush current and internal faults even at the first signal cycles of the inrush current event, minimizing the negative impact associated to the fault. In addition, the indices are sensitive to fault severity, i.e., their values change according to the severity level. This information can be used to carry out either maintenance for prolonging the life-of service of power transformers or, in the case of low-power transformers (e.g., epoxy resin transformers), the replacement with a new one. Moreover, although a low-power transformer is used to obtain the proposed model, the methodology can be applied in large power transformers, as their inrush current signal waveforms are similar. Finally, due to the simplicity and reliability of the proposed model, it can be used for different applications in a simulation environment where an inrush current waveform with inter-turn fault influence at different levels of severity is required. These applications can be the design and study of protections, sizing and study of both transformer parts and measurement sensors under fault conditions, among others.

In a future work, dry-type transformers with epoxy resin of high capacity will be studied in order to look for a general model, i.e., a model that allows the diagnostics of inter-turn faults from inrush current regardless the power rating. Also, inrush currents of power transformers with different topologies and features will be studied in order to obtain proper models for each transformer type. Changes in the current waveforms, associated to the differences in the constitution and type of power transformers, could require the use and application of new proposals with the aim of obtaining high fit percentages in the resulting transient-stationary current models.

Acknowledgements

This work was partially supported by CONACYT Scholarship296868 and by PRODEP-UAQ-PTC-331 under Project FIN2017-02.

References

[1] P.S. Georgilakis, Spotlight on Modern Transformer Design, Springer Science & Business Media, 2009.
[2] M. Wang, A.J. Vandermaar, K.D. Srivastava, Review of condition assessment of power transformers in service, IEEE Electr. Insul. Mag. 18 (6) (2002) 12–25.
[3] I. Fofana, J. Sabau, Application of petroleum-based oil in power transformer, Nat. Gas Res. Prog. 23 (2008).
[4] J. Faiz, J. Gharaeei, S. Lotfifard, Detection, location, and estimation of severity of interturn faults in power transformers, 2016 10th International Conference on Compatibility, Power Electronics and Power Engineering (2016) 39–44.
[5] L.M.R. Oliveira, A.J.M. Cardoso, Comparing power transformer turn-to-turn faults protection methods: negative sequence component versus space vector algorithms, IEEE Trans. Ind. Appl. 52 (3) (2017) 2817–2825.
[6] M.E. Hamedani Golshan, M. Saghaian-nejad, A. Saha, H. Samet, A new method for recognizing internal faults from inrush current conditions in digital differential protection of power transformers, Electr. Power Syst. Res. 71 (1) (2004) 61–71.
[7] M. Ahmadi, H. Samet, T. Ghanbari, Discrimination of internal fault from magnetising inrush current in power transformers based on sine-wave least-squares curve fitting method, IET Sci. Meas. Technol. 9 (1) (2015) 73–84.
[8] G. Baoming, A.T. de Almeida, Z. Qionglin, W. Xiangheng, An equivalent instantaneous inductance-based technique for discrimination between inrush current and internal faults in power transformers, IEEE Trans. Power Deliv. 20 (4) (2005) 2473–2482.
[9] R.J. Negreiros Alencar, U. Holanda Bezerra, A.M. Damasceno Ferreira, A method to identify inrush currents in power transformers protection based on the differential current gradient, Electr. Power Syst. Res. 111 (2014) 78–84.
[10] X. Ma, J. Shi, A new method for discrimination between fault and magnetizing inrush current using HMM, Electr. Power Syst. Res. 56 (1) (2000) 43–49.
[11] L.M.R. Oliveira, A.J. Marques Cardoso, S.M.A. Cruz, Power transformers winding fault diagnosis by the on-load exciting current Extended Park's vector approach, Electr. Power Syst. Res. 81 (6) (2011) 1206–1214.
[12] D.A.K. Pham, E. Gockenbach, Analysis of physical transformer circuits for frequency response interpretation and mechanical failure diagnosis, IEEE Trans. Dielectr. Electr. Insul. 23 (3) (2016) 1491–1499.
[13] M. Khanali, A. Hayati-Soloot, H. Kristian Høidalen, S. Jayaram, Study on locating transformer internal faults using sweep frequency response analysis, Electr. Power Syst. Res. 145 (2017) 55–62.
[14] L.L. Zhang, Q.H. Wu, T.Y. Ji, A.Q. Zhang, Identification of inrush current in power transformers based on higher-order statistics, Electr. Power Syst. Res. 146 (2017) 161–169.
[15] S.G. Abdulsalam, W. Xu, V. Dinavahi, Modelling and simulation of three-phase transformers for inrush current studies, IEE Proc.: Gener. Transm. Distrib. 152 (3) (2005) 328–333.
[16] J. Faiz, S. Saffari, Inrush current modeling in a single-phase transformer, IEEE Trans. Magn. 46 (2) (2010) 578–581.
[17] M. Jamali, M. Mirzaie, S. Asghar Gholamian, Calculation and analysis of transformer inrush current based on parameters of transformer and operating conditions, Electron. Electr. Eng. J. 109 (3) (2011) 17–20.
[18] A. Tokič, I. Uglešić, G. Štumberger, Simulations of transformer inrush current by using BDF-based numerical methods, Math. Problems Eng. 2013 (2013) 1–10, Article ID 215647.
[19] P. Bastard, P. Bertrand, M. Meunier, A transformer model for winding fault studies, IEEE Trans. Power Deliv. 9 (2) (1994) 690–699.
[20] L.M.R. Oliveira, A.J.M. Cardoso, A permeance-based transformer model and its application to winding interturn arcing fault studies, IEEE Trans. Power Deliv. 25 (3) (2010) 1589–1598.
[21] X. Lei, J. Li, Y. Wang, S. Mi, C. Xiang, Simulative and experimental investigation of transfer function of inter-turn faults in transformer windings, Electr. Power Syst. Res. 107 (2014) 1–8.
[22] A. Berzoy, A.A.S. Mohamed, O.A. Mohammed, Inter-turn short-circuit fault model for magnetically coupled circuits: a general study, in: 2016 IEEE Industry Applications Society Annual Meeting, Portland, OR, 2016, pp. 1–7.
[23] N. Chiesa, B.A. Mork, H.K. Høidalen, Transformer model for inrush current calculations: simulations, measurements and sensitivity analysis, IEEE Trans. Power Deliv. 25 (4) (2010) 2599–2608.
[24] Y. Wang, S.G. Abdusalam, W. Xu, Analytical formula to estimate the maximum inrush current, IEEE Trans. Power Deliv. 23 (2) (2008) 1266–1268.
[25] S.R. Huang, S.C. Chung, B.N. Chen, Y.H. Chen, A harmonic model for the nonlinearities of single-phase transformer with describing functions, IEEE Power Deliv. 18 (3) (2003) 815–820.
[26] R.L. Herman, An Introduction to Fourier Analysis, CRC Press, 2016.
[27] I. Hernandez, F. de Leon, J.M. Cañedo, J.C. Olivares-Galvan, Modelling transformer core joints using Gaussian models for the magnetic flux density and permeability, IET Electr. Power Appl. 4 (9) (2010) 761–771.

Anexo B

Measurement 117 (2018) 371–379

Contents lists available at ScienceDirect

Measurement

journal homepage: www.elsevier.com/locate/measurement

The application of EMD-based methods for diagnosis of winding faults in a transformer using transient and steady state currents

Arturo Mejia-Barron[a], Martin Valtierra-Rodriguez[a,*], David Granados-Lieberman[b], Juan C. Olivares-Galvan[c], Rafael Escarela-Perez[c]

[a] ENAP-RG, Facultad de Ingeniería, Universidad Autonoma de Queretaro (UAQ), Campus San Juan del Río, Rio Moctezuma 249, Col. San Cayetano, C. P. 76807 San Juan del Río, Qro., Mexico

[b] ENAP-RG, Departamento de Ingeniería Electromecánica, Instituto Tecnológico Superior de Irapuato (ITESI), Carr. Irapuato-Silao km 12.5, Col. El Copal, C. P. 36821 Irapuato, Gto., Mexico

[c] Departamento de Energía, Universidad Autonoma Metropolitana (UAM), Azcapotzalco Campus, Av. San Pablo 180, Col. Reynosa Tamaulipas, C. P. 02200 Ciudad de México, Mexico

ARTICLE INFO

Keywords:
Empirical mode decomposition
Fault diagnosis
Inrush current signals
Short-circuited turns
Steady state current
Transformer
Transient current

ABSTRACT

The application of signal processing techniques is a fundamental step for fault diagnostic methodologies. The application of empirical mode decomposition (EMD)-based methods such as classic EMD, ensemble EMD (EEMD), and complete EEMD (CEEMD) is presented in this work for the analysis of inrush current signals. This analysis leads to the detection of short-circuited turns in transformers. Results show that CEEMD provides the best performance, as it readily extracts the information related to the fault, requiring of acceptable computational resources. Actual inrush current signals of a transformer with short-circuited turns are also considered. The number of short-circuited turns ranges from 5 to 40. Useful indices, such as the Shannon Entropy, Energy, and root-mean-square value, are obtained from the information provided by the CEEMD approach. These indices are analyzed for both the transient state and the steady state of the current signals, providing the proper quantification of the fault severity.

1. Introduction

Transformers are among the most important elements in power systems [1–3]. In general, a transformer is a robust electric machine, however it is susceptible to different faults due to inherent operating conditions [4,5]. Hence, the development and application of condition monitoring systems, diagnostics systems, and protection schemes are particularly important [6–9] for minimizing the negative effects that transformer faults have on utilities and users. These systems are generally based on signal processing techniques which are used to detect or extract features associated to specific faults. In particular, the proper detection of short-circuit faults in transformer windings has attracted the interest of many researchers around the world [10], as the correct discrimination between inrush currents and internal fault currents is a challenging task.

Many signal processing techniques in the time, frequency, and time-frequency domains, as well as methodologies that use artificial intelligence algorithms have been reported in literature over the past few years to deal with the problem of fault detection [11–29]. In [11,12], the Fourier transform (FT) has been used to extract harmonic information related to the fault nature. A modification, called Empirical Fourier transform, has been presented in [13] to enhance the performance of FT, where the waveform characteristics of the current signals for internal fault, inrush, and current-transformer saturation conditions are considered. Although promising results have been obtained, some shortcomings of FT have to be taken into consideration; for instance, FT considers that the signal into the analyzed time-window is stationary which is not true for transient phenomena [14], compromising the accuracy of the results. As a partial solution, the wavelet transform (WT) has been explored [14–22]. In [14–17], the WT is implemented using high- and low-pass filters and different mother wavelets such as the Symlet and Daubechies; in addition, indices based on summation [15] and median absolute deviation [16] of wavelet coefficients, as well as peak values [17] for fault discrimination have been proposed. Wavelet analysis has been also combined with classification techniques such as support vector machines [18,19] and artificial neural networks [20] for discriminating different operating conditions. Other wavelet-based approaches such as wavelet packet transform [21] and wavelet

---

* Corresponding author.

E-mail addresses: arturo.mejia@enap-rg.org (A. Mejia-Barron), martin.valtierra@enap-rg.org (M. Valtierra-Rodriguez), david.granados@enap-rg.org (D. Granados-Lieberman), jolivares@correo.azc.uam.mx (J.C. Olivares-Galvan), r.escarela@ieee.org (R. Escarela-Perez).

https://doi.org/10.1016/j.measurement.2017.12.003
Received 20 August 2017; Received in revised form 19 November 2017; Accepted 4 December 2017

correlation modes [22] have been also recently presented. In the aforementioned works, the effectiveness and usefulness of the WT as a signal processing technique have been demonstrated; however, special attention must be given to the choice of the mother wavelet since the results heavily depend on this selection [19]. Other schemes have explored autoregressive models [23], S-transform [24], principal component analysis [25], Clarke's transform [26], normalized grille curves [27], gradient method [28], and higher order statistics [29]. With the aim at overcoming some of the shortcomings of reported fault detection methods, the application of new and novel signal processing techniques is desirable. In the past years, a method called empirical mode decomposition (EMD) has been presented in the literature for the analysis of signals with transient, non-linear, and non-stationary properties [30–32]. In addition, this technique does not require a parameter configuration as other signal processing techniques, e.g., the WT requires to choose both the decomposition level and wavelet mother. Moreover, a comparative study has demonstrated that the EMD method outperforms the performance of WT for waveform reconstruction [32]. Finally, other works have successfully proposed novel methodologies for specific applications, e.g., extraction of harmonics [33] and power quality analysis [34], exploiting the inherent capabilities of EMD. It is worth noting that other EMD-based methods such as ensemble EMD (EEMD) [35] and complete EEMD (CEEMD) [36] have been also presented in the literature for different applications. However, the application of EMD-based methods to the analysis of inrush currents with the presence of internal faults has not been reported yet. So, it would be desirable to bridge this open research gap.

In this work, the application of EMD-based methods, i.e., EMD, EEMD, and CEEMD, for the analysis of inrush current signals with the presence of inter-turn faults is presented. These methods have not been explored on this particular topic to the best of the authors' knowledge. The performance and computational burden of EMD, EEMD, and CEEMD methods using synthetic signals are firstly analyzed. These simulated signals correspond to an inrush current signal with inter-turn fault effects. The goal is to quantify the capacity of the presented methods for extracting information related to the fault. Secondly, the analysis is applied to real inrush current signals. These signals are acquired from a transformer adapted for having either a healthy condition or inter-turn faults. Different fault severity levels that range from 5 to 40 short-circuited turns are considered. Shannon entropy (*SE*), *Energy*, and root-mean-square (*RMS*) indices are obtained from the processing analysis to assess the severity of inter-turn faults during both the transient and steady states of the current signal. Results demonstrate both the advantages of CEEMD for the analysis of inrush currents and the effectiveness of the analyzed indices for assessing the fault severity.

2. Theoretical background

2.1. Empirical mode decomposition

EMD is an adaptive method developed for analysis of signals with transient, non-linear, and non-stationary properties [30–32]. In general, this method decomposes a signal, $x(t)$, into a set of functions called intrinsic mode functions (IMFs). An IMF is a function that satisfies two conditions: (1) the number of extrema and number of zero crossings in the signal must be either equal or different at most by one, and (2) the mean value of the envelope defined by the local maxima and the envelope defined by the local minima is zero [30]. In order to extract each IMF, a process called sifting process has to be carried out. Firstly, the extrema of the signal $x(t)$, i.e., the local maxima and minima points of $x(t)$, are identified. Then, they are connected using cubic-spline interpolation to obtain both an upper envelope (maxima points) and a lower envelope (minima points). The mean of the envelopes is designated as m_1. The first oscillation mode is obtained using m_1 as follows [30]:

$$x(t) - m_1 = h_1 \tag{1}$$

If h_1 is not an IMF, i.e., it does not satisfy the two conditions stated above, a new oscillation mode has to be computed using (1) but h_1 is treated as $x(t)$, i.e., $h_1 - m_{11} = h_{11}$. The process can be repeated until the oscillation mode becomes an IMF. The iterative procedure is given by [30]:

$$h_{1(k-1)} - m_{1k} = h_{1k} \tag{2}$$

The resulting signal is the first IMF, $c_1 = h_{1k}$. The following step calculates the residue $r_1 = x(t) - c_1$ and checks if r_1 is a monotonic function from which no more IMFs can be extracted. If r_1 is not a monotonic function, the procedure is repeated but r_1 is now $x(t)$ in (1). On the contrary, if r_1 is a monotonic function, the process is finished. The input signal can be recovered from both the IMFs and the last residue as [30]:

$$x(t) = \sum_{i=1}^{n} c_i + r_n \tag{3}$$

2.2. Ensemble EMD

A noise-assisted method called EEMD is presented in [35]. The following steps describe the EEMD algorithm. Firstly, new signals have to be generated using both the input signal $x(t)$ and different white-noise series $n_i(t)$, i.e., $x_i(t) = x(t) + n_i(t)$ for $i = 1, 2, \ldots, m$, where m is the number of trials. Then, the EMD method has to be applied to each trial. Finally, a true IMF, indexed with j, is computed as follows [36]:

$$EEMD_{cj}(t) = \frac{1}{m} \sum_{i=1}^{m} c_{ij}(t) \tag{4}$$

where $c_{ij}(t)$ is the IMF indexed with j for the trial i. The number of trials should be as large as possible for a reliable result.

2.3. Complete EEMD

The CEEMD method is a variation of EEMD [36]. In EEMD method, each trial $x_i(t)$ is decomposed independently; therefore, one residue r_i is obtained for each trial. On the contrary, CEEMD method provides a unique first residue as follows:

$$r_1 = x(t) - \text{IMF}_1 \tag{5}$$

where IMF_1 is a true IMF obtained in the same way as in EEMD method [36]. Then, an ensemble of r_1 plus different realizations is carried out in order to obtain the true IMF_2. The next residue is given by $r_2 = r_1 - IMF_2$. This procedure is repeated until all the true IMFs are obtained.

3. Application of EMD-based methods

New techniques and methodologies for signal processing in many research fields are usually tested and validated using synthetic signals [37–40]. Their use allows both the establishment of reference values and the deletion of unknown events in the data. If the reference values are known, differences or errors obtained using the in-test method can be measured. In this regard, a synthetic signal is employed in this work to observe the performance of EMD-based methods. The proposed signal is composed of three signals. The first signal is a train of Gaussian functions multiplied by an exponential function, leading to an inrush current waveform (see Fig. 1a).

The synthetic signal is analytically given by:

$$G_T = (Ae^{-\tau t})\left(\sum_{i=1}^{G} e^{\frac{-(t-p_i)^2}{2\sigma^2}}\right) \tag{6}$$

where A is the amplitude of the signal, τ is the exponential decay constant, G is the number of Gaussian functions, t is the time, p_i represents the time position indexed with i of the center of each Gaussian function, and σ is the standard deviation (width of the "bell"). The following values are set: $A = 2$, $\tau = 70$, $G = 6$, $\sigma = 0.001$, t ranges from

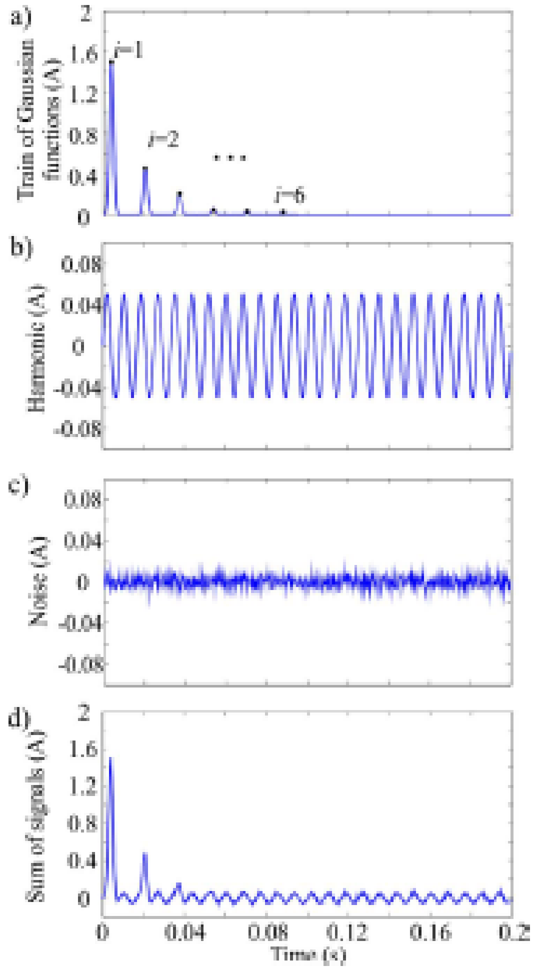

Fig. 1. Synthetic signal: (a) train of Gaussian functions, (b) harmonic component, (c) noise, and (d) final signal.

0 to 0.2 s with a sampling frequency of 6000 samples/s, and p_i takes the following values $1/(4f)$, $5/(4f)$, $9/(4f)$, $13/(4f)$, $17/(4f)$, and $21/(4f)$ for i equal to 1, 2, …, 6, respectively. f is the nominal frequency, i.e., 60 Hz. The second signal is a harmonic component to represent the effect of an inter-turn fault (see Fig. 1b). This signal is given by:

$$H_C = A_H \sin(2\pi f_H t) \tag{7}$$

where A_H and f_H are the amplitude and frequency of the signal, respectively. A_H and f_H are set to 0.05 A and 120 Hz, respectively. t follows the definition given above. Finally, the third signal is a 30 dB Gaussian white noise to represent the unavoidable noise that is present in real signals (see Fig. 1c). Fig. 1d shows the resulting signal, i.e., the sum of all the components. It is worth noting that this signal is not intended to represent a real inrush current since the goal is only to observe the capabilities of EMD-based methods to decompose the synthetic signal into the three original components. Nonetheless, the proposed signal follows somehow the behavior of a real one [13,16,28,29]. Fig. 2 shows the obtained results. They are organized in three columns. The first column presents the seven IMFs obtained using EMD method, whereas the second and third columns present the results obtained using EEMD and CEEMD methods, respectively. It is observed in Fig. 2 that most of the noise signal appears in the IMF 1 for the three methods. The harmonic component seems somehow to be in the IMF 3, IMF 4, and IMF 6 for EMD, EEMD, and CEEMD methods, respectively. The signal that represents the sum of Gaussian functions may be seen in the IMF 7 of the CEEMD method, which is not evident for the other methods.

In order to quantify the decomposition accuracy, the Pearson correlation coefficient is computed. This coefficient indicates the linear correlation between two variables, x and y [40]. It can take values from −1 (perfect negative correlation, i.e., y decreases as x increases) to +1 (perfect positive correlation, i.e., y increases as x increases), where 0 indicates that there is not linear correlation. It is computed with:

$$R = \frac{1}{N-1}\sum_{i=1}^{N}\left[\left(\frac{x_i-\overline{x}}{\sigma_x}\right)\left(\frac{y_i-\overline{y}}{\sigma_y}\right)\right] \tag{8}$$

where N is the number of samples, x_i is the sample indexed with i, $\overline{x}$ and σ_x are the mean and standard deviation of the signal x, respectively. The same definitions apply for the y parameters. Table 1 presents the correlation results. All the IMFs are correlated with the three reference signals, i.e., the ones shown in Fig. 1 are correlated with those shown in Fig. 2.

Numerical results indicate that the noise component presents the highest correlation values with the IMF 1, i.e., 0.3422 for EMD, 0.8055 for EEMD, and 0.8051 for CEEMD. For the harmonic component, the highest correlation values are with IMF 3 (EMD, 0.3866), IMF 4 (EEMD, 0.5670), and IMF 5 (CEEMD, 0.4458). For the latter, a high correlation with IMF 6 (CEEMD, 0.2373) is also observed, indicating the presence of the harmonic components. Finally, the signal that represents the sum of Gaussian functions has the highest correlations values with IMF 4 (EMD, 0.4650), IMF 4 (EEMD, 0.6743), and IMF 7 (CEEMD, 0.5537). It is worth noting that for the EEMD method both the harmonic component and the Gaussian functions present the highest correlation values with the IMF 4. This condition can compromise the discrimination between components; yet, IMF 5 presents a high correlation with the Gaussian functions, which can be used to discriminate between components. It is important to mention that several cases present negative values, e.g., the R values for H_C with IMF 3 and $Noise$ with IMF 7 using CEEMD are −0.0160 and −0.0011, respectively; as stated above, these values indicate a poor negative correlation. On the other hand, the computational requirements are also important aspects during the application of signal processing methods. In this regard, the number of iterations of EEMD and CEEMD are obtained in order to assess the computational burden. For the results shown in Fig. 2, EEMD and CEEMD require 240,194 and 62,999 ensembles, respectively. It is evident from all the obtained results that the CEEMD method is the most suitable tool for this type of analysis, as it presents an acceptable computational burden and high correlation values. Although the EEMD method also gives acceptable correlation results, the number of ensembles is almost four times bigger than the one required by the CEEMD technique. The EMD method presents the lowest computational burden (a desirable feature for online diagnosis systems), as it does not require an ensemble number; however, its decomposition presents the lowest correlation values. Hence, real inrush current signals with inter-turn faults are only analyzed with the CEEMD method in the next section.

4. CEEMD method for diagnosis of inter-turn faults

The application of the CEEMD method to the analysis of real inrush current signals with inter-turn faults is presented in this section. Some indices are also presented to quantify the fault severity from the information provided by CEEMD.

4.1. Experimental setup

The experimental setup used in this work is shown in Fig. 3a. A single-phase transformer is used to produce the inrush current phenomenon under healthy and different inter-turn fault conditions. The transformer for the tests is a resin impregnated dry-type with a three-limb core, a power rating of 120 VA, a rated current of 0.94 A, a rated input voltage of 127 V, a primary winding of 474 turns, and a secondary

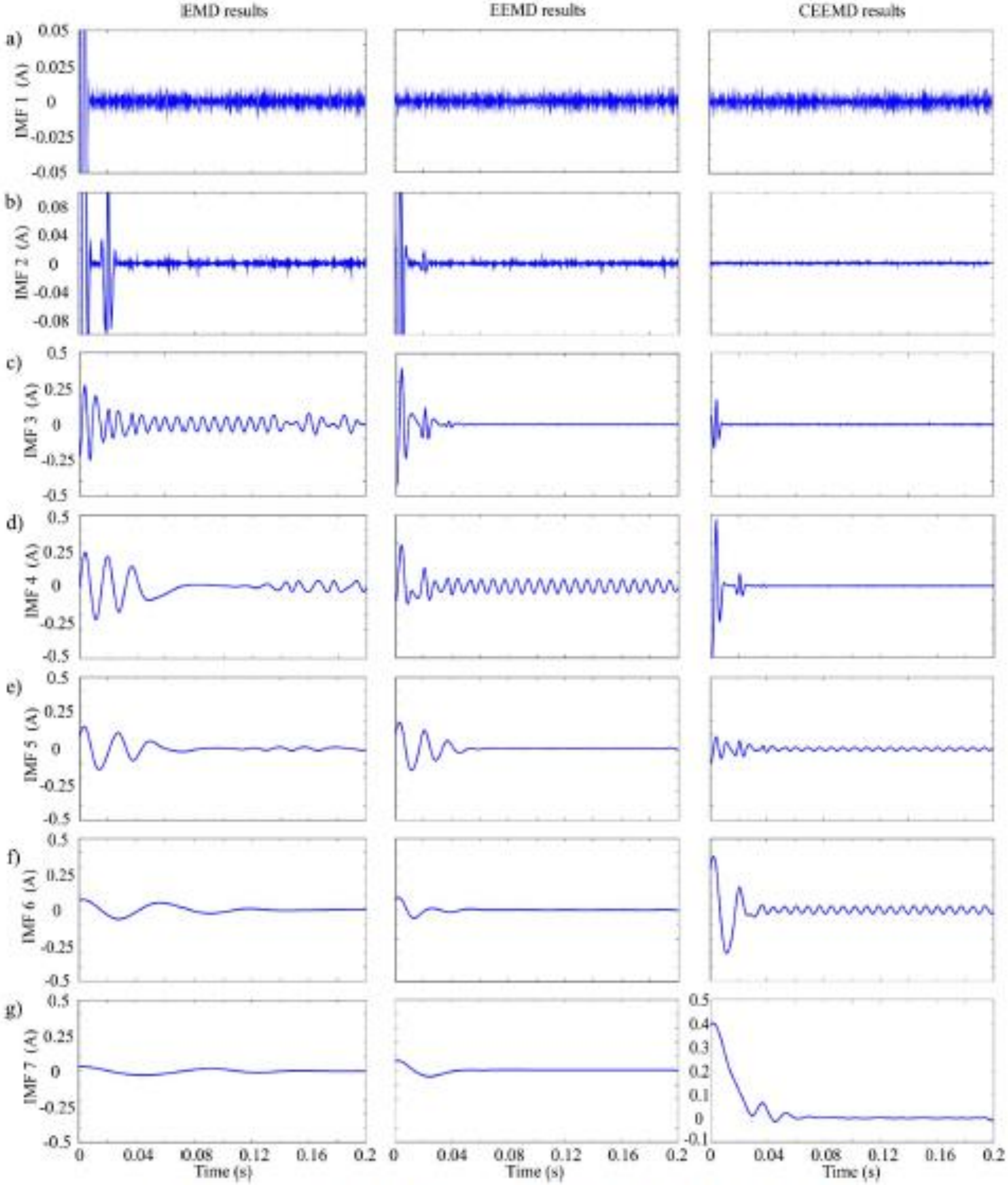

Fig. 2. Results of EMD-based methods: (a) IMF 1, (b) IMF 2, (c) IMF 3, (d) IMF 4, (e) IMF 5, (f) IMF 6, and (g) IMF 7.

winding of 91 turns. Eight taps are available at the primary winding to achieve several turn to turn fault conditions. These conditions are: 5, 10, 15, 20, 25, 30, 35, and 40 short-circuited turns. The energization process is carried out using a solid-state relay controlled with a zero-crossing detector in order to maintain the switching angle as zero in all the tests, obtaining a maximum peak current of 20 A. The transformer is always operated at rated conditions. The flowchart of the signal acquisition process is shown in Fig. 3b. A Tektronix oscilloscope TDS 2024 is used for storing the signals with a sampling frequency of 5 kHz. Current signals are measured by means of a Tektronix A622 sensor with a range of 50 mA to 100 A. The transformer switching-on is controlled by means of the FRDM-k64 microcontroller-based platform, driving the solid-state relay through the zero-crossing detector circuit. Finally, the inrush current signals of the transformer have a duration of 0.25 s in

Table 1
Correlation results.

	EMD			EEMD			CEEMD		
	Noise	H_s	G_s	Noise	H_s	G_s	Noise	H_s	G_s
IMF 1	0.3422	−0.0098	0.1520	0.8055	0.0055	0.0018	0.8051	0.0056	0.0023
IMF 2	0.0123	0.0025	0.3911	0.0516	−0.0267	0.3072	0.5350	0.0119	0.0629
IMF 3	0.0213	0.3866	0.4589	0.0156	0.0431	0.5514	0.0566	−0.0160	0.3298
IMF 4	0.0028	0.1336	0.4650	0.0115	0.5670	0.6743	0.0196	−0.0309	0.4494
IMF 5	0.0085	0.0196	0.2683	0.0102	0.0542	0.5751	0.0067	0.4458	0.4731
IMF 6	0.0242	0.0173	0.1683	0.0106	0.0478	0.5113	0.0082	0.2373	0.5364
IMF 7	0.0021	0.0190	0.2517	0.0017	0.0392	0.3790	−0.0011	0.0481	0.5537

order to acquire both the entire inrush current phenomenon and a steady state current signal. All the analysis is implemented on Matlab software.

4.2. CEEMD results

Results obtained using the CEEMD method are depicted in Fig. 4. Fig. 4a shows the real inrush current signals, where nine signals can be observed. They correspond to the following conditions: 0 (healthy), 5, 10, 15, 20, 25, 30, 35, and 40 short-circuited turns. Fig. 4b–h show the IMFs obtained for each inrush current signal. Similar to the synthetic signal case, results of IMF 1 in Fig. 4b show the noise of the signals. The most of the harmonic content appears in signals of the IMF 6 (see Fig. 4 g), where a small increment in amplitude is observed according to the fault severity level, i.e., the higher the severity of the fault, the higher the amplitude. Information related to the inrush current is observed in the signals of the IMF 7 (see Fig. 4 h). In general, it is demonstrated that the CEEMD method is a suited technique for the analysis of inrush current signals with the presence of inter-turn faults since information related to the fault can be split up. This information can be advantageously used for diagnosis purposes.

4.3. Indices for fault diagnosis

Indices for fault diagnosis can be computed from the information provided by the CEEMD method. Firstly, information of IMFs 6 and 7 has to be considered. These IMFs present changes in their waveforms which can be associated to the fault (see Fig. 5a). In this work, the *SE*, *RMS*, and *Energy* values are analyzed as potential indices to diagnose the inter-turn fault and characterize its severity. It should be pointed out that these indices are chosen because they have proven to be efficient and reliable in other electric applications [39,41–43]; for instance, the *RMS* index has provided valuable information to characterize voltage and current signals within a power quality context [39], the *SE* index has been successfully used to diagnose induction motor faults [41], and the *Energy* index has allowed the assessment of both power transformers using vibrations signals [42] and voltage sags [43]; however, many other indices can be applied and researched, leaving the open doors to new proposals. The aforementioned indices are computed as follows:

$$SE = -\sum_{i=1}^{M} p(\beta_i)\log_2(p(\beta_i)) \tag{9}$$

where β_i represents the values of a signal x that can be taken, i.e., $\beta_1,\beta_2,\beta_3,\ldots,\beta_M$ with M possible outcomes, $p(\beta_i)$ is the probability of β_i in the signal x, and $\log_2(\cdot)$ represents the binary logarithm [41]. The *RMS* [44] and *Energy* [43] values are given by:

$$RMS = \sqrt{\frac{1}{N}\sum_{i=1}^{N} x_i^2} \tag{10}$$

$$Energy = \sum_{i=1}^{N} x_i^2 \tag{11}$$

where N is the number of samples and x_i represents the samples of a signal x.

The indices are explored in two states: transient and steady cases. The goal is to show that the CEEMD method is capable of providing useful information to diagnose the inter-turn fault during both the transient and steady states through the application of numerical indices. Firstly, current signals of IMF 7 are considered to analyze the transient state. This state ranges from 0 s to 0.13 s (see Fig. 5a). The obtained results are presented in Fig. 5c, where the first row corresponds to *SE* values, the second one is for *RMS* values and the third one is for *Energy* values. On the other hand, current signals of IMF 6 are considered to analyze the steady state. This state ranges from 0.13 s to

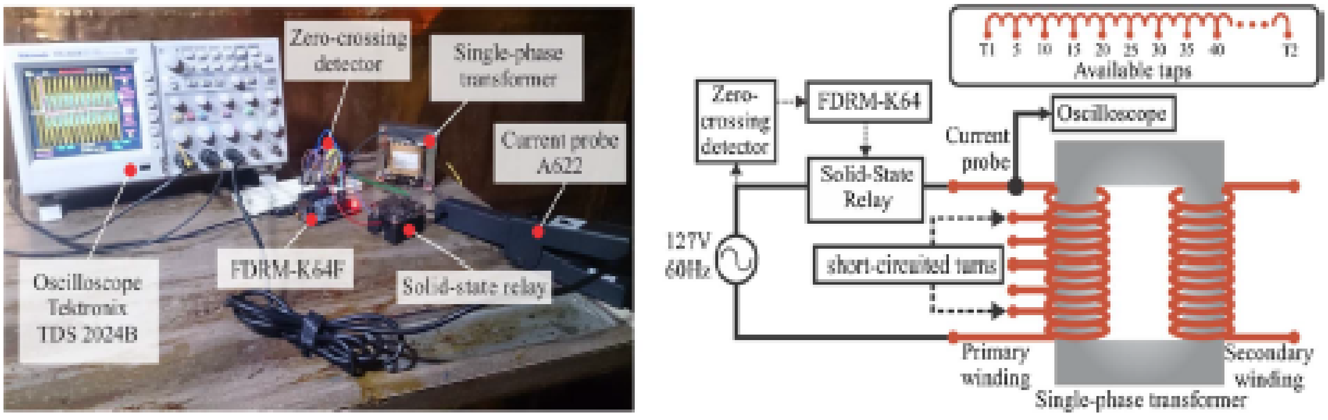

a) b)

Fig. 3. Experimentation: (a) experimental setup and (b) flowchart for acquisition of inrush current signals with inter-turn faults.

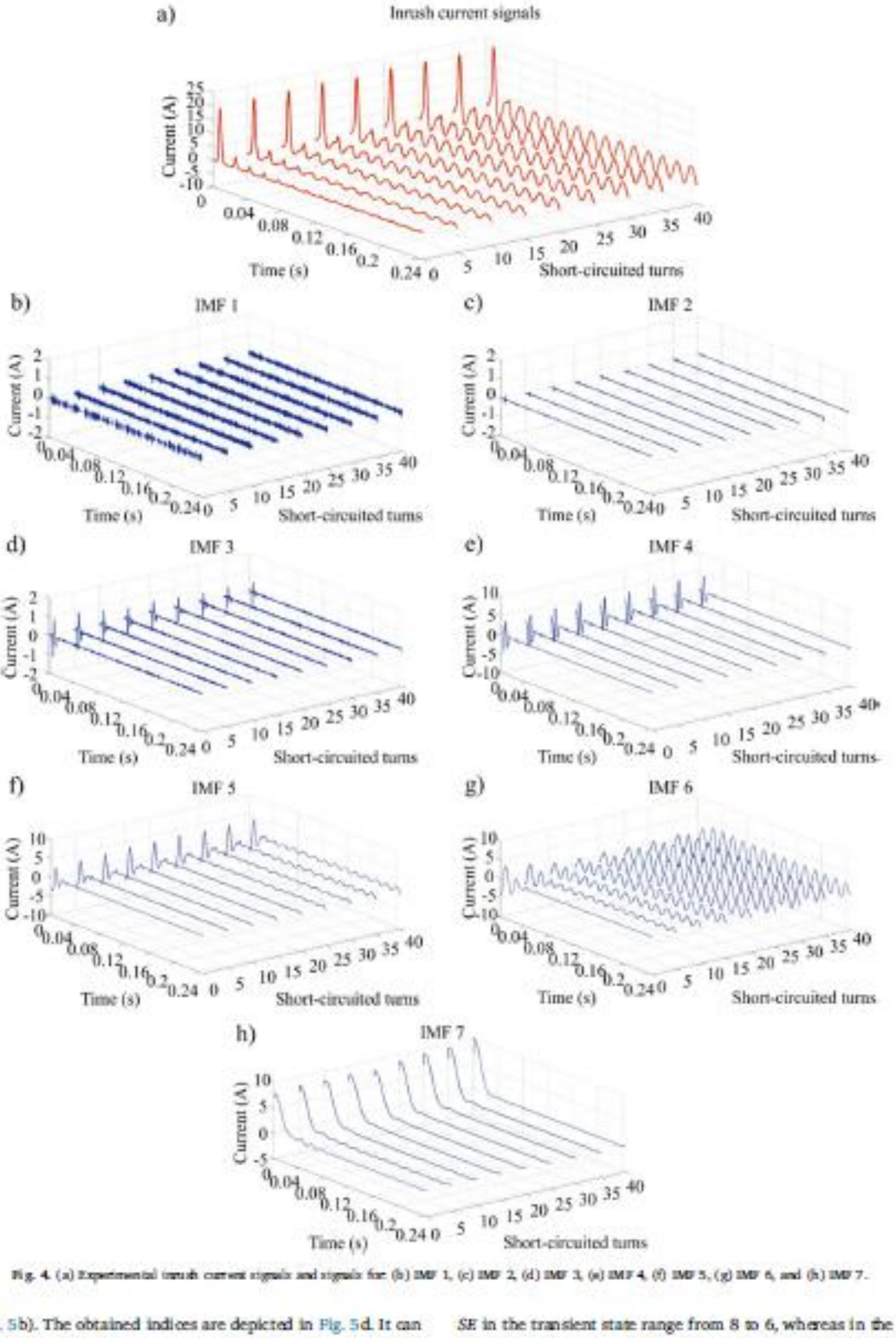

Fig. 4. (a) Experimental inrush current signals and signals for: (b) IMF 1, (c) IMF 2, (d) IMF 3, (e) IMF 4, (f) IMF 5, (g) IMF 6, and (h) IMF 7.

0.25 s (see Fig. 5b). The obtained indices are depicted in Fig. 5d. It can be observed from results of Fig. 5c that all the indices are sensitive to the fault severity level since they change their amplitude according to the fault. The highest change is observed in the *Energy* index. The indices in Fig. 5d indicate that is also possible to discriminate the fault severity, even with a larger rate of change. For instance, the values of *SE* in the transient state range from 8 to 6, whereas in the steady state they range from 4 to 8. The largest change is observed in the *Energy* index. This index shows a proportional increment according to the fault severity, which makes it a suitable tool for characterizing the fault severity in a fault diagnosis system.

Fig. 6 presents the results for the ratio of indices, i.e., the division

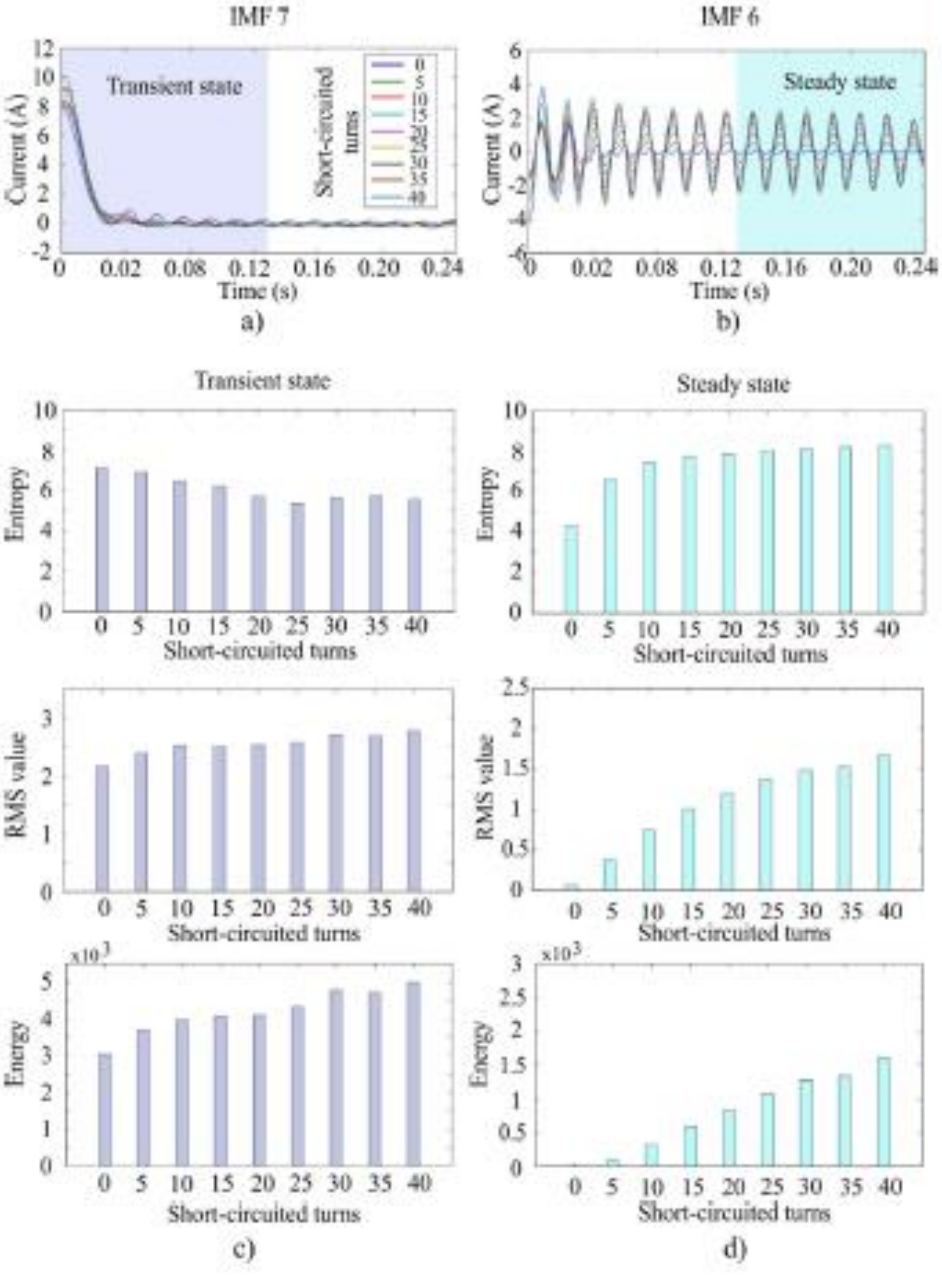

Fig. 5. Indices for fault diagnostic (a) current signals for IMF 7, (b) current signals for IMF 6, (c) results for transient state of IMF 7, and (d) results for steady state of IMF 6.

between the indices for IMF 6 and the indices for IMF 7 by considering either the transient state signal (TSS) or the steady state signal (SSS) (see Fig. 6a). Therefore, the transient state ratio (*TSR*) and steady state ratio (*SSR*) indices are given by:

$$TSR_{SE} = \frac{SE(TSS,IMF6)}{SE(TSS,IMF7)}$$

$$SSR_{SE} = \frac{SE(SSS,IMF6)}{SE(SSS,IMF7)} \tag{12}$$

$$TSR_{RMS} = \frac{RMS(TSS,IMF6)}{RMS(TSS,IMF7)}$$

$$SSR_{RMS} = \frac{RMS(SSS,IMF6)}{RMS(SSS,IMF7)} \tag{13}$$

$$TSR_{Energy} = \frac{Energy(TSS,IMF6)}{Energy(TSS,IMF7)}$$

$$SSR_{Energy} = \frac{Energy(SSS,IMF6)}{Energy(SSS,IMF7)} \tag{14}$$

where *SE*(·), *RMS*(·), and *Energy*(·) are computed using (9)–(11), respectively.

It should be pointed out that the ratio of indices for fault diagnosis of inter-turn faults in transformers is presented and analyzed in this work since it follows the essence of other reported indices, e.g., ratio of higher-order statistics and second harmonic ratio [29], besides that, the ratio of indices provides normalized values which allow establishing a fault criterion regardless of the magnitude or other features of the input signals. In this regard, the results shown in Fig. 6b indicate that the ratio of indices can provide normalized values for fault diagnosis, e.g., the *SE* ratio with a value of 1 (dotted red line) indicates a healthy condition whereas values greater than 1 indicate fault conditions. This behavior can be useful in automatic diagnosis tasks. The reference values for healthy conditions in the transient state regions are 0.5 and 0.25 (dotted red lines) for the *RMS* and *Energy* ratios, respectively; however, these values are sensitive to severity levels greater than 10 short-circuited turns, i.e., faults of 5, 10, and 15 short-circuited turns can be misled with a healthy condition. The reference values for healthy conditions using *RMS* and *Energy* values in the steady state regions are 0.7 and 0.5, respectively. Unlike other indices, it is observed in Fig. 6b

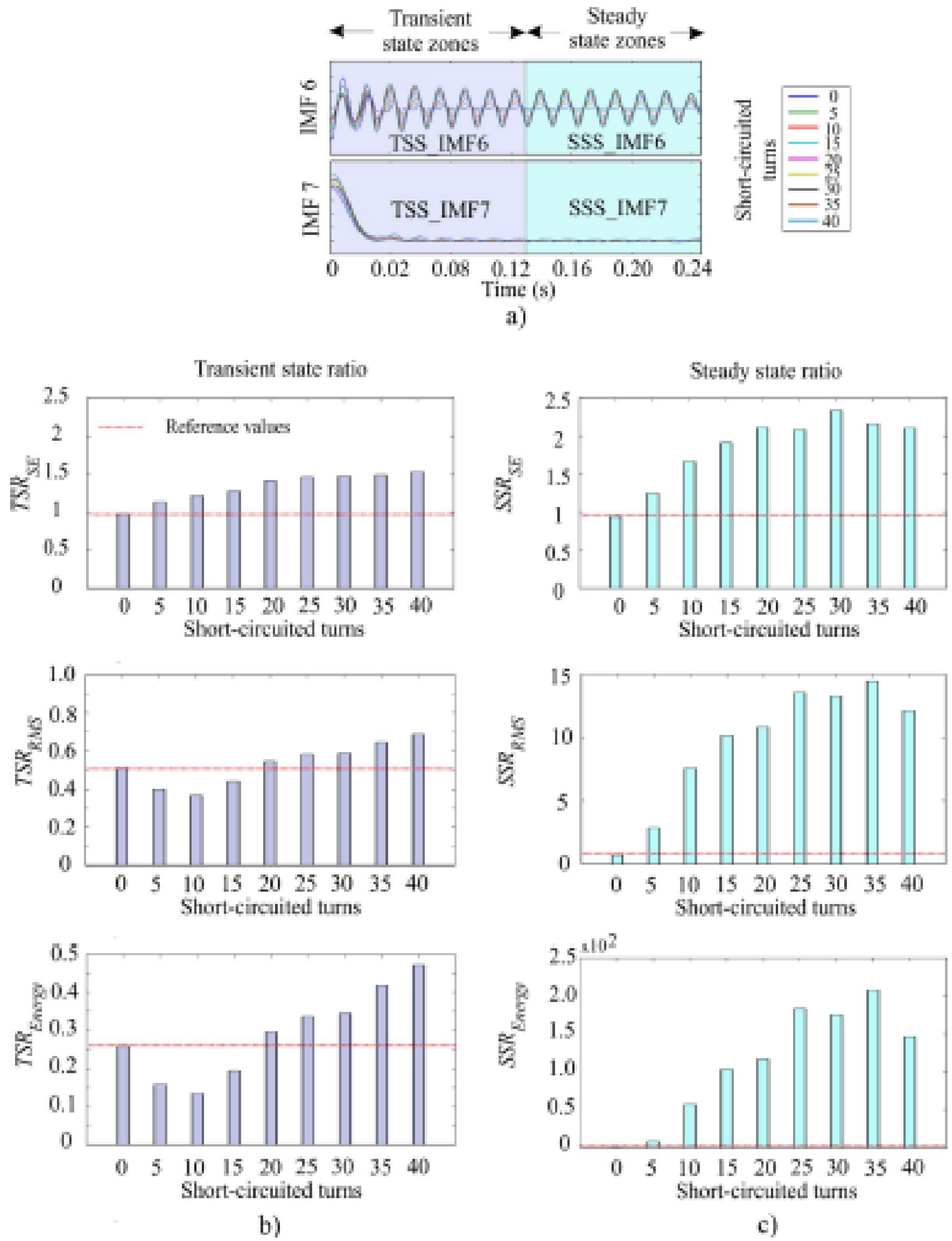

Fig. 6. Normalized indices for fault diagnostic (a) current signals for both IMF 6 and IMF 7, and results for the ratio of indices during either (b) transient state or (c) steady state by considering both IMF6 and IMF 7.

that the ratio of *SE* values in the transient state regions provides: a normalized value of 1, a proportional increment according to the fault severity, and a discrimination from 5 short-circuited turns. Thus, *SE* demonstrates to be the most suitable index, if the ratio of indices is considered.

5. Conclusions

Application of signal processing techniques is of paramount importance for fault diagnosis since it allows the proper detection of features associated to the fault in a measured signal. Application of EMD, EEMD, and CEEMD methods for the analysis of inrush current signals is presented in this work. To the best of the author's knowledge, these methods have not been previously applied in this topic. The analysis is focused on the extraction of information related to inter-turn faults in transformers using IMFs. Firstly, the methods are tested using synthetic signals. Results indicate that the CEEMD method provides the best decomposition results since the IMFs extracted by this method present the highest correlation values. The EEMD method presents also acceptable correlation results, however the number of iterations for this analysis is almost four times bigger than the ones required by the CEEMD approach. The EMD method requires the lowest computational resources, as it does not require an ensemble number; however, its decompositions display the lowest correlation values.

Since the CEEMD method provides the best results in terms of performance and complexity, it is chosen to analyze real inrush current signals. These signals correspond to different severity levels of inter-turn faults, i.e., 5, 10, 15, 20, 25, 30, 35, and 40 short-circuited turns. For these signals, useful information to carry out fault diagnosis appears in both IMF 6 and IMF 7, demonstrating that the CEEMD method is a suitable tool for analysis of this type of signals. Although the CEEMD is only applied to the analysis of inter-turn faults, this signal processing technique can be applied to the diagnosis of other faults; in fact, information of such faults may appear in other IMFs, facilitating the diagnosis of multiple faults. *SE*, *RMS*, and *Energy* indices are computed from the information obtained in IMF 6 and IMF 7 for both the transient state (IMF 7) and the steady state (IMF 6) to diagnose the fault and characterize its severity. The results obtained indicate that a suitable and reliable transformer diagnosis can be assessed from these indices. In particular, the *Energy* index presents the best results for both the transient state (IMF 7) and the steady state (IMF 6). Nonetheless, the ratio of *SE* values gives the best results if a normalized index is considered. Although this work has tested specific indices, many others can be investigated to find more sensitive ones.

Other electrical faults such as phase to phase and phase to ground, as well as other types of signals such as voltages and magnetic fluxes can be analyzed with the proposed technique, a task that the authors will perform in the near future. Besides, long time transformer excitation under short-circuited fault conditions will be studied to analyze its behavior before a catastrophic event in the transformer occurs. In addition, the hardware implementation of the CEEMD method will be performed in order to provide online diagnosis systems.

Acknowledgements

This work was partially supported by CONACYT Scholarship 296868 and by FOFI-UAQ 2015 under Project FIN2016-33.

References

[1] B. García, J.C. Burgos, Á. Alonso, Winding deformations detection in power transformers by tank vibrations monitoring, Electr. Power Syst. Res. 74 (1) (2005) 129–138.

[2] H.A. Illias, X.R. Chai, Hybrid modified evolutionary particle swarm optimisation-time varying acceleration coefficient-artificial neural network for power transformer fault diagnosis, Measurement 90 (2016) 94–102.

[3] M.M. Islam, G. Lee, S.N. Hettiwatte, A review of condition monitoring techniques and diagnostic tests for lifetime estimation of power transformers, Electr. Eng. (2017) 1–25.

[4] M. Wang, A.J. Vandermaar, K.D. Srivastava, Review of condition assessment of power transformers in service, IEEE Electr. Insul. Mag. 18 (6) (2002) 12–25.

[5] J.L. Guardado, J.L. Naredo, P. Moreno, C.R. Fuerte, A comparative study of neural network efficiency in power transformers diagnosis using dissolved gas analysis, IEEE Trans. Power Del. 16 (4) (2001) 643–647.

[6] B. Wicaksono, H. Kong, L.V. Markova, H.G. Han, Application of fluorescence emission ratio technique for transformer oil monitoring, Measurement 46 (10) (2013) 4161–4165.

[7] B. Sarkar, C. Koley, N.K. Roy, P. Kumbhakar, Condition monitoring of high voltage transformers using fiber bragg grating sensor, Measurement 74 (2015) 255–267.

[8] A.A. Abdoos, S.A. Gholamian, M.M.A. Takami, A precise scheme for detection of current transformer saturation based on time frequency analysis, Measurement 94 (2016) 692–706.

[9] T. Lei, M. Faifer, R. Ottoboni, S. Toscani, On-line fault detection technique for voltage transformers, Measurement 108 (2017) 193–200.

[10] M. Tripathy, R.P. Maheshwari, H.K. Verma, Advances in transformer protection: a review, Electr. Power Compon. Syst. 33 (11) (2005) 1203–1209.

[11] M.H. Golshan, M. Saghaian-Nejad, A. Saha, H. Samet, A new method for recognizing internal faults from inrush current conditions in digital differential protection of power transformers, Electr. Power Syst. Res. 71 (1) (2004) 61–71.

[12] M. Geethanjali, S.M.R. Slochanal, R. Bhavani, PSO trained ANN-based differential protection scheme for power transformers, Neurocomputing 71 (4) (2008) 904–918.

[13] M.S. Kumar, S.P. Simon, K. Sundareswaran, P.S.R. Nayak, N.P. Padhy, An empirical Fourier transform based power transformer differential protection, IEEE Trans. Power Del. 32 (1) (2017) 209–218.

[14] O.A. Youssef, Discrimination between faults and magnetizing inrush currents in transformers based on wavelet transforms, Electr. Power Syst. Res. 63 (2) (2002) 87–94.

[15] A.R. Sedighi, M.R. Haghifam, Detection of inrush current in distribution transformer using wavelet transform, Int. J. Electr. Power Energy Syst. 27 (5) (2005) 361–370.

[16] A.H. Eldin, M.A. Refaey, A novel algorithm for discrimination between inrush current and internal faults in power transformer differential protection based on discrete wavelet transform, Electr. Power Syst. Res. 81 (1) (2011) 19–24.

[17] P.L. Mao, R.K. Aggarwal, A wavelet transform based decision making logic method for discrimination between internal faults and inrush currents in power transformers, Int. J. Electr. Power Energy Syst. 22 (6) (2000) 389–395.

[18] S. Jazebi, B. Vahidi, M. Jannati, A novel application of wavelet based SVM to transient phenomena identification of power transformers, Energy Convers. Manage. 52 (2) (2011) 1354–1363.

[19] A.M. Shah, B.R. Bhalja, Discrimination between internal faults and other disturbances in transformer using the support vector machine-based protection scheme, IEEE Trans. Power Delivery 28 (3) (2013) 1508–1515.

[20] O. Ozgonenel, S. Karagol, Transformer differential protection using wavelet transform, Electr. Power Syst. Res. 114 (2014) 60–67.

[21] S.A. Saleh, B. Scaplen, M.A. Rahman, A new implementation method of wavelet-packet-transform differential protection for power transformers, IEEE Trans. Ind. Appl. 47 (2) (2011) 1003–1012.

[22] D. Guillén, H. Esponda, E. Vázquez, G. Idárraga-Ospina, Algorithm for transformer differential protection based on wavelet correlation modes, IET Gener. Transm. Distrib. 10 (12) (2016) 2871–2879.

[23] H. Zhang, P. Liu, O.P. Malik, A new scheme for inrush identification in transformer protection, Electr. Power Syst. Res. 63 (2) (2002) 81–86.

[24] S.R. Samantaray, B.K. Panigrahi, P.K. Dash, G. Panda, Power transformer protection using S-transform with complex window and pattern recognition approach, IET Gener. Transm. Distrib. 1 (2) (2007) 278–286.

[25] E. Vazquez, I.I. Mijares, O.L. Chacon, A. Conde, Transformer differential protection using principal component analysis, IEEE Trans. Power Del. 23 (1) (2008) 67–72.

[26] D. Barbosa, U.C. Netto, D.V. Coury, M. Oleskovicz, Power transformer differential protection based on Clarke's transform and fuzzy systems, IEEE Trans. Power Del. 26 (2) (2011) 1212–1220.

[27] J. Ma, Z. Wang, Q. Yang, Y. Liu, Identifying transformer inrush current based on normalized grille curve, IEEE Trans. Power Del. 26 (2) (2011) 588–595.

[28] R.J.N. Alencar, U.H. Bezerra, A.M.D. Ferreira, A method to identify inrush currents in power transformers protection based on the differential current gradient, Electr. Power Syst. Res. 111 (2014) 78–84.

[29] L.L. Zhang, Q.H. Wu, T.Y. Ji, A.Q. Zhang, Identification of inrush currents in power transformers based on higher-order statistics, Electr. Power Syst. Res. 146 (2017) 161–169.

[30] N.E. Huang, Z. Shen, S.R. Long, M.C. Wu, H.H. Shih, Q. Zheng, N.C. Yen, C.C. Tung, H.H. Liu, The empirical mode decomposition and the Hilbert spectrum for nonlinear and non-stationary time series analysis, Proc. Roy. Soc. Lond. A: Math., Phys. Eng. Sci. 454 (1971) (1998) 903–995.

[31] G. Cheng, Y.L. Cheng, L.H. Shen, J.B. Qiu, S. Zhang, Gear fault identification based on Hilbert-Huang transform and SOM neural network, Measurement 46 (3) (2013) 1137–1146.

[32] D. Labate, F.L. Foresta, G. Occhiuto, F.C. Morabito, A. Lay-Ekuakille, P. Vergallo, Empirical mode decomposition vs. wavelet decomposition for the extraction of respiratory signal from single-channel ECG: a comparison, IEEE Sens. J. 13 (7) (2013) 2666–2674.

[33] J. Wu, X. Wang, X. Sun, Y. Liu, Pure harmonics extracting from time-varying power signal based on improved empirical mode decomposition, Measurement 49 (2014) 216–225.

[34] D. Camarena-Martinez, M. Valtierra-Rodriguez, C.A. Perez-Ramirez, J.P. Amezquita-Sanchez, R. de Jesus Romero-Troncoso, A. Garcia-Perez, Novel downsampling empirical mode decomposition approach for power quality analysis, IEEE Trans. Ind. Electron. 63 (4) (2016) 2369–2378.

[35] Z. Wu, N.E. Huang, Ensemble empirical mode decomposition: a noise-assisted data analysis method, Adv. Adapt. Data Anal. 1 (1) (2009) 1–41.

[36] M.E. Torres, M.A. Colominas, G. Schlotthauer, P. Flandrin, A complete ensemble empirical mode decomposition with adaptive noise, IEEE International Conference on Acoustics, Speech and Signal Processing (ICASSP), Prague, Czech Republic, 2011, pp. 4144–4147.

[37] J.P. Amezquita-Sanchez, H. Adeli, Synchrosqueezed wavelet transform-fractality model for locating, detecting, and quantifying damage in smart highrise building structures, Smart Mater. Struct. 24 (6) (2015) 1–14.

[38] R. de Jesus Romero-Troncoso, Multirate signal processing to improve FFT-based analysis for detecting faults in induction motors, IEEE Trans. Ind. Inf. 13 (3) (2017) 1291–1300.

[39] I. Urbina-Salas, J.R. Razo-Hernandez, D. Granados-Lieberman, M. Valtierra-Rodriguez, J.E. Torres-Fernandez, Instantaneous power quality indices based on single-sideband modulation and wavelet Packet-Hilbert transform, IEEE Trans. Instrum. Meas. 66 (5) (2017) 1021–1031.

[40] D. Camarena-Martinez, C.A. Perez-Ramirez, M. Valtierra-Rodriguez, J.P. Amezquita-Sanchez, R. de Jesus Romero-Troncoso, Synchrosqueezing transform-based methodology for broken rotor bars detection in induction motors, Measurement 90 (2016) 519–525.

[41] E. Cabal-Yepez, M. Valtierra-Rodriguez, R.J. Romero-Troncoso, A. Garcia-Perez, R.A. Osornio-Rios, H. Miranda-Vidales, R. Alvarez-Salas, FPGA-based entropy neural processor for online detection of multiple combined faults on induction motors, Mech. Syst. Sig. Process. 30 (2012) 123–130.

[42] K. Hong, H. Huang, Y. Fu, J. Zhou, A vibration measurement system for health monitoring of power transformers, Measurement 93 (2016) 135–147.

[43] F.B. Costa, J. Driesen, Assessment of voltage sag indices based on scaling and wavelet coefficient energy analysis, IEEE Trans. Power Delivery 28 (1) (2013) 336–346.

[44] IEEE Standard on Transitions, Pulses, and Related Waveforms, Institute of Electrical and Electronics Engineers, IEEE Std. 181-2011, September 2011.

Anexo C

electronics

Article

Shannon Entropy Index and a Fuzzy Logic System for the Assessment of Stator Winding Short-Circuit Faults in Induction Motors

Arturo Mejia-Barron [1], J. Jesus de Santiago-Perez [1], David Granados-Lieberman [2], Juan P. Amezquita-Sanchez [1] and Martin Valtierra-Rodriguez [1,*]

[1] ENAP-Research Group, CA-Sistemas Dinámicos, Facultad de Ingeniería, Universidad Autónoma de Querétaro (UAQ), Campus San Juan del Río, Río Moctezuma 249, Col. San Cayetano, San Juan del Río, Qro., C. P. 76807, Mexico; arturo.mejia@enap-rg.org (A.M.-B.); jjdesantiago@hspdigital.org (J.J.d.S.-P.); juan.amezquita@enap-rg.org (J.P.A.-S.)

[2] ENAP-Research Group, CA-Fuentes Alternas y Calidad de la Energía Eléctrica, Departamento de Ingeniería Electromecánica, Instituto Tecnológico Superior de Irapuato (ITESI), Carr. Irapuato-Silao km 12.5, Colonia El Copal, Irapuato, Guanajuato C. P. 36821, Mexico; david.granados@enap-rg.org

* Correspondence: martin.valtierra@enap-rg.org

Received: 28 November 2018; Accepted: 9 January 2019; Published: 15 January 2019

Abstract: The induction motor (IM) is one of the most important elements in industry. Although IMs are robust machines, they are susceptible to faults, where the stator winding short-circuit fault is one of the most common ones. In this work, the Shannon entropy (SE) index and a fuzzy logic (FL) system are proposed to diagnose short-circuit faults, considering both different severity levels and different load conditions. In the proposed methodology, a filtering stage based on brick-wall band-pass filters is firstly carried out. After this stage, the SE index is computed to quantify the fault severity and a FL system is applied to diagnose the IM condition in an automatic way. Unlike other works that propose some types of space transformations, the proposal is only based on a filtering stage and a time domain index, requiring low computational resources. The obtained results demonstrate the effectiveness of the proposal, i.e., the SE index quantifies the fault severity, regardless of the mechanical load, and the proposed FL system achieves a positive classification rate of 98%.

Keywords: brick-wall filter; fuzzy logic; induction motor; Shannon entropy; short-circuit fault

---

1. Introduction

In recent years, the development of monitoring systems to assess the physical condition of rotatory machinery has been vital to guaranteeing the reliability of industrial processes [1–3]. Among the rotatory machinery, the three-phase induction motor (IM), representing ~85% of the consumed power in the industry, is a default implementation in industrial processes [4] because it offers great benefits, such as low maintenance, low cost, high robustness to aggressive environments and easy control under different load conditions [5,6]. Despite these great benefits, IMs are susceptible to present electrical and mechanical faults during their service-life, which are produced mainly by power quality problems, prolonged activity times and harsh operating conditions, among other factors [1–3,5,6]. Regarding electrical faults, stator winding faults (SWFs) are one of the most dangerous and common faults in IMs [7], representing about a 36–38% of faults that can take place [8,9]. This fault, even in its incipient/early state, can produce alterations and increments in current consumption, temperature and vibrations, putting at risk the personnel, the production, the machine itself and other machines in the same line of production.

During the last 15 years, an important number of techniques and methodologies for SWF detection using the analysis of acoustic, current and vibration signals have been proposed [10–14]. Motor current signature analysis (MCSA) is one of the most used methods because of its advantages, such as possessing a non-invasive capacity, possible remote sensing, easy implementation and low implementation costs [2,9]. MCSA is mainly used to identify faults in the IM according to the analysis of frequency components found in the measured signal. Particularly, MCSA for SWF detection is employed to identify frequencies around the fundamental frequency or harmonic components [15]. In the literature, diverse signal processing algorithms for stator winding short-circuit (SWSC) fault detection using MCSA have been introduced; for instance, fast Fourier transform (FFT) [14,16,17], wavelet transform (WT) [18–20], empirical mode decomposition-based methods (EMD) [21,22], Wigner-Ville distribution (WVD) [22], Hilbert transform (HT) [23], statistical time series model (STSM) [24], and statistical analysis (SA) [25]. Despite obtaining promising results, diverse limitations still remain. For instance, the FFT is a proficient tool to analyze time signals with stationary properties; yet, current applications in industry require continuous changes of the load applied to IMs, which can generate fluctuations in the voltage and current signals, producing non-stationary properties, therefore making the FFT method unsuitable [26]. WT is a suitable tool for analyzing signals of non-stationary nature; regrettably, it requires a fine election of the decomposition level and the wavelet mother in order to estimate adequate features that allow for correct evaluation of the IM's condition [27]. In this sense, EMD-based algorithms are used to analyze or decompose time signals of non-stationary nature according to their frequency components; yet, they are susceptible to present a phenomenon called mode mixing, which produces waves with different frequency components that are assigned to the same frequency band, complicating the identification of frequencies associated to the SWSC fault. Furthermore, the computational resources can increase depending on the EMD-method used, e.g., when the ensemble-EMD method is used [28]. HT is employed for obtaining the instantaneous frequency and the instantaneous amplitude of a time signal; but its results can be affected by the noise and the number of frequency components found in the analyzed signal [29]. WVD is a method capable of providing a time-frequency representation of time signals; yet, its results can be contaminated with spurious frequencies, frequency components that do not exist in the measured signal due to a problem called cross-term [30], compromising the ability for adequate location of the frequencies associated to the SWSC fault. STSMs are employed for modelling signals with a linear or time-invariant behavior; but, they can present problems for modelling nonlinear behaviors [31], which are greatly produced in an IM because of the dynamic loading. Further, their results are susceptible to errors due to the quantity of noise contained in the measured signal. The SA methods are employed for calculating statistical parameters of the time-domain signals, such as median, variance, standard deviation and among others, but their results can fail due to the noise and nonlinearities found in the time signal [32].

Although diverse methods for SWSC fault detection have been introduced in the literature, most of them are negatively affected by the non-stationary properties of the measured signal. These properties are generated by different factors, e.g., the variations in current consumption associated to changes in the mechanical load. In this regard, the proposal and development of efficient and reliable methodologies in terms of processing and performance are still required, mainly if they are not susceptible to the motor load, e.g., they have to be independent of the motor mechanical load in order to provide a consistent diagnosis for a large variety of industrial processes where the mechanical load can be different and time-variant.

In this paper, a new methodology to diagnose and quantify the severity of SWSC faults, where an independent fault indicator of the mechanical load is presented. The proposed methodology is based on MCSA, using the monitored current during the IM steady-state as input. It is based on three steps. Firstly, a filtering stage based on brick-wall band-pass filters is carried out. This type of filter is used as it presents great advantages, such as a rectangular frequency response and an abrupt transition between the pass and stop bands. Secondly, the Shannon entropy (SE) index is applied to the filtered signal in order to identify the short-circuit faults, considering both different severity levels and different load conditions. Other indices, such as the signal energy and the root mean square (RMS) value are tested and compared with the results obtained by the SE index. Finally, a fuzzy logic (FL) system is developed in order to classify the IM condition in an automatic way. The usefulness and effectiveness of the proposal is validated through experimentation, where a healthy (HLT) IM and an IM with short-circuited turns using four different levels of load are considered. The obtained results show that the proposal is an effective and consistent tool for diagnosing SWSC faults independently of load conditions, making it a promising solution for a large variety of industrial applications.

2. Theoretical Background

2.1. Motor Current Signal Analysis (MCSA)

MCSA is a widely used method for online condition monitoring in IMs, where the current spectra is used to obtain information associated to the motor fault. This fault information is obtained through abnormal harmonics in the stator current produced by the magnetomotive force distribution and the permeance-wave representation of the air gap [15,33].

Regarding the SWSC fault, signature patterns in different frequency components have been associated to the following equation [9,15,33]:

$$f_{st} = f_1\left\{\frac{n}{p}(1-s) \pm k\right\} \qquad k = 1,3,5,\ldots \quad n = 1,2,3,\ldots \tag{1}$$

where the values for f_{st} are the frequency components due to the SWSC fault, f_1 is the supply frequency, p is the pole-pairs and s is the slip. Different values for k and n can be tested in order to obtain the frequencies of interest, where promising results have been obtained for $k = 1$ with $n = 3$ and $n = 5$ [15].

2.2. Brick-Wall Filters

Brick-wall filters or sinc filters are idealized digital FIR (finite impulse response) filters with a rectangular frequency response, which provides an ideally flat amplitude response in the passband and an abrupt transition in the cutoff frequency [34]. Besides, a FIR filter is featured by its stability and linear phase. Then, an ideal brick-wall low-pass filter with bandwidth ω_p and zero phase provides the impulse response, as per Reference [35]:

$$g(t) = \frac{\omega_p}{2}\frac{\sin \omega_p t}{\omega_p t} \tag{2}$$

As the filter impulse response has an infinite length, making the structure implementation impossible [35], a window function $w(t)$ of length τ is applied to $g(t)$ to obtain a practical filter, which can be expressed as per Reference [35]:

$$h(t) = w(t)\frac{\omega_p}{2}\frac{\sin \omega_p t}{\omega_p t} \tag{3}$$

By using two brick-wall low-pass filters, a brick-wall band-pass filter is obtained as follows:

$$h(t)_{BP} = h(t)_u - h(t)_l \tag{4}$$

where $h(t)_u$ and $h(t)_l$ are the upper and lower band edges, respectively.

2.3. Fault Indices

In the literature, several indices have been presented for fault diagnosis. In this work, the SE, energy and RMS indices, which have proven to be efficient in other electric applications related to the diagnosis of faults in induction motors and transformers [36–39], are analyzed as potential indicators to diagnose SWSC faults.

In the information theory, SE is used to describe the uncertainty of information content provided by an event or a signal [36]; as the SWSC fault generates different frequency components, the amount of information can change, making the SE index a promising fault indicator to quantify this change. It is given by:

$$\mathrm{SE}(X) = -\sum_{i=1}^{n} p(x_i)\log_2[p(x_i)] \tag{5}$$

where $x_1, x_2, x_3, \ldots, x_n$ are the possible outcomes of an event or signal given by X, where $p(x_i)$ is the corresponding probability vector.

On the other hand, the energy and RMS indices are obtained by means of the following equations [37]:

$$\mathrm{Energy} = \sum_{i=1}^{N} [x(i)]^{2} \tag{6}$$

$$\mathrm{RMS} = \sqrt{\frac{1}{N}\sum_{i=1}^{N} [x(i)]^2} \tag{7}$$

where $x(i)$ is the signal value at the sample i and N is the total number of samples. As can be noticed, these indices somehow increase their value according to the increments in the signal amplitude $x(i)$; therefore, they can be sensitive to SWSC faults, considering that the presence of fault and its severity increase the signal amplitude from the increment of different frequency components.

2.4. *Fuzzy Logic Systems*

In general, FL systems can be used as control strategies based exclusively on FL or in combination with other methods, such as neural networks (neuro-fuzzy systems) [40–44] or classification algorithms [5,26], where features such as simplicity and flexibility of design, handling of imprecise data and the capability to model nonlinear systems, among others, can be exploited. In particular, a classification task can be carried out if the information behavior is described using 'if-then' classification rules for when information about the input data is known. These rules describe the class of an object according to its features; for instance, if an object is high then its class is big.

FL systems consist of four stages: Fuzzification, rules, inference mechanism and defuzzification [5,44], as shown in Figure 1. In the fuzzification, the inputs are mapped into linguistic variables and quantified through membership functions. These functions can have Gaussian, triangular, trapezoidal or other shapes. As mentioned previously, the 'if-then' rules describe linguistically how an object has to be assigned to a specific class according to its features. These rules are set by an expert that knows the features and classes. In the inference mechanism, the decision-making process is carried out, giving a conclusion for a specific set of inputs. Finally, the conclusion is converted to understandable information for the user using the defuzzification stage. In this stage, there are several defuzzification methods, where the center-of-gravity method is one of the most popular.

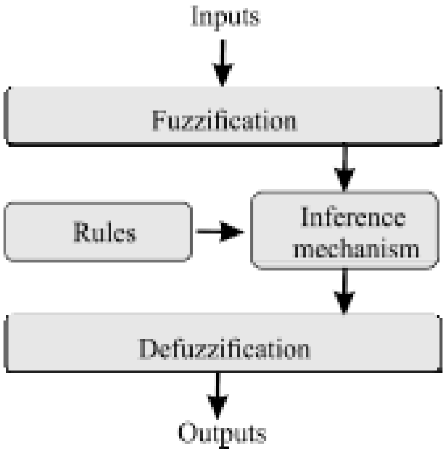

Figure 1. General diagram of a fuzzy logic (FL) system.

3. Proposed Methodology

The proposed methodology to detect SWSC faults in IMs is shown in Figure 2. In general, the methodology is divided into two stages: Design and implementation. In the design stage, the current signals of an IM, ranging from steady state to different fault severities, along with different load conditions are firstly acquired. Then, from the frequency domain analysis, and by following Equation (1), information related to the SWSC condition can be found in f_{L} ($k = 1$ and $n = 3$) and f_{R} ($k = 1$ and $n = 5$). In particular, an IM with two pairs of poles ($p = 2$) operating in an electric system where $f = 60$ Hz at no load condition (slip of $s \approx 0$) presents information related to the SWSC fault, where $f_{\mathrm{L}} = 150$ and $f_{\mathrm{R}} = 210$. In this regard, two brick-wall band-pass filters (using Equation (4)) are constructed to extract that information. Figure 3 shows their design. In Figure 3a, the region of interest in the frequency domain (f_{L} and f_{R}) can be observed. As s in the IM can shift the f_{L} and f_{R} components, the brick-wall band-pass filters consider the bandwidths denoted by ($f_{\mathrm{L\_1}}$,$f_{\mathrm{L\_2}}$) and ($f_{\mathrm{R\_1}}$,$f_{\mathrm{R\_2}}$), respectively. By considering a wide range for s according to the nominal motor speed, the values of $f_{\mathrm{L\_1}} = 160$, $f_{\mathrm{L\_2}} = 170$, $f_{\mathrm{R\_1}} = 200$, and $f_{\mathrm{R\_2}} = 210$ are used. Figure 3b shows that the band-pass filter, Ff_{L}, is designed using the difference of two brick-wall low-pass filters with $f_{\mathrm{L\_1}}$ and $f_{\mathrm{L\_2}}$ as cutoff frequencies. In a similar way, the band-pass filter, Ff_{R}, is designed using $f_{\mathrm{R\_1}}$ and $f_{\mathrm{R\_2}}$. The order of the filters is set to 1024 in order to achieve a high attenuation in the stop band. Figure 3c shows the frequency responses for the two brick-wall band-pass filters. Ff_{L} is the filter that is constructed to extract the f_{L} component and Ff_{R} is the filter that is constructed to extract the f_{R} component. Once the filters are designed, the analysis of fault indices is carried out (see Figure 2); in order to do so, the SE, energy and RMS indices (using Equations (5)–(7) are applied to the filtered signals to determine which index presents the most discriminant information in terms of the fault severity and its susceptibility to the mechanical load. When the most appropriate index to diagnose the SWSC has been obtained, a FL system is designed to automatically determine the IM condition from the information provided by the selected index. The designed FL system consists of the stages presented in Figure 1, i.e., fuzzification, rules, inference mechanism and defuzzification. As the elements that compound each stage depend on the experimental results, they are described in detail in Section 4.3.

In the implementation stage, the designed filters, Ff_{L} and Ff_{R}, are applied to the input current signal (see Figure 2). Then, the selected index is computed for each frequency component, namely $\mathrm{SE_L}$ for f_{L} and $\mathrm{SE_R}$ for f_{R}. Finally, on the one hand, the indices are averaged to provide an indicator that quantifies the fault severity, and on the other hand, the indices are analyzed by the FL system to determine the IM condition in an automatic way.

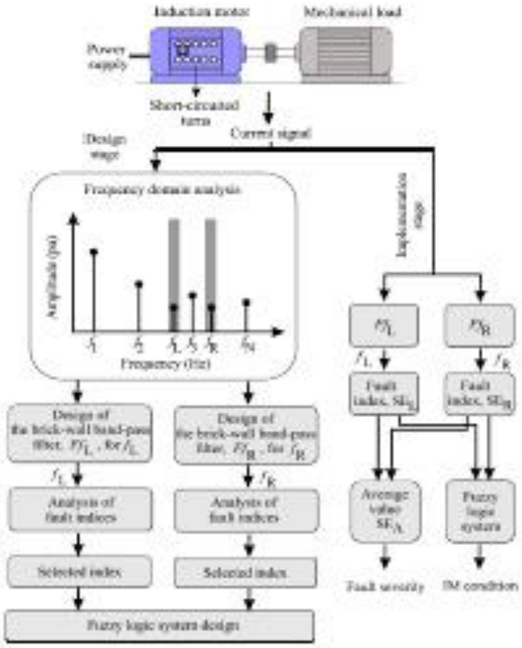

Figure 2. Proposed methodology.

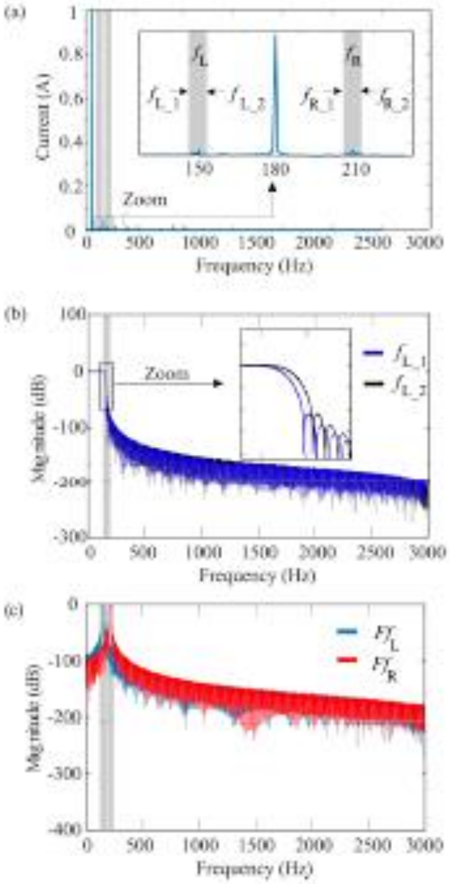

Figure 3. Filter design: (**a**) Frequencies of interest, (**b**) brick-wall low-pass filters and (**c**) brick-wall band-pass filters.

4. Experimentation and Results

4.1. Experimental Setup

In Figure 4, the experimental setup used to test and validate the proposal is depicted. In general, it consists of: A personal computer (PC) to implement the analysis using MATLAB software, an IM in which the stator-winding has been modified with several taps, a motor starter, a data acquisition system (DAS) to acquire the current signals and a dynamometer to generate the mechanical load in a controlled way. The model of the used 3-phase IM was WEG 218ET3EM145TW, featuring 2 poles, 2 hp, 220 VAC and 60 Hz. The SWSC conditions were artificially produced with the insertion of taps in phase A. The analyzed taps correspond to 10, 20, 30 and 40 short-circuited turns (SCTs). The current signal was acquired using a model i200 current clamp from Fluke, a 16-bit analog-to-digital converter model which was incorporated in the NI-USB 6211 board from National Instruments, and a sampling frequency of 6000 samples/s during a time window of 1 s. For the analysis, twenty tests for each motor condition (0, 10, 20, 30 and 40 SCTs) were carried out; therefore, 100 tests were analyzed. Regarding the mechanical load, it was provided by a four-quadrant model 8540 dynamometer from Lab-Volt, where 0.00, 2.04, 4.09 and 6.13 Nm were used as the load torques. These values ranged from no-load to nominal load.

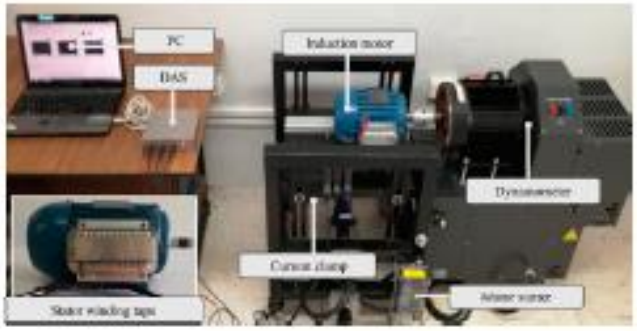

Figure 4. Experimental setup.

Figure 5 shows an example of the acquired current signals, where it was observed that the magnitude of the current signal increased with both the mechanical load and the fault severity. This is very important, as the proposed methodology has to be capable of detecting the SCTs regardless of the mechanical load. For instance, a methodology based on the magnitude of the current signal is inappropriate as the fault can be confused with an increment in the load.

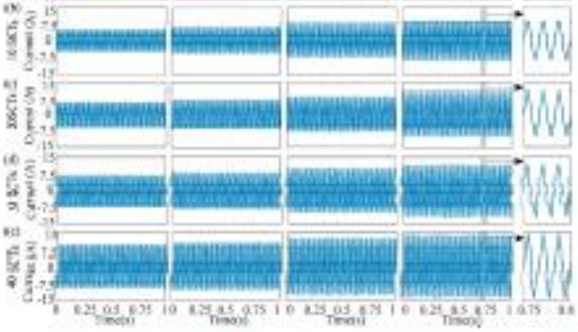

Figure 5. Current signals for (**a**) 0 SCTs, (**b**) 10 SCTs, (**c**) 20 SCTs, (**d**) 30 SCTs and (**e**) 40 SCTs at different loads (0.00, 2.04, 4.09 and 6.13 Nm).

4.2. *Results for Real Signals*

Following the proposed methodology, the current signals in steady state were filtered using Ff_{L} and Ff_{R}. After the filtering stage, the SE, RMS and energy indices were computed for the output signals given by f_{L} and f_{R} (see Figure 2). In order to have a common reference to quantify the fault severity, the results of the indices were normalized using the numerical value as a normalization factor for the healthy condition (0 SCTs); thus, these indices will have a value of 1 for 0 SCTs, indicating a healthy condition. Figure 6 depicts the obtained results for the analyzed indices. At the left side of this figure, the results for f_{L} under both different fault severities and different load conditions are shown, whereas the results for f_{R} are shown at the right side.

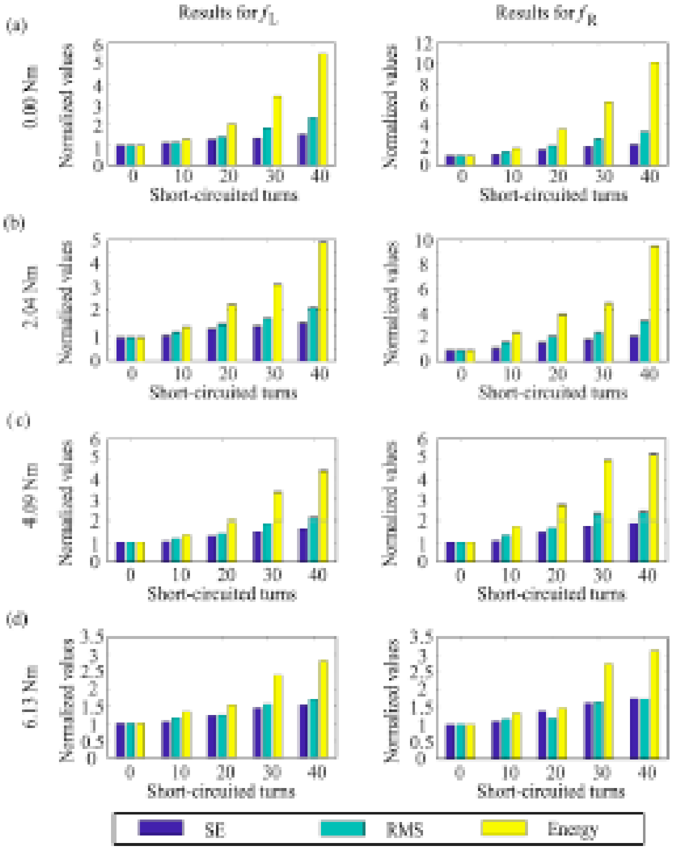

Figure 6. Results for the Shannon entropy (SE), root mean square (RMS), and energy indices at **(a)** 0.00 Nm, **(b)** 2.04 Nm, **(c)** 4.09 Nm and **(d)** 6.13 Nm (left side for f_{L} and right side for f_{R}).

The results presented in Figure 6 show that the values of the indices increased with the fault severity, which was useful for quantification purposes; however, the change rate in some indices was different for different load conditions, which can compromise the diagnosis. For instance, the energy in f_{L} for 30 SCTs under a load of 2.04 Nm was approximately 3, which can be confused with the energy in f_{L} for 40 SCTs under a load of 6.13 Nm, since it was also approximately 3. In the RMS index, a similar behavior was observed; for instance, the RMS in f_{R} for 20 SCTs under a load of 0.00 Nm was approximately 2, which can be confused with the RMS in f_{R} for 30 SCTs under a load of 4.09 Nm, since it was also approximately 2. From these observations and by analyzing the SE behavior, it was found that the SE index provides the most uniform rate of change regardless of the load conditions, making it the most appropriate index to diagnose and quantify the severity of the SWSC fault. For clarity purposes, Figure 7 shows a three-dimensional bar chart of the SE values (SE_{L} value for f_{L} and SE_{R}

value for f_R), where a behavior almost constant for different loads levels and a constant increment according to the fault severity are both observed. This behavior demonstrates that the SE index can diagnose the fault severity in a proper way, regardless of the mechanical load. In order to provide a single fault index, SE_L and SE_R were averaged, where the result, SE_A, was used as indicator for quantifying the fault severity (see Figure 7c).

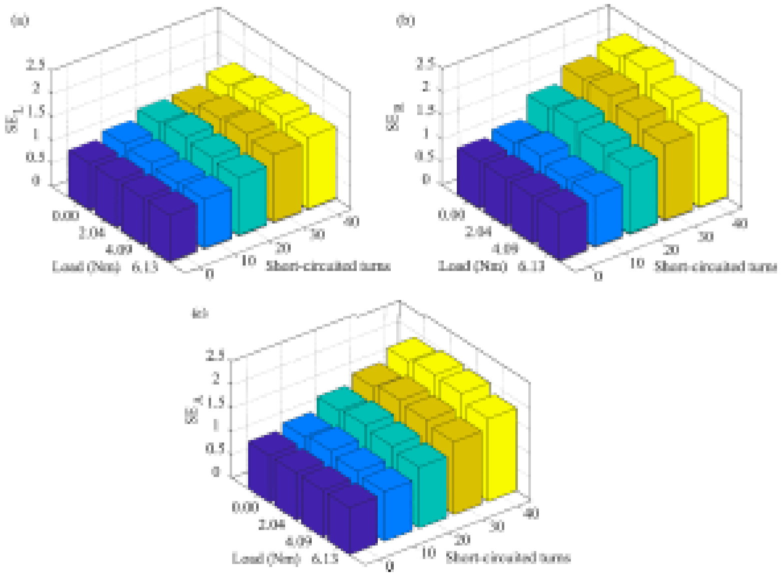

Figure 7. SE values for (**a**) f_L, (**b**) f_R, and (**c**) SE_A at both different loads and different fault severities.

Table 1 presents the mean (μ) and the standard deviation (σ) for the SE values of the twenty tests of each IM condition (0, 10, 20, 30 and 40 SCTs). Figure 8 shows the results of Table 1 as Gaussian distribution functions, where μ and σ are considered. From this figure, it is evident that, in all the cases, the higher the fault severity, the higher the index value, which applies to both SE_L and SE_R. Although the SE index allows for quantification of the fault severity, the classification of the IM condition (0, 10, 20, 30 and 40 SCTs) cannot be directly achieved, since there are small overlaps between some conditions; for instance, there is an overlap between the 0 SCTs condition (dark blue) and the 10 SCTs condition (light blue) in Figure 8a at the different loads. In this regard, a FL system with SE_L and SE_R as inputs was used to provide the automatic classification. It is important to mention that a FL system was used as classifier in this work, since the information presented in Figure 8 (Gaussian distribution functions) can be seized to generate the Gaussian membership functions.

Table 1. μ and σ for SE values.

			f_L **Number of Short-Circuited Turns (μ and σ for SE Values)**		
Load	**0**	**10**	**20**	**30**	**40**
0.00	1, 0.1229	1.1326, 0.1578	1.3051, 0.1720	1.3297, 0.1160	1.5324, 0.0699
2.04	1, 0.1097	1.0916, 0.0890	1.3673, 0.0483	1.4781, 0.0413	1.6144, 0.0533
4.09	1, 0.0516	1.0368, 0.0530	1.3025, 0.0395	1.5279, 0.0335	1.6354, 0.0359
6.13	1, 0.0558	1.0589, 0.0771	1.2410, 0.0613	1.4507, 0.0477	1.5444, 0.0591
			f_R **Number of Short-Circuited Turns (μ and σ for SE Values)**		
Load	**0**	**10**	**20**	**30**	**40**
0.00	1, 0.1082	1.1082, 0.1121	1.5639, 0.0951	1.8904, 0.0696	2.0860, 0.0830
2.04	1, 0.1614	1.2044, 0.1315	1.6318, 0.1035	1.9104, 0.0647	2.1743, 0.0580
4.09	1, 0.1204	1.0683, 0.1135	1.5052, 0.1166	1.7788, 0.0960	1.9281, 0.0727
6.13	0.073833	1.0878, 0.0720	1.3794, 0.0838	1.6181, 0.0786	1.7425, 0.0932

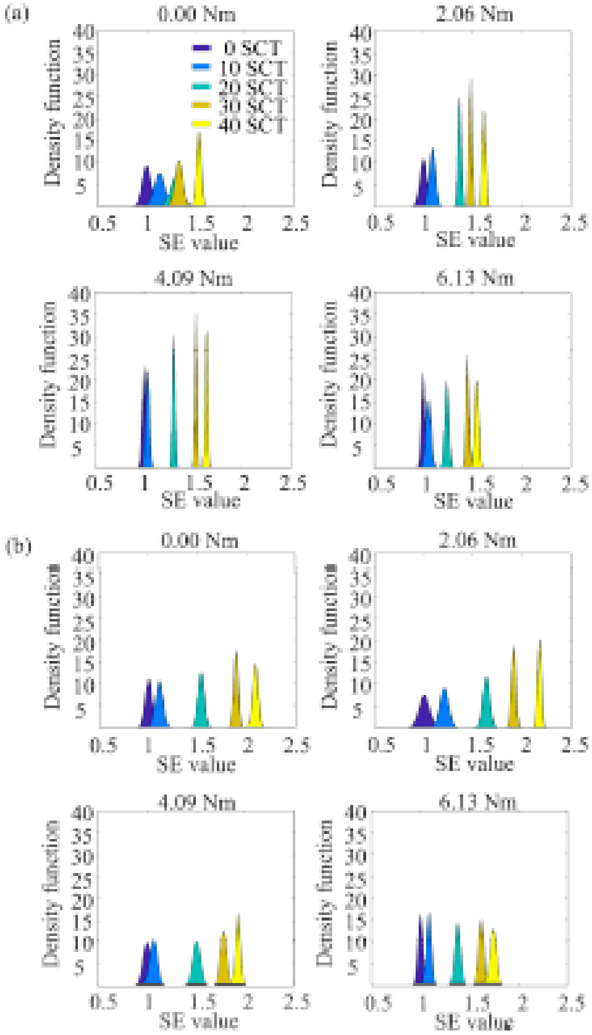

Figure 8. Gaussian distribution functions for (**a**) SE_L and (**b**) SE_R at both different loads and different fault severities.

4.3. *Fuzzy Logic System Results*

The proposed FL system is a Mamdani-type fuzzy inference system with two inputs, one output and 25 rules. As mentioned previously, the inputs were SE_L and SE_R, while the output was the IM condition. For the fuzzification stage, both inputs were portioned into five Gaussian membership functions, as shown in Figure 9a. These functions were labeled as follows: Very small value (VSV), small value (SV), normal value (NV), high value (HV) and very high value (VHV). The crisp output of the proposed FL system assumes values between 0.5 and 5.5, as shown in Figure 9b; in this figure, 0 SCTs are 1, 10 SCTs are 2, 20 SCTs are 3, 30 SCTs are 4 and 40 SCTs are 5. On the other hand, the 25 functions are presented in Table 2, where one rule can be read as follows: If SE_L is VSV and SE_R is VSV, then the IM condition is 0 SCTs. The minimum composition was used for quantifying the output of the rules and the center-of-gravity method was used for defuzzification [44]. Table 3 shows the classification results for the performed tests. As can be observed, most cases present an effectiveness of 100%; however, two cases present an effectiveness of 95%, implying a general effectiveness of 98%. These cases correspond to 0 SCTs and 10 SCTs. This result can be somehow expected, since the existing overlaps in the Gaussian distribution functions shown in Figure 8 indicate that, in probabilistic terms, there is not a complete separation between cases.

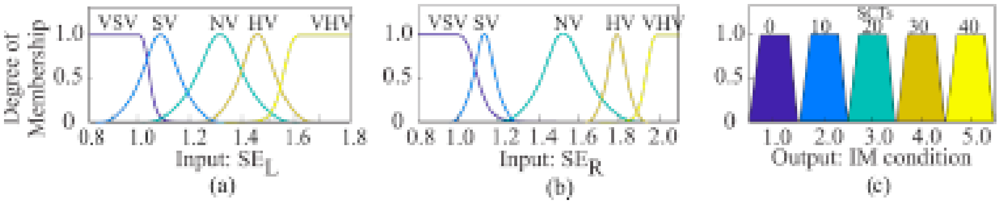

Figure 9. Membership functions for (a) SE_L and (b) SE_R and (c) FL outputs.

Table 2. Rules for the proposed FL system.

Inputs			**SE_R**		
SE_L	**VSV**	**SV**	**NV**	**HV**	**VHV**
VSV	0 SCTs	0 SCTs	10 SCTs	20 SCTs	20 SCTs
SV	0 SCTs	10 SCTs	20 SCTs	20 SCTs	20 SCTs
NV	10 SCTs	20 SCTs	20 SCTs	20 SCTs	30 SCTs
HV	20 SCTs	20 SCTs	20 SCTs	30 SCTs	40 SCTs
VHV	20 SCTs	20 SCTs	30 SCTs	40 SCTs	40 SCTs

Table 3. Classification results (confusion matrix).

IM Condition	**0 SCTs**	**10 SCTs**	**20 SCTs**	**30 SCTs**	**40 SCTs**	**EP (%)**
0 SCTs	19	1	0	0	0	95
10 SCTs	1	19	0	0	0	95
20 SCTs	0	0	20	0	0	100
30 SCTs	0	0	0	20	0	100
40 SCTs	0	0	0	0	20	100
					Effectiveness	98%

EP: Effectiveness percentage.

4.4. *Discussion*

Table 4 summarizes a comparison between the proposal and other recent methodologies presented in the literature, where the methods or algorithms applied to diagnose the SWSC fault in the IM and the features or operating conditions that are considered in the experimentation are shown.

From Table 4, it can be observed that the proposed methodology presents an effectiveness percentage of 98% for detecting the SWSC fault, considering both different severity levels (10, 20, 30 and 40 short-circuited turns) and different mechanical load levels (0%, 33%, 66% and 100%), unlike other works reviewed in the literature [12,19,24], which present mainly the analysis of either a level of damage and different operating conditions or different levels of damage and a constant load operating condition.

In the proposal, the obtained effectiveness (98%) is mainly due to the SE index, which allows for both quantifying the severity of damage regardless of the torque load applied to the IM and classifying the SWSC fault using the proposed FL system for an automatic diagnosis. In qualitative terms, it is important to mention that a low computational burden is achieved by the proposal, since a space transformation of the measured signal is not required, allowing for a low complexity implementation, unlike the other introduced proposals, where a signal transformation and several nonlinear indices is required, along with an expert to interpret the obtained results [12,19,23]. It should be pointed out that the expert role is to interpret the results obtained by the analysis of several characteristics, such as: The location of peaks, the spectrum, among other characteristics; in this regard, the aforementioned analyses are performed qualitatively. Yet, the automatic detection of the motor condition can drastically reduce time taken and allow for continuous and online monitoring. In Reference [8], similar features and operating conditions with the proposal can be observed; however, results about the fault indictor as an independent parameter of the mechanical load are not presented. On the contrary, the proposed

SE index demonstrates to be an efficient and insensitive fault indicator to the mechanical load, allowing for consistent diagnosis in different industry applications.

Table 4. Comparison summary between the proposed methodology and works reporting stator winding short-circuit (SWSC) fault diagnosis.

Work	Applied Methods	Domain	Accuracy	Variable Load	Different Fault Severities
[8]	1. Compute the mutual information among current signals. 2. Normalize data. 3. Pattern recognition by means of artificial neural networks (ANN).	Time	>93%	Yes	Yes
[12]	1. Estimate Zero crossing time (ZCT). 2. Compute frequency spectrum of ZCT signal by means of discrete Fourier transform. 3. Locate peaks related to inter-turn fault.	Frequency	NR	Yes	No
[19]	1. Decompose current signal using stationary Wavelet transform (SWT). 2. Obtain fault residues using reconstructed currents. 3. Obtain coefficients by decomposing the residues with discrete Wavelet transform (DWT). 4. Estimate the fault index and compare with an adaptive threshold.	Time-Frequency	NR	No	Yes
[23]	1. Obtain an analytical signal by means of extended Park's vector approach and Hilbert transform (P-H). 2. Estimate frequency domain of the analytical signal via fast Fourier transform (FFT). 3. Calculate the amplitudes and frequencies corresponding to harmonics associated with the fault. 4. Compute the partial relative indexes (PRI) for fault detection.	Frequency	NR	Yes	Yes
[24]	1. Map into the α-β stator-fixed reference frame the stator currents. 2. Compute the instantaneous space phasor (ISP) module. 3. Evaluate the final prediction criterion (FPE) for the proposed ISP autoregressive model by the different operation condition.	Time	95%	No	Yes
This work	1. Brick-wall band-pass FIR filters for extraction of frequency components. 2. Compute the SE index as fault indicator. 3. FL system for automatic classification	Time	98%	Yes	Yes

5. Conclusions

Winding faults are one of the most common faults in IM. In this work, a new method based on filters, fault indices and a FL system for the assessment of SWSC faults in IMs was presented. The SE, RMS and energy indices were tested. These indices evaluated the information that was extracted by the brick-wall band-pass filters from the steady-state current signal. Our results indicated that the SE was the most suitable index for the assessment of SWSC faults. For the analyzed cases, i.e., 10, 20, 30 and 40 SCTs under different load torque conditions (0, 2.04, 4.09 and 6.13 Nm), this index has been demonstrated to be sensitive to fault severity and insensitive to mechanical load, i.e., the SE index can properly assess the fault severity regardless of the mechanical load, which is very important, as the mechanical load can change or be different for different industrial applications. On the other hand, the proposed FL system uses the SE values to classify the IM condition in an automatic way. The obtained results indicate that the proposed FL system provides a general effectiveness of 98%.

In a future work, the proposal will be tested under an unbalanced power supply voltage condition (a common electrical condition in industry) in order to increase its robustness and applicability. Furthermore, as the proposal is based on low complexity algorithms (filters and indices based on time-domain formulas), it may be implemented into an embedded system in order to provide an online condition monitoring system. On the other hand, it is important to mention that at this stage of research, the proposal is focused on the diagnosis of SWSC faults in steady state conditions; however, adaptive filters and time-frequency techniques will be also explored in order to provide a solution for transient operating conditions.

Author Contributions: Conceptualization, A.M.-B. and M.V.-R.; Data curation and formal analysis, A.M.-B; Funding acquisition, J.J.d.S.-P., D.G.-L. and J.P.A.-S.; Methodology, A.M.-B. and M.V.-R.; Investigation, Resources and Visualization, J.J.d.S.-P., D.G.-L. and J.P.A.-S.; Writing—original draft, review & editing, all the Authors.

Funding: This research was funded by the "Consejo Nacional de Ciencia y Tecnologia (CONACYT)" under the scholarship 296868.

Conflicts of Interest: The authors declare no conflict of interest.

References

1. Glowacz, A. Acoustic-based fault diagnosis of commutator motor. *Electronics* **2018**, *7*, 299. [CrossRef]
2. Singh, A.; Grant, B.; DeFour, R.; Sharma, C.; Bahadoorsingh, S. A review of induction motor fault modeling. *Electr. Power Syst. Res.* **2016**, *133*, 191–197. [CrossRef]
3. Mrizalde, Y.; Hernandez-Callejo, L.; Duque-Perez, O. State of the art and trends in the monitoring, detection and diagnosis of failures in electric induction motors. *Energies* **2017**, *10*, 1056. [CrossRef]
4. Rangari, S.; Suryawanshi, H.; Renge, M. New fault-tolerant control strategy of five-phase induction motor with four-phase and three-phase modes of operation. *Electronics* **2018**, *7*, 159. [CrossRef]
5. Amezquita-Sanchez, J.P.; Valtierra-Rodriguez, M.; Perez-Ramirez, C.A.; Camarena-Martinez, D.; Garcia-Perez, A.; Romero-Troncoso, R.J. Fractal dimension and fuzzy logic systems for broken rotor bar detection in induction motors at start-up and steady-state regimes. *Meas. Sci. Technol.* **2017**, *28*, 075001. [CrossRef]
6. Gyftakis, K.N.; Spyropoulos, D.V.; Kappatou, J.C.; Mitronikas, E.D. A novel approach for broken bar fault diagnosis in induction motors through torque monitoring. *IEEE Trans. Energy Convers.* **2013**, *28*, 267–277. [CrossRef]
7. Florkowski, M.; Furgal, J. Detection of winding faults in electrical machines using the frequency response analysis method. *Meas. Sci. Technol.* **2004**, *15*, 2067. [CrossRef]
8. Bazan, G.H.; Scalassara, P.R.; Endo, W.; Goedtel, A.; Godoy, W.F.; Palácios, R.H.C. Stator fault analysis of three-phase induction motors using information measures and artificial neural networks. *Electr. Power Syst. Res.* **2017**, *143*, 347–356. [CrossRef]
9. Thomson, W.T.; Fenger, M. Current signature analysis to detect induction motor faults. *IEEE Ind. Appl. Mag.* **2001**, *7*, 26–34. [CrossRef]
10. Arthur, N.; Penman, J. Induction machine condition monitoring with higher order spectra. *IEEE Trans. Ind. Electron.* **2000**, *47*, 1031–1041. [CrossRef]
11. Ballal, M.S.; Khan, Z.J.; Suryawanshi, H.M.; Sonolikar, R.L. Adaptive neural fuzzy inference system for the detection of inter-turn insulation and bearing wear faults in induction motor. *IEEE Trans. Ind. Electron.* **2007**, *54*, 250–258. [CrossRef]
12. Ukil, A.; Chen, S.; Andenna, A. Detection of stator short circuit faults in three-phase induction motors using motor current zero crossing instants. *Electr. Power Syst. Res.* **2011**, *81*, 1036–1044. [CrossRef]
13. Drif, M.H.; Cardoso, A.J.M. Stator fault diagnostics in squirrel cage three-phase induction motor drives using the instantaneous active and reactive power signature analyses. *IEEE Trans. Ind. Inform.* **2014**, *10*, 1348–1360. [CrossRef]
14. Glowacz, A.; Glowacz, W.; Glowacz, Z.; Kozik, J. Early fault diagnosis of bearing and stator faults of the single-phase induction motor using acoustic signals. *Measurement* **2018**, *113*, 1–9. [CrossRef]

15. Thomson, W.T. On-line MCSA to diagnose shorted turns in low voltage stator windings of 3-phase induction motors prior to failure. In Proceedings of the Electric Machines and Drives Conference (IEMDC 2001), Cambridge, MA, USA, 17–20 June 2001; pp. 891–898.
16. Bouzid, M.B.K.; Champenois, G. New expressions of symmetrical components of the induction motor under stator faults. *IEEE Trans. Ind. Electron.* **2013**, *60*, 4093–4102. [CrossRef]
17. Surya, G.N.; Khan, Z.J.; Ballal, M.S.; Suryawanshi, H.M. A simplified frequency-domain detection of stator turn fault in squirrel-cage induction motors using an observer coil technique. *IEEE Trans. Ind. Electron.* **2017**, *64*, 1495–1506. [CrossRef]
18. Asfani, D.A.; Muhammad, A.K.; Purnomo, M.H.; Hiyama, T. Temporary short circuit detection in induction motor winding using combination of wavelet transform and neural network. *Expert Syst. Appl.* **2012**, *39*, 5367–5375. [CrossRef]
19. Devi, N.R.; Sarma, D.V.S.; Rao, P.V.R. Detection of stator incipient faults and identification of faulty phase in three-phase induction motor–simulation and experimental verification. *IET Electr. Power Appl.* **2015**, *9*, 540–548. [CrossRef]
20. Lee, S.H.; Kim, S.; Kim, J.M.; Choi, C.; Kim, J.; Lee, S.; Oh, Y. Extraction of induction motor fault characteristics in frequency domain and fuzzy entropy. In Proceedings of the IEEE International Conference on Electric Machines and Drives, San Antonio, TX, USA, 15 May 2005; pp. 35–40.
21. Li, J.; Yu, H.; Zhang, L. Application of ensemble empirical mode decomposition on stator inter-turn short-circuit fault in doubly fed induction generators. In Proceedings of the Second International Conference on Mechatronics and Automatic Control, Beijing, China, 20–21 September 2014; pp. 73–83.
22. Rosero, J.A.; Romeral, L.; Ortega, J.A.; Rosero, E. Short-circuit detection by means of empirical mode decomposition and Wigner–Ville distribution for PMSM running under dynamic condition. *IEEE Trans. Ind. Electron.* **2015**, *56*, 4534–4547. [CrossRef]
23. Sahraoui, M.; Ghoggal, A.; Guedidi, S.; Zouzou, S.E. Detection of inter-turn short-circuit in induction motors using Park–Hilbert method. *Int. J. Syst. Assur. Eng. Manag.* **2014**, *5*, 337–351. [CrossRef]
24. Garcia-Guevara, F.M.; Villalobos-Piña, F.J.; Alvarez-Salas, R.; Cabal-Yepez, E.; Gonzalez-Garcia, M.A. Stator fault detection in induction motors by autoregressive modeling. *Math. Probl. Eng.* **2016**, *2016*, 1–7. [CrossRef]
25. Ghate, V.N.; Dudul, S.V. Optimal MLP neural network classifier for fault detection of three phase induction motor. *Expert Syst. Appl.* **2010**, *37*, 3468–3481. [CrossRef]
26. Valtierra-Rodriguez, M.; Granados-Lieberman, D.; Torres-Fernandez, J.E.; Rodriguez-Rodriguez, J.R.; Gómez-Aguilar, J.F. A new methodology for tracking and instantaneous characterization of voltage variations. *IEEE Trans. Instrum. Meas.* **2016**, *65*, 1596–1604. [CrossRef]
27. Antonino-Daviu, J.A.; Riera-Guasp, M.; Pineda-Sanchez, M.; Pérez, R.B. A critical comparison between DWT and Hilbert–Huang-based methods for the diagnosis of rotor bar failures in induction machines. *IEEE Trans. Ind. Appl.* **2009**, *45*, 1794–1803. [CrossRef]
28. Torres, M.E.; Colominas, M.A.; Schlotthauer, G.; Flandrin, P. A complete ensemble empirical mode decomposition with adaptive noise. In Proceedings of the IEEE International Conference on Acoustics, Speech and Signal Processing (ICASSP 2011), Prague, Czech Republic, 22–27 May 2011; pp. 4144–4147.
29. Elbouchikhi, E.; Choqueuse, V.; Amirat, Y.; Benbouzid, M.E.H.; Turri, S. An efficient Hilbert–Huang transform-based bearing faults detection in induction machines. *IEEE Trans. Energy Convers.* **2017**, *32*, 401–413. [CrossRef]
30. Boashash, B.; Khan, N.A.; Ben-Jabeur, T. Time–frequency features for pattern recognition using high-resolution TFDs: A tutorial review. *Digit. Signal Process.* **2015**, *40*, 1–30. [CrossRef]
31. Adeli, H.; Jiang, X. Dynamic fuzzy wavelet neural network model for structural system identification. *J. Struct. Eng.* **2006**, *132*, 102–111. [CrossRef]
32. Amezquita-Sanchez, J.P.; Adeli, H. Synchrosqueezed wavelet transform-fractality model for locating, detecting, and quantifying damage in smart highrise building structures. *Smart Mater. Struct.* **2015**, *24*, 065034. [CrossRef]
33. Jung, J.H.; Lee, J.J.; Kwon, B.H. Online diagnosis of induction motors using MCSA. *IEEE Trans. Ind. Electron.* **2006**, *53*, 1842–1852. [CrossRef]
34. Roscoe, A.J.; Abdulhadi, I.F.; Burt, G.M. Filters for M class phasor measurement units. In Proceedings of the IEEE International Workshop on Applied Measurements for Power Systems (AMPS 2012), Aachen, Germany, 26–28 September 2012; pp. 1–6.

35. Ramstad, T. Digital methods for conversion between arbitrary sampling frequencies. *IEEE Trans. Acoust. Speech Signal Process.* **1984**, *32*, 577–591. [CrossRef]
36. Cabal-Yepez, E.; Valtierra-Rodriguez, M.; Romero-Troncoso, R.J.; Garcia-Perez, A.; Osornio-Rios, R.A.; Miranda-Vidales, H.; Alvarez-Salas, R. FPGA-based entropy neural processor for online detection of multiple combined faults on induction motors. *Mech. Syst. Signal Process.* **2012**, *30*, 123–130. [CrossRef]
37. Mejia-Barron, A.; Valtierra-Rodriguez, M.; Granados-Lieberman, D.; Olivares-Galvan, J.C.; Escarela-Perez, R. The application of EMD-based methods for diagnosis of winding faults in a transformer using transient and steady state currents. *Measurement* **2018**, *117*, 371–379. [CrossRef]
38. Bafroui, H.H.; Ohadi, A. Application of wavelet energy and Shannon entropy for feature extraction in gearbox fault detection under varying speed conditions. *Neurocomputing* **2014**, *133*, 437–445. [CrossRef]
39. Seryasat, O.R.; Honarvar, F.; Rahmani, A. Multi-fault diagnosis of ball bearing using FFT, wavelet energy entropy mean and root mean square (RMS). In Proceedings of the IEEE International Conference on Systems Man and Cybernetics (SMC 2010), Istanbul, Turkey, 10–13 October 2010; pp. 4295–4299.
40. Kamalapathi, K.; Priyadarshi, N.; Padmanaban, S.; Holm-Nielsen, J.; Azam, F.; Umayal, C.; Ramachandaramurthy, V. A hybrid moth-flame fuzzy logic controller based integrated cuk converter fed brushless DC motor for power factor correction. *Electronics* **2018**, *7*, 288. [CrossRef]
41. Fink, A.; Töpfer, S.; Isermann, R. Nonlinear model-based control with local linear neuro-fuzzy models. *Arch. Appl. Mech.* **2003**, *72*, 911–922. [CrossRef]
42. Nentwig, M.; Mercorelli, P. Throttle valve control using an inverse local linear model tree based on a Fuzzy neural network. In Proceedings of the 7th IEEE International Conference on Cybernetic Intelligent Systems, London, UK, 9–10 September 2008. [CrossRef]
43. De Silva, C.W. *Intelligent Control: Fuzzy Logic Applications*; CRC Press: Boca Raton, FL, USA, 2018.
44. Passino, K.M.; Yurkovich, S.; Reinfrank, M. *Fuzzy Control*; Addison-Wesley: Menlo Park, CA, USA, 1998; ISBN 0-201-18074-X.

Anexo D

electronics

MDPI

Article

Harmonic PMU Algorithm Based on Complex Filters and Instantaneous Single-Sideband Modulation

Arturo Mejia-Barron [1], David Granados-Lieberman [2], Jose R. Razo-Hernandez [1], Juan P. Amezquita-Sanchez [1] and Martin Valtierra-Rodriguez [1,*]

[1] ENAP-Research Group, CA-Sistemas Dinámicos, Facultad de Ingeniería, Universidad Autónoma de Querétaro (UAQ), Campus San Juan del Río, Río Moctezuma 249, Col. San Cayetano, San Juan del Río, Qro. C. P. 76807, Mexico; arturo.mejia@enap-rg.org (A.M.-B.); roberto.razo@enap-rg.org (J.R.R.-H); juan.amezquita@enap-rg.org (J.P.A.-S.)

[2] ENAP-Research Group, CA-Fuentes Alternas y Calidad de la Energía Eléctrica, Departamento de Ingeniería Electromecánica, Instituto Tecnológico Superior de Irapuato (ITESI), Carr. Irapuato-Silao km 12.5, Colonia El Copal, Irapuato, Guanajuato C. P. 36821, Mexico; david.granados@enap-rg.org

* Correspondence: martin.valtierra@uaq.mx

Received: 30 December 2018; Accepted: 28 January 2019; Published: 29 January 2019

Abstract: Phasor measurement units (PMUs) have become powerful monitoring tools for many applications in smart grids. In order to address the different issues related to harmonics in power systems, the fundamental phasor estimator in a PMU has been extended to the harmonic phasor estimator by several researchers around the world. Yet, the development of harmonic phasor estimators is a challenge because they have to consider time-varying frequencies since the frequency deviation in the harmonic components is proportional to the harmonic order in a dynamic way. In this work, a new algorithm for harmonic phasor estimation using an instantaneous single-sideband (SSB) modulation is presented. Unlike other SSB-based approaches, its implementation in this work is based on concepts of instantaneous phase and instantaneous frequency. In general, the proposed algorithm is divided into two stages. Firstly, the estimation of the fundamental phasor is carried out by means of a complex finite impulse response (FIR) filter which provides the analytic signal used to compute the instantaneous magnitude, phase, and frequency. Secondly, a complex FIR filter bank is proposed for the estimation of the harmonic components, where the instantaneous SSB modulation technique is applied in order to center the harmonic components into specific narrow bands for each complex filter when an off-nominal frequency occurs. The validation of the proposed algorithm is carried out by means of the current standards of phasor measurement units, i.e., Std. C37.118.1-2011 and C37.118.1a-2014, which involve steady-state, dynamic, and time performance tests.

Keywords: complex FIR filters; harmonic phasor; IEEE Standard C37.118.1; instantaneous phase and frequency; instantaneous single-sideband modulation; phasor measurement unit (PMU)

1. Introduction

Proliferation of non-linear loads along with the growth of distributed generation systems are some of the main causes of power quality problems related to harmonic pollution in modern power systems [1]. This pollution compromises the system reliability, e.g., producing additional losses in transmission or distribution lines, overheating of electrical machines and relays breakdowns [2,3]. At the same time, the development of new power system topics, such as smart grids and renewable energies, increases the requirements of methodologies for power quality monitoring [4–7], including the analysis of both the fundamental component and the harmonic components [8]. Regarding the fundamental component, phasor measurement units (PMUs) are synchronized remote devices commonly used for wide area monitoring systems with high performance requirements for phasor, frequency and rate of change of frequency (ROCOF) errors defined in the current standard, i.e., the IEEE Std. C37.118.1-2011 and -2014 [9–11]. Although PMU standards are set originally for fundamental component measurements according to the required performance: P class or M class, their benchmark tests and requirements can be extended to harmonic components for validation purposes [9]. Therefore, a PMU with capabilities for harmonic estimation will allow improving the performance in different applications of power systems such as power quality monitoring, adaptive protections, network reconfiguration under fault conditions, and so on [12].

In literature, different algorithms for estimation of both fundamental phasor and harmonic phasor have been reported. Among the algorithms for the former [13–15], the Fourier transform (FT) has been widely used; however, it presents some drawbacks that compromise its performance, e.g., the assumption of periodic signals, spectral leakage produced when the fundamental frequency fluctuates, and that the frequency resolution depends on the time observation window [16,17]. Regarding the harmonic synchrophasor implementations, few strategies have been presented. For instance, in [2,12], the FT and a zero-crossing technique is used to calculate the fundamental and harmonic components, in which unreliable results can be obtained when a frequency fluctuation appears. In [18], an improved FT version is presented where several windows to reduce the spectral leakage are compared; besides that, it uses a curve fitting approach with fundamental frequency information for estimation of the harmonic phasors. Another work that follows the synchrophasors guidelines is carried out in [19], which proposes an estimator in off-nominal frequency conditions based on a frequency tracking process and a harmonic model, solving the model by means of a singular value decomposition method. Similarly, in [20], a recursive-least-squares technique synchronized by a phase-locked loop (PLL) is proposed. Also, harmonic dynamic models have been proposed and solved using approaches based on Taylor and Kalman filters (KF) [21,22] and a rotational invariance technique [23]. Further, in [9], both the KF and a FIR filter with adaptive filter coefficients as a function of the fundamental frequency for harmonic phasor estimation are presented. From these works, it is evident that the concept of harmonic synchrophasor has been investigated with special attention in the fundamental frequency since, on the one hand, it is used for the harmonic phasor estimations and, on the other hand, it is related to the accuracy of the results [18]. However, these works are leaving out important parameters such as the frequency error (FE) and the rate of change of frequency error (RFE) along with the benchmark tests required in the current synchrophasor standards, which can be taken as reference in order to validate in a more complete way the performance of a harmonic PMU.

In this paper, a new algorithm for phasor estimation of harmonic components in a PMU context is proposed. This algorithm is based on a complex brick-wall band-pass FIR filter for the estimation of both the fundamental phasor and the fundamental frequency. The harmonic phasors are estimated using a complex FIR filter bank by centering the harmonic components of the signal according to its frequency deviation by means of an instantaneous single-sideband (SSB) modulation technique. This technique allows shifting the spectral content of the signal using a Hilbert filter and a complex modulation process using the instantaneous frequency deviation. In this regard, the proposed algorithm represents a new scheme for harmonic estimation in a PMU context with a low-complex technique. The proposed algorithm is evaluated under all the steady-state and dynamic conditions established in the IEEE Std. C37.118.1-2011 [10] along with its amendment C37.118.1a-2014 [11]. These conditions are amplitude, phase and frequency variations, total harmonic distortion (THD), out-of-band interference, amplitude and phase modulations, frequency ramp, amplitude and phase steps. Besides that, unlike other proposals, even and odd harmonic components are analyzed for each condition. Then, the total vector error (TVE), FE, and RFE parameters, which are extended to the harmonic components, are analyzed according to the allowable limits for the M class. This class is chosen since the proposal is oriented to applications that require higher levels of accuracy and has to satisfy the out-of-band interference test which is one of the most challenging tests. The results show the feasibility of the proposed method for harmonic synchrophasor applications, where a complete fulfillment of the benchmark tests is obtained.

2. Theoretical Background

2.1. Harmonic Phasor Model

PMUs provide a synchronized magnitude and phase estimation under a coordinated universal time (UTC) of an electric signal [24,25]. This signal is determined by:

$$x(t) = \frac{A}{\sqrt{2}} \cos(2\pi f_0 t + 2\pi \int \Delta f dt + \phi) \tag{1}$$

where A is the amplitude, f_0 is the nominal system frequency (50 Hz/60 Hz), Δf is the frequency deviation, and ϕ is the phase angle. From (1), the synchrophasor representation is defined as [10]:

$$X(t) = \frac{A}{\sqrt{2}} e^{2\pi \int \Delta f dt + \phi} \tag{2}$$

In the same way, a sinusoidal signal with harmonic content can be expressed as:

$$x(t) = \sum_{h=1}^{H} \frac{A_h}{\sqrt{2}} \cos(h(2\pi f_0 t + 2\pi \int \Delta f dt) + \phi_h) \tag{3}$$

where h is the h-th component of the sinusoidal signal and H is the number of harmonics; then, the synchrophasor representation for fundamental and harmonic components is defined by:

$$X(t)_h = \frac{A_h}{\sqrt{2}} e^{2\pi h \int \Delta f dt + \phi_h} \tag{4}$$

One of the major challenges to estimate the harmonic phasors in (4) appears when the analyzed signal presents off nominal frequencies since the frequency deviation for the harmonic components increases linearly with the harmonic order h, e.g., a frequency deviation of 1 Hz in the fundamental component produces a 2 Hz frequency deviation for the 2nd harmonic, 3 Hz for the 3rd harmonic, and so on.

2.2. Single Sideband Modulation

SSB modulation is an efficient amplitude modulation technique commonly used in radio communications. Yet, this technique is also employed in signal processing, whose purpose is to shift frequency components using a carrier frequency [26,27]. This modulation is based on an analytic signal. In this regard, the modulated signal $x(t)_{SSB}$ by a frequency shift f_c is expressed by:

$$x(t)_{SSB} = x(t)\cos(2\pi f_c t) - \hat{x}(t)\sin(2\pi f_c t) \tag{5}$$

where $x(t)$ is the non-modulated signal and $\hat{x}(t)$ is the component in quadrature of $x(t)$. This formulation is normally used as a time-invariant frequency signal [27] and, in some cases, with windows of fixed length.

2.3. Complex FIR Filters

The concept of complex band-pass FIR filters for harmonic phasor estimators has been studied to obtain an analytic signal with real and imaginary parts [9]. Although good dynamic performance can be achieved, the scheme presented in [9] requires additional frequency tracking methods to adapt the filter coefficients when off nominal frequencies are presented, increasing somehow the algorithm complexity. Unlike that work, in this work, the proposal is based on adapting the input signal when a frequency deviation occurs.

Among the FIR filters, brick-wall filters are idealized filters with rectangular frequency response and an abrupt transition during the cutoff frequencies, which allows a high rejection to harmonic and inter-harmonic interference [28]. In practice, the coefficients for a band-pass filter are obtained as the difference of two low-pass filters as follows:

$$h(t)_{\mathrm{BP}} = h(t)_u - h(t)_l \tag{6}$$

where $h(t)_u$ and $h(t)_l$ are the low-pass filters with upper and lower cutoff frequencies, respectively.

The brick-wall low-pass filter coefficients are estimated using a *sinc* function as follows:

$$h(t) = w(t)\frac{\omega_p}{2}\frac{\sin \omega_p t}{\omega_p t} \tag{7}$$

where ω_p is the reference frequency and $w(t)$ is a window function; in this case, the window is a hamming window. The complex FIR filters are constructed by means of two quadrature filters ($h(t)_{\mathrm{BP}\_real}$ and $h(t)_{\mathrm{BP}\_imaginary}$) with the same attenuation behavior but with a $\pi/2$ phase shift; therefore, the analytic signal with two components is obtained through these filters for phasor estimation purposes.

3. Proposed Methodology

The proposed methodology for phasor estimation is depicted in Figure 1. The first stage consists of the estimation of both the fundamental component phasor and its frequency, where the amplitude and phase are computed by means of the analytic signal ($x(t)_r$ + i$x(t)_i$ [27]) obtained through the proposed complex FIR filter. This filter is designed from the frequency response of a reference band-pass filter as shown in Figure 2a. The reference filter given by Equation (6) represents the real filter, $h(t)_r$. Then, from the real filter frequency response, a phase shift of $\pi/2$ is introduced by multiplying the real filter frequency response by $-j$ in order to have the frequency response in quadrature. From this response, the weighted least square (WLS) algorithm is used to obtain the coefficients of the imaginary FIR filter by means of a fitting stage for the shifted frequency response. In order to improve the fit in the passband, a weight function for the fit based on both a rectangular pulse in the passband and a set of small Gaussian functions in the valleys of the frequency response are proposed, obtaining the imaginary filter (a filter in quadrature with the real filter). As a result, two brick-wall band-pass FIR filters (real: $h(t)_{\mathrm{BP}\_real}$ and imaginary: $h(t)_{\mathrm{BP}\_imaginary}$) are obtained. These proposed steps to design the filter are needed since the filter performance has to satisfy the IEEE Std. C37.118.1 requirements.

For the estimation of the fundamental phasor, a brick-wall filter with a passband of 53 Hz to 67 Hz with a filter order of 1024 (similar to the filter of 10 cycles presented at the Std.) is carefully selected to obtain an attenuation greater than 50 dB for frequencies out of the Nyquist frequency given by the reporting rate in frames per second $(FPS)/2$. In the same way, complex brick-wall FIR filters for harmonic components with both a passband of ±15 Hz around the nominal harmonic component and a filter order of 768 are designed. The amplitude frequency responses for the proposed filter bank are shown in Figure 2b. As can be notice, a lower order is proposed for the harmonic filters in order to reduce the latency since the next stage, i.e., the SSB modulation, also produces a latency.

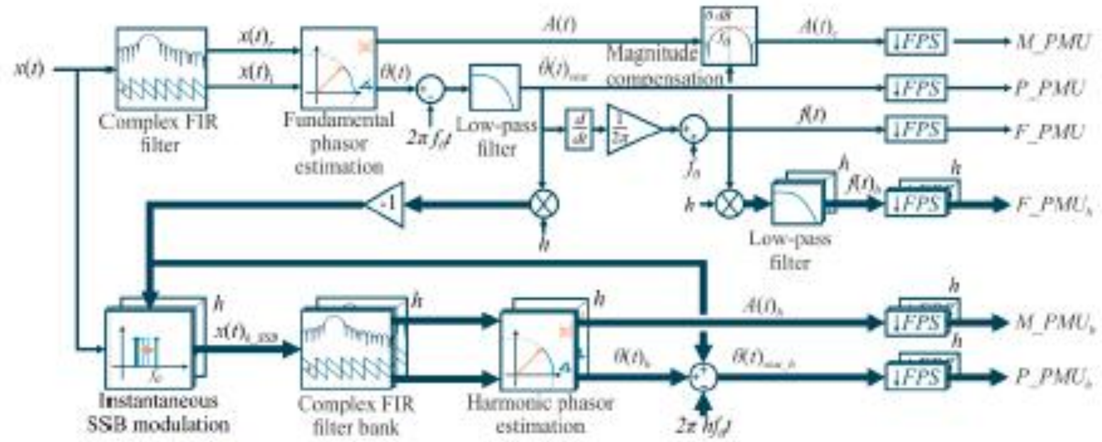

Figure 1. Proposed methodology for estimation of harmonic phasors.

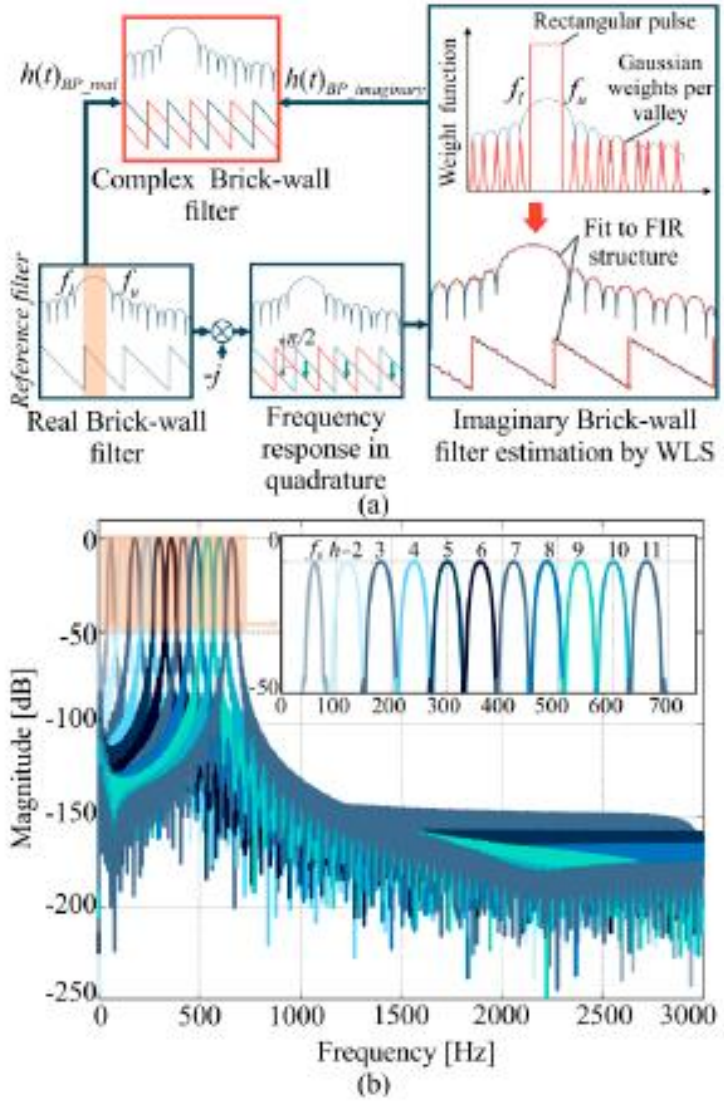

Figure 2. (**a**) Design of a complex brick-wall band-pass finite impulse response (FIR) filter and (**b**) the frequency response of complex brick-wall band-pass FIR filters.

From the outputs of the complex filter, $x(t)_r$ and $x(t)_i$, the instantaneous amplitude can be easily estimated by:

$$A = \frac{1}{\sqrt{2}}\sqrt{x(t)_r^2 + x(t)_i^2} \tag{8}$$

where $x(t)_r$ and $x(t)_i$, are the in-phase and in-quadrature filtered signals. Additionally, a magnitude compensation is carried out when a frequency deviation occurs. This compensation is necessary due to the magnitude frequency response of the filter. In order to reduce the computational burden, a simple Gaussian function *Gc* is proposed for the compensation process. Hence, the compensated magnitude *A*(*t*)*c* is given by:

$$A(t)_c = \frac{A(t)}{Gc} = \frac{A(t)}{e^{-\left(\frac{f(t)-f_0}{\delta}\right)^2}} \tag{9}$$

where f is the instantaneous frequency and δ is a shape parameter of the Gaussian function, which is adjusted according to the magnitude filter attenuation response, using a curve fitting technique in the interest range, this is ±5 Hz around f_0.

On the other hand, the instantaneous phase can be obtained as:

$$\theta(t) = \tan^{-1}\left(\frac{x(t)_i}{x(t)_r}\right) \tag{10}$$

However, the instantaneous phase represents the entire argument of the sinusoidal signal shown in Equation (1), this means that the instantaneous phase is in a rotatory reference frame given by the nominal frequency $2\pi f_0 t$. Therefore, a phase compensation is presented to obtain an adequate phasor representation. It is given by:

$$\theta(t)_{stat} = \theta(t) - 2\pi f_0 t \tag{11}$$

where $\theta(t)_{stat}$ is the phase in a stationary reference frame. This phase value contains the instantaneous frequency deviation term along with the stationary phase. The instantaneous phase is used as argument for the SSB modulation depicted in Figure 3a. A Hilbert FIR filter with a $\pi/2$ phase using an equiripple linear-phase and an order of 600 is proposed to obtain the analytic signal terms, i.e., $x(t)$ and $\hat{x}(t)$. Then, these terms are modulated by a cosine and sine functions (see Figure 3a), respectively, using the inverted instantaneous phase and the harmonic order h; as a result, the frequency shift depicted in Figure 3b is achieved. From this point of view, it is evident that a unit of SSB modulation is required for each harmonic component (see Figure 1). Additionally, it should be pointed out that Equation (5) has to be modified in order to consider the frequency deviation as a time-variant frequency signal; therefore, the instantaneous SSB modulation is computed by:

$$x(t)_{SSB} = x(t)\cos(-2\pi h\int \Delta f\,dt - \phi_h) - \hat{x}(t)\sin(-2\pi h\int \Delta f\,dt - \phi_h) \tag{12}$$

After that, the harmonic phasor estimation is computed by means of a bank of complex band-pass FIR filters, where the magnitude and phase are estimated using Equations (8) and (10). It is important to note that the magnitude compensation is not required for the harmonic components since the SSB modulation centers all the harmonics to each filter, resulting in a 0 dB gain. Nevertheless, harmonic phase estimation does requires both a compensation due to the modulation process and a change of phase reference frame, which is summarized by the following equation (see also Figure 1):

$$\theta(t)_{stat\_h} = \theta(t)_h - h\theta(t)_{stat} - 2\pi h f_0 t \tag{13}$$

where $\theta(t)_h$ is the instantaneous phase of h-th harmonic, the term $h\theta(t)_s$ is the phase introduced by the SSB modulation by considering the harmonic order, and $2\pi h f_0 t$ is the term due to the rotatory reference frame.

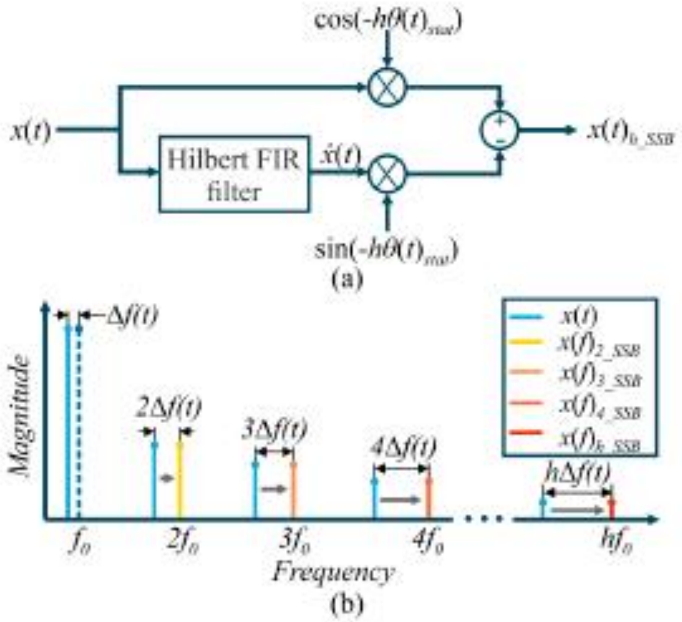

Figure 3. (**a**) Instantaneous SSB modulation diagram and (**b**) the frequency shift for each harmonic component.

For the fundamental frequency estimation (see Figure 1), a derivative process that considers the instantaneous phase component (initial phase and frequency deviation) is used as follows:

$$f(t) = f_0 + \frac{1}{2\pi}\frac{d\theta(t)_{stat}}{dt} \tag{14}$$

In the same way, the instantaneous frequency for harmonic components is obtained by means of the fundamental frequency as follows:

$$f(t)_h = hf(t) \tag{15}$$

The derivative process is based on the proposed algorithm in the IEEE Std. C37.118.1-2011 which is composed by a discrete differential equation [10]. In this regard, the derivative algorithm can be structured into a FIR filter architecture, simplifying its implementation. This filter has the following coefficients $b_k = \{12, -6, -4, -2\}/(20/Fs)$ and can be implemented using a well-known FIR filter structure as follows:

$$y[n] = \sum_{k=0}^{K} b_k x[n-k] \tag{16}$$

where $x[n]$ is the discrete input signal, $y[n]$ is the output signal and K is the filter order. As can be noticed in Figure 1, additional low-pass FIR filters are proposed to smooth the instantaneous phase of the fundamental component, which allows improving the accuracy in the SSB modulation process. Likewise, harmonic frequency components are filtered by a low-pass FIR filter to smooth the derivative process and improve the frequency accuracy. These filters are proposed as triangular filters with an order of 128. This order is selected by trial and error according to its performance and by considering the general delay time. A triangular weighted FIR filter is given by:

$$W(k) = 1 - \frac{2}{N+2}|k| \tag{17}$$

where $k = -N/2{:}N/2$ (integers only) and N is the filter order [10]. Finally, a downsampling process is carried out for the magnitude, phase, and frequency components. This process represents the reporting rate or FPS of the PMU. In this work, a 60 fps is used to assess the proposed algorithm.

4. Results and Discussions

The proposed algorithm is tested using all the benchmark tests proposed by the current synchrophasor IEEE standards: C37.118.1-2011 along with C37.118.1a-2014. All the experimentation is carried out using MATLAB software (The MathWorks, Inc., Natick, MA, USA). Steady-state and dynamic tests are carried to evaluate the accuracy through error parameters such as: TVE, FE, and RFE. As mentioned above, the error limits are extended to harmonic components in the most tests except in the modulation tests where the error boundaries depend on the carrier frequency and some adjustments must be carried out. Additionally, the dynamic behavior is also evaluated using parameters such as response time and delay time along with the overshoot by means of the step response. As the PMU standard is designed for a fundamental synchrophasor, additional issues must be considered, e.g., the signal sampling frequency Fs is set to 6000 Hz which allows analyzing up to 50th harmonic. This condition is also useful for the out-of-band interference test.

For the tests, a synthetic reference signal with 11 harmonic components is proposed, including even and odd harmonics. This number has been chosen by other authors; however, other harmonic phasors can be computed in the proposal by simply adding the corresponding stages (e.g., the SSB stage for a specific harmonic). The magnitude, phase, and frequency parameters of the synthetic signal are listed in Table 1. This table also shows the estimated parameters using the proposal, where very similar values are obtained, indicating a suitable performance. These parameters are obtained in both steady-state and nominal conditions.

Table 1. Harmonic parameters for synthetic signals and estimated parameters by the proposed algorithm.

h	Proposed Parameters			Estimated Parameters		
	A_h [p.u.]	ϕ_h [rad]	hf_c [Hz]	A_h [p.u.]	ϕ_h [rad]	hf_c [Hz]
1	1.000	0.0	60.000	1.000	-6×10^{-11}	60.000
2	0.493	0.0	120.000	0.493	2×10^{-4}	120.000
3	0.510	0.0	180.000	0.510	5×10^{-5}	180.000
4	0.188	0.0	240.000	0.188	-8×10^{-4}	240.000
5	0.375	0.0	300.000	0.375	-1×10^{-4}	300.000
6	0.104	0.0	360.000	0.104	-3×10^{-4}	360.000
7	0.208	0.0	420.000	0.208	1×10^{-4}	420.000
8	0.101	0.0	480.000	0.101	3×10^{-4}	480.000
9	0.202	0.0	540.000	0.202	3×10^{-4}	540.000
10	0.100	0.0	600.000	0.100	-2×10^{-4}	600.000
11	0.200	0.0	660.000	0.200	4×10^{-6}	660.000

After that, the proposal is tested under all the benchmark tests according to the Std. C37.118.1-2011 and C37.118.1a-2014 using TVE, FE, and RFE. These tests include steady-state conditions (a specific parameter changes in a moment of time and then maintains its value) and dynamic conditions (a specific parameter changes overtime).

The TVE is a value which encompasses magnitude and phase accuracy. It is defined as:

$$\mathrm{TVE} = \sqrt{\frac{(x_r' - x_r)^2 + (x_i' - x_i)^2}{{x_r}^2 + {x_i}^2}} \tag{18}$$

where x'_r and x'_i are the estimated values, while x_r and x_i are the theoretical values given by the synthetic signal. Likewise, frequency and ROCOF measurements are evaluated by means of FE and RFE defined by:

$$\mathrm{FE} = \left| f - f' \right| \tag{19}$$

$$\mathrm{RFE} = \left| (df/dt) - (df'/dt) \right| \tag{20}$$

where f and df/dt are the measured values and f' and df'/dt are the true values at the same instant of time. In this work, ROCOF is obtained as the difference between the current values and the past values by dividing the result by Fs.

4.1. Steady-State Tests

4.1.1. Magnitude and Phase Tests

This test consists of evaluating the synchrophasor algorithm under constant changes of magnitude and phase. For the magnitude test, values between 0.1 p.u. to 2 p.u. (per unit) have to be tested [10]. Therefore, the signal under analysis with harmonic content is given by:

$$x(t) = G\sum_{h=1}^{H} A_h \cos(h(2\pi f_0 t + 2\pi \int \Delta f dt) + \phi_h) \tag{21}$$

where G is a gain term that scales the entire signal between 0.1 and 2 as shown in Figure 4a. The TVE values for each harmonic component are also shown. A shaded plane is placed on the TVE graph, denoting the maximum allowable limit by the standard, i.e., 1%. As can be noticed, the TVE values for all harmonics remain far below the TVE boundaries.

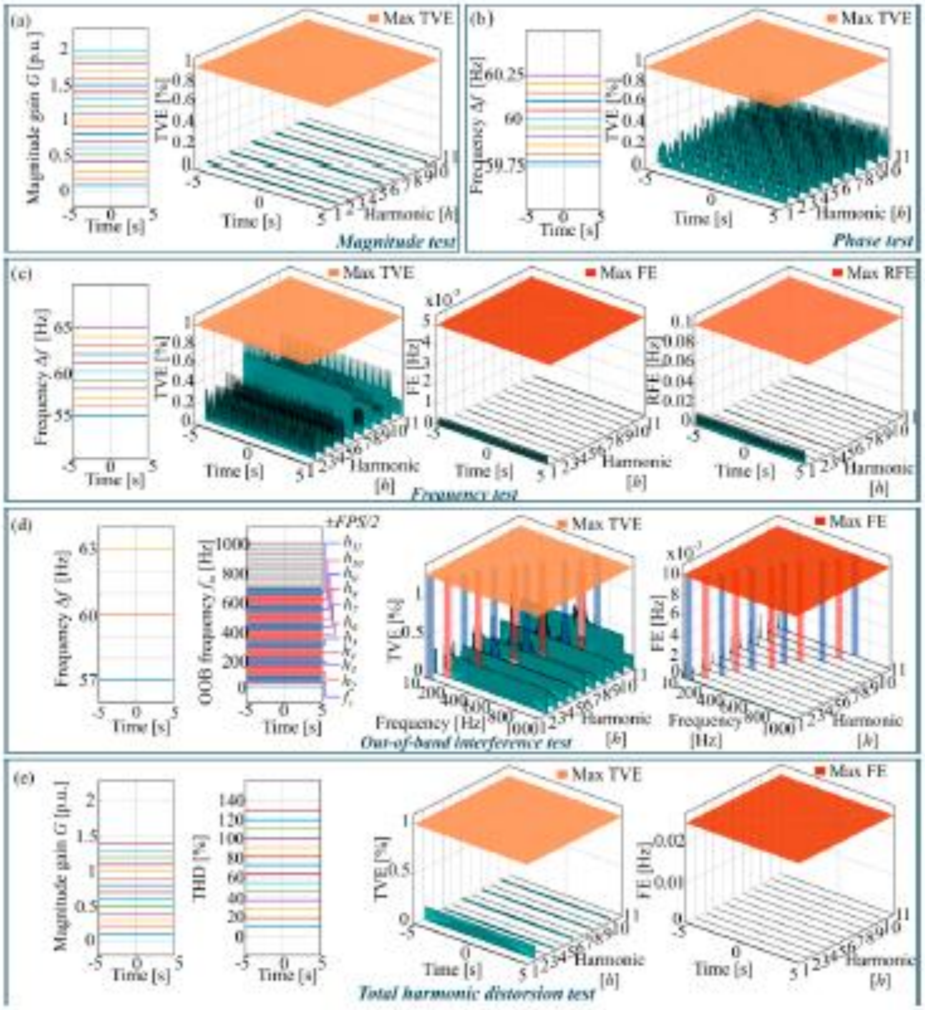

Figure 4. Steady-state tests: (**a**) magnitude test, (**b**) phase test, (**c**) frequency test, (**d**) out-of-band test, and (**e**) total harmonic distortion test.

For the phase test, the change of phase angle is carried out as described in [10] with an input frequency offset $|\Delta f - f_0| < 0.25$ Hz, which produces a slowly varying phase angle of $\pm\pi$. The TVE values for the phase test are below the required limits (see Figure 4b), but an increment in the TVE values according to the harmonic order is observed. This effect is caused because the frequency deviation increases linearly according to the harmonic order.

4.1.2. Frequency Test

This test considers off-nominal frequency values, i.e., $\Delta f = \pm 5$ Hz. The main advantage of the proposed methodology is that the SSB modulation centers the harmonic frequencies in their respective passbands according to the fundamental frequency deviation, allowing an accurate result during the harmonic phasor estimation. TVE, FE, and RFE values are within the admissible levels of the IEEE Std. C37.118.1-2011 and C37.118.1a-2014 as shown in Figure 4c. Although allowable error levels are obtained, it can be noticed that even harmonic components have greater TVE errors than the ones obtained for the odd harmonic components, which is due to changes in the frequency response of the filters.

4.1.3. Out-of-Band (OOB) Interference Test

In this test, the inter-harmonic immunity is evaluated, where frequency deviations of $\Delta f = \pm 0.1(FPS/2) = \pm 3$ Hz are considered. The OOB interference is constructed by adding to the reference signal a set of sinusoidal components with 10% of fundamental magnitude from 10 Hz to 1000 Hz, which represents a greater range (a more realistic condition for harmonics) than the one required by the standard. Hence, the reference signal for this test is:

$$x(t) = \sum_{h=1}^{H} A_h \cos(2\pi h(f_0 t + \int \Delta f\, dt) + \phi_h) + 0.1\sin(2\pi f_{in} t) \tag{22}$$

where f_{in} is the OOB interference frequency. The reported TVE and FE values exclude the Nyquist frequency of the synchrophasor reporting rate, i.e., $\pm FPS/2$ around each component as shown in Figure 4d (blue and red zones). The TVE and FE values are below the limits required by the synchrophasor standard. For the TVE values, high values or peaks close to the Nyquist frequency can be observed but they remain within the required accuracy. It is important to mention that although a frequency deviation along with the OOB interference are evaluated, the SSB modulation and the high rejection of the proposed filters (below 50 dB beyond the Nyquist frequency) allow keeping the required accuracy, knowing that this test is one of the most demanding tests.

4.1.4. Total Harmonic Distortion (THD) Test

For this test, the standard requirements set a 10% of THD. In order to have a wider range of evaluation and by considering the presence of even and odd harmonics, higher values of THD are considered. In the proposed evaluation, the THD variation is proposed by scaling all the harmonic components of the reference signal as follows:

$$x(t) = A_1\cos(2\pi f_0 t + 2\pi\int \Delta f\, dt + \phi_1) + G\sum_{h=2}^{H} A_h \cos(h(2\pi f_0 t + 2\pi \int \Delta f\, dt) + \phi_h) \tag{23}$$

where G is a constant gain that changes from 0.1 to 1.4, producing THD values from 10% to 130% approximately as shown in Figure 4e; as can be noticed, the accuracy of the synchrophasor and frequency is not affected by high levels of THD. Although the limits are not exceeded, even harmonic components have greater error values than the ones obtained for the odd harmonic components, which is similar to the frequency test (Figure 4c).

4.2. Dynamic Tests

4.2.1. Magnitude and Phase Modulation Tests

In this test, bandwidth requirements for synchrophasors are evaluated by means of magnitude or phase modulated signals. These signals are obtained as follows:

$$x(t) = \sum_{h=1}^{H} (A_h(1 + k_x \cos(2\pi f_m)) \cos(2\pi h f_0 t + k_a h \cos(2\pi f_m - \pi)) \tag{24}$$

where k_x is the amplitude modulation factor, k_a is the phase modulation factor, and f_m is the modulation frequency. The magnitude modulation test is performed using $k_x = 0.1$ and $k_a = 0$, and the phase modulation test is performed with $k_x = 0$ and $k_a = 0.1$ as described in the standard. In both cases, the modulation frequency varies from 0.1 Hz to 5 Hz in steps of 0.2 Hz.

Regarding the magnitude modulation test (see Figure 5a), TVE values below 3% are obtained, staying within the allowable ranges. The results for the fundamental component have levels of accuracy close to the maximum TVE limit; however, the FE and RFE values have good performance.

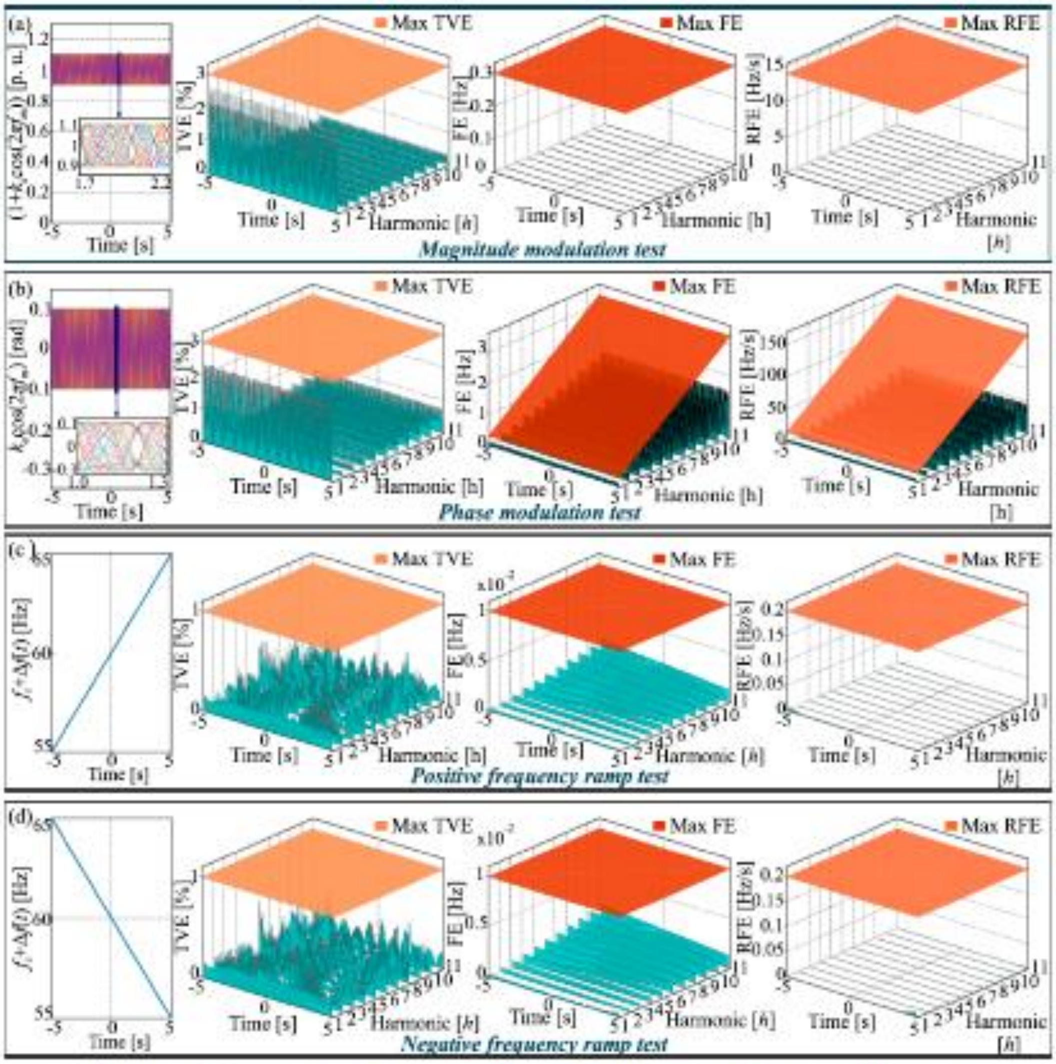

Figure 5. Dynamic tests: (**a**) magnitude modulation test, (**b**) phase modulation test, (**c**) positive ramp test, and (**d**) negative ramp test.

For the phase modulation test, the TVE performance is similar to the one obtained in the magnitude modulation, which is below the maximum allowable TVE value, i.e., 3%. Regarding the frequency and ROCOF results for the phase test, some issues must be considered since the maxima allowable FE and RFE values depend on the modulation frequency values which increase according to the harmonic order. In this regard, as described in the C37.118.1a-2014, the maxima allowable FE and RFE values for harmonic components are set by:

$$\text{Max FE} = 0.06 h f_m \tag{25}$$

$$\text{Max RFE} = 0.18 \pi h {f_m}^2 \tag{26}$$

As shown in Figure 5b, the FE and RFE maxima values are indicated by means of shaded inclined planes where the measurements show values below the boundaries.

4.2.2. Frequency Ramp Test

Dynamic performance during a frequency change is tested with a linear frequency ramp which is constructed using the following equation:

$$x(t) = \sum_{h=2}^{H} A_h \cos(2\pi h f_0 t + \pi h R_f t^2) \tag{27}$$

where R_f is the frequency ramp rate in Hz/s and the frequency range is given by the test duration. The most demanding condition for this test ranges between ±5 Hz. Then, positive and negative frequency ramps are constructed. As shown in Figure 5c, a positive ramp test is carried out from 55 Hz to 65 Hz where TVE, FE, and RFE values are evaluated according to the class M performance. As can be observed, the magnitude, phase, frequency, and ROCOF measurements have the enough accuracy for synchrophasor applications. Likewise, a negative slope ramp is also tested as shown in Figure 5d. In this test, similar error values are obtained, complying with the accuracy requirements for phasor, frequency, and ROCOF.

4.2.3. Magnitude and Phase Step Tests

Step tests are carried out to assess the time performance of synchrophasor, frequency, and ROCOF measurements using parameters such as response time, delay time, and overshoot, whose limits depend on the *FPS* value. The main idea is to produce a step of 10% in the magnitude test and a step of $\pi/18$ in the phase for the phase step. For the measurements of time and overshoot, a set of shifted steps in a constant fraction of the reported interval are used to interleave them, obtaining higher resolutions [10]. The delay time is obtained by measuring the time interval between the zero time of the step input and the 50% of the final value, while the response time is measured by means of the TVE as the time interval that begins when the TVE exceeds the allowable limit and ends when it returns and remains below the limit [10]. Similar to the TVE value, the frequency and ROCOF time responses are measured using the FE and RFE values. Regarding the overshoot, it is measured as a percentage between the maximum value and the final value. A more detailed description of the aforementioned parameters can be found in [10].

The results for the magnitude and phase tests are summarized in Table 2, where the step test is applied to each harmonic by considering a 10% of magnitude and $\pi/18$ rad of phase step. In the magnitude step tests, the maximum response time is 0.0594 s for the fundamental component which is below the allowed value for 60 *FPS* (0.116 s). The maximum delay time is 0.00077 s measured for the 11th harmonic component, it is also below the allowable limit (0.004166 s); besides that, overshoot values below 1.140% are obtained for the magnitude step tests. In the cases of frequency and ROCOF response times, the maxima times are measured in the 11th harmonic component, 0.1416 s and 0.1574 s, respectively. For the phase tests, the maximum response time is achieved by the 11th harmonic component (0.10400 s) which is close to the maximum allowable limit. Delay time in the phase step test shows a behavior within the limits with a maximum delay time of 0.0001 s, which is obtained for the fundamental component. In the overshoot measurements for the phase step tests, some drawbacks can be observed since the 4th, 6th, and 8th harmonic components exceed the overshoot percentage with values of 11.25%, 14.21%, and 11.82%, respectively. Nevertheless, these drawbacks are present only for even components while odd components have values below 5.41%. Requirements for frequency and ROCOF time responses are completely accomplished with maxima values of 0.1746 s and 0.1594 s, respectively, obtained for the 11th harmonic component. Finally, although an increment in the response time for frequency and ROCOF values can be noticed for the magnitude and phase step tests according to the harmonic order, the limits are not exceeded; in fact, they are far below the allowed limits, hence, the number of harmonics to be measured can be extended.

Table 2. Magnitude and phase tests results for each harmonic component.

	Magnitude Step Test					**Phase Step Test**				
h	**Response Time (Max. 7/FPS)**	**Delay Time (Max. 1/(4FPS))**	**Overshoot (Max. 10%)**	**Frequency Response Time (Max. 14/f_0)**	**ROCOF Response Time (Max. 14/f_0)**	**Response Time (Max. 7/FPS)**	**Delay Time (Max. 1/(4FPS))**	**Overshoot (Max. 10%)**	**Frequency Response Time (Max. 14/f_0)**	**ROCOF Response Time (Max. 14/f_0)**
1	0.0594 s	0.00018 s	0.022%	0.0874 s	0.0190 s	0.06960 s	0.0001000 s	0.00%	0.1292 s	0.1456 s
2	0.0342 s	0.00018 s	0.550%	0.1189 s	0.1035 s	0.06940 s	0.0000520 s	6.26%	0.1383 s	0.1546 s
3	0.0340 s	0.00022 s	0.290%	0.1212 s	0.1328 s	0.09420 s	0.0000590 s	4.55%	0.1396 s	0.1563 s
4	0.0385 s	0.00027 s	0.950%	0.1219 s	0.1374 s	0.10000 s	0.0000120 s	* 11.25%	0.1401 s	0.1572 s
5	0.0342 s	0.00033 s	0.260%	0.1225 s	0.1382 s	0.09920 s	0.0000560 s	4.39%	0.1411 s	0.158 s
6	0.0448 s	0.00044 s	1.140%	0.1265 s	0.1386 s	0.10140 s	0.0000006 s	* 14.21%	0.1416 s	0.1584 s
7	0.0350 s	0.00051 s	0.270%	0.1347 s	0.1390 s	0.10090 s	0.0000270 s	5.41%	0.1535 s	0.1586 s
8	0.0362 s	0.00062 s	0.680%	0.1408 s	0.1430 s	0.10220 s	0.0000007 s	* 11.82%	0.1688 s	0.1589 s
9	0.0348 s	0.00068 s	0.250%	0.1408 s	0.1517 s	0.10240 s	0.0000550 s	4.43%	0.1714 s	0.1591 s
10	0.0359 s	0.00074 s	0.630%	0.1412 s	0.1561 s	0.10370 s	0.0000021 s	8.59%	0.1734 s	0.1592 s
11	0.0351 s	0.00077 s	0.260%	0.1416 s	0.1574 s	0.10400 s	0.0000650 s	4.16%	0.1746 s	0.1594 s

* Values that exceed the allowable limits.

4.3. *Comparison with Previous Works*

As aforementioned some strategies have been reported for phasor harmonic estimation with PMU capabilities, which are summarized in Table 3. These strategies are based on FFT [2,12], adaptive filters [9], and model-based estimation [19]. It is important to mention that the current methods require additional frequency tracking algorithms for an accurate estimation when off-nominal frequencies are present, unlike the proposed work where the frequency is estimated by means of the proposed algorithm. On the other hand, different tests must be carried out to evaluate the robustness under different static and dynamic conditions that can occur in real scenarios; however, not all works consider the different possible conditions, such as in [2,12]. Regarding the harmonic estimation, different harmonic orders and reporting rates are analyzed; nevertheless, odd and even harmonics are only considered in [9] and the proposed work. Although the proposal only analyzes up to the 11th harmonic, the computation of a higher number of harmonics requires simply to add the stages related to the harmonic components as shown in Figure 1. In fact, the proposal can be configured to compute specific harmonic phasors according to the user application, e.g., protection and control schemes for some odd harmonics. Finally, although there is no guidelines for harmonic phasor estimation oriented to PMU applications, different error criteria are used to assess the performance of the proposed methodologies, where the proposed work uses all the benchmark tests and accuracy requirements indicated in the current synchrophasor standard.

Table 3. Comparative summary between the proposed method and other related works.

Work	Methodology	Additional Frequency Tracking	Static Test Validation	Dynamic Test Validation	Harmonics under Test	PMU Reporting Frequency (FPS)	Reported Error Values
[2]	1. Signal decimation. 2. Apply window to signal. 3. Apply FFT for synchrophasor estimation. 4. Compensation for off-nominal frequencies	Yes	Yes	No	3, 5, 7, and 9	10	1. TVE2. Standard deviation
[9]	1. Adaptive filter bank (FIR, Kalman and SFFT) for each harmonic component. 2. Phasor estimation.	Yes	Yes	Yes	2, 3, 4, 5, 6, 7, 8, 9, 10, 11	60	1. Magnitude Error. 2. Frequency error. 3. THDerror
[12]	1. Apply window to signal.2. Apply FFT for synchrophasor estimation.	Yes	Yes	No	3, 5, 7, 9	10	-
[19]	1. Vector state model estimation. 2. Frequency tracking for compensation. 3. Harmonic phasor estimation	Yes	Yes	Yes	3, 5	-	1. TVE
This work	1. Fundamental phasor and frequency estimation through a complex filter. 2. Instantaneous SSB modulation to center the harmonic component. 3. Harmonic phasor estimation.	No	Yes	Yes	2, 3, 4, 5, 6, 7, 8, 9, 10, 11	60	1. TVE 2. FE 3. RFE 4. Response time 5. Delay time 6. Overshoot

- Not reported values.

5. Conclusions

A new algorithm for phasor and frequency estimation of fundamental and harmonic components is assessed through the current synchrophasor standards, i.e., the Std. C37.118.1-2011 along with Std. C37.118.1a-2014. The proposed algorithm is based on complex brick-wall FIR filters which are designed at the nominal frequencies for fundamental and harmonic components, while the instantaneous SSB modulation technique is used to shift the harmonic frequency component according to the instantaneous frequency deviation, shifting the signal to the center of each complex FIR filter.

The proposed filters show that are reliable enough to accomplish with the PMU standards due to their high rejection in the stop band, linear phase behavior, and fast response time. Additionally, the main advantage of the proposal is that additional algorithms for frequency tracking are not required as the case of the most harmonic phasor estimation algorithms reported in the literature, which implies a complexity reduction. It is worth noting that even and odd harmonic components are considered in the analysis, which is not always studied in the works proposed for the harmonic phasor estimation.

The fulfillment of all the dynamic and steady-state tests stated in the PMU standard is achieved, taking as a reference the limits for the fundamental phasor; yet, some issues must be considered. Firstly, in the phase modulation test, the maxima allowable limits are modified according to the harmonic order since the phase modulation affects the frequency components related to the allowed maximum error. Secondly, although some overshoot values are out of range in the phase step tests for some even harmonic components, the time performance still has admissible results and they do not affect the estimation accuracy. Finally, the proposed algorithm is tested for eleven components but it could be extended for more harmonic components easily.

In a future work, the proposal will be implemented using the FPGA technology, exploiting its parallelism. This implementation will allow providing a system-on-a-chip (SoC) solution for PMU applications in power systems.

Author Contributions: Conceptualization: A.M.-B., D.G.-L. and M.V.-R.; data curation and formal analysis: A.M.-B. and J.R.R.-H.; funding acquisition: J.P.A.-S. and M.V.-R.; methodology, A.M.-B. and D.G.-L.; investigation, resources, and visualization: J.R.R.-H. and J.P.A.-S.; writing—original draft, review, and editing: all authors.

Funding: This research was funded by the "Consejo Nacional de Ciencia y Tecnologia (CONACYT)" under scholarship 296868 and the "Programa para el Desarrollo Profesional Docente (PRODEP), para el tipo Superior de México".

Conflicts of Interest: The authors declare no conflicts of interest.

References

1. Jain, S.K.; Singh, S.N. Harmonics estimation in emerging power system: Key issues and challenges. *Electr. Power Syst. Res.* **2011**, *81*, 1754–1766. [CrossRef]
2. Carta, A.; Locci, N.; Muscas, C. A PMU for the measurement of synchronized harmonic phasors in three-phase distribution networks. *IEEE Trans. Instrum. Meas.* **2009**, *58*, 3723–3730. [CrossRef]
3. Ye, G.; Xiang, Y.; Cuk, V.; Cobben, J.F.G. Harmonic disturbance location by applying Bayesian inference. *Electr. Power Syst. Res.* **2016**, *140*, 886–894. [CrossRef]
4. Valtierra-Rodriguez, M.; Granados-Lieberman, D.; Torres-Fernandez, J.E.; Rodriguez-Rodriguez, J.R.; Gómez-Aguilar, J.F. A new methodology for tracking and instantaneous characterization of voltage variations. *IEEE Trans. Instrum. Meas.* **2016**, *65*, 1596–1604. [CrossRef]
5. Messina, F.; Marchi, P.; Rey Vega, L.; Galarza, C.; Laiz, H. A novel modular positive-sequence synchrophasor estimation algorithm for PMUs. *IEEE Trans. Instrum. Meas.* **2017**, *66*, 1164–1175. [CrossRef]
6. Shaik, A.G.; Mahela, O.P. Power quality assessment and event detection in hybrid power system. *Electr. Power Syst. Res.* **2018**, *161*, 26–44. [CrossRef]
7. Razo-Hernandez, J.R.; Valtierra-Rodriguez, M.; Amezquita-Sanchez, J.P.; Granados-Lieberman, D.; Gomez-Aguilar, J.F.; Rangel-Magdaleno, J.J. Homogeneity-PMU-based method for detection and classification of power quality disturbances. *Electronics* **2018**, *7*, 433. [CrossRef]
8. Chen, C.I.; Chen, Y.C. Comparative study of harmonic and interharmonic estimation methods for stationary and time-varying signals. *IEEE Trans. Ind. Electron.* **2014**, *61*, 397–404. [CrossRef]
9. Chakir, M.; Kamwa, I.; Le Huy, H. Extended C37.118.1 PMU algorithms for joint tracking of fundamental and harmonic phasors in stressed power systems and microgrids. *IEEE Trans. Power Deliv.* **2014**, *29*, 1465–1480. [CrossRef]
10. IEEE Std C37.118.1-2011. *IEEE Standard for Synchrophasor Measurements for Power Systems*; IEEE Inc.: New York, NY, USA, 2011.
11. IEEE Standard C37.118.1a-2014. *IEEE Standard for Synchrophasor Measurements for Power Systems-Amendment 1: Modification of Selected Performance Requirements, (Amendment to IEEE Standard C37.118.1-2011)*; IEEE Inc.: New York, NY, USA, 2014.
12. Carta, A.; Locci, N.; Muscas, C. GPS-based system for the measurement of synchronized harmonic phasors. *IEEE Trans. Instrum. Meas.* **2009**, *58*, 586–593. [CrossRef]
13. Aminifar, F.; Fotuhi-Firuzabad, M.; Safdarian, A.; Davoudi, A.; Shahidehpour, M. Synchrophasor measurement technology in power systems: Panorama and state-of-the-art. *IEEE Access* **2014**, *2*, 1607–1628. [CrossRef]
14. Nanda, P.; Panigrahi, C.K.; Dasgupta, A. Phasor Estimation and Modelling Techniques of PMU—A Review. *Energy Procedia* **2017**, *109*, 64–77. [CrossRef]
15. Rocha, R.V.; Coury, D.V.; Monaro, R.M. Recursive and non-recursive algorithms for power system real time phasor estimations. *Electr. Power Syst. Res.* **2017**, *143*, 802–812. [CrossRef]
16. Wang, M.; Sun, Y. A practical, precise method for frequency tracking and phasor estimation. *IEEE Trans. Power Deliv.* **2004**, *19*, 1547–1552. [CrossRef]
17. Akke, M.; Thorp, J.S. Sample value adjustment improves phasor estimation at off-nominal frequencies. *IEEE Trans. Power Deliv.* **2010**, *25*, 2255–2263. [CrossRef]
18. Zeng, B.; Teng, Z.; Cai, Y.; Guo, S.; Qing, B. Harmonic phasor analysis based on improved FFT algorithm. *IEEE Trans. Smart Grid* **2011**, *2*, 51–59. [CrossRef]
19. Chen, C.I. A phasor estimator for synchronization between power grid and distributed generation system. *IEEE Trans. Ind. Electron.* **2013**, *60*, 3248–3255. [CrossRef]

20. Sadinezhad, I.; Agelidis, V.G. Real-time power system phasors and harmonics estimation using a new decoupled recursive-least-squares technique for DSP implementation. *IEEE Trans. Ind. Elect.* **2013**, *60*, 2295–2308. [CrossRef]
21. Ferrero, R.; Pegoraro, P.A.; Toscani, S. Dynamic fundamental and harmonic synchrophasor estimation by Extended Kalman filter. In Proceedings of the 2016 IEEE International Workshop on Applied Measurements for Power Systems (AMPS), Aachen, Germany, 28–30 September 2016; pp. 1–6. [CrossRef]
22. Liu, J.; Ni, F.; Pegoraro, P.A.; Ponci, F.; Monti, A.; Muscas, C. Fundamental and harmonic synchrophasors estimation using modified Taylor-Kalman filter. In Proceedings of the IEEE International Workshop on Applied Measurements for Power Systems (AMPS), Aachen, Germany, 26–28 September 2012; pp. 1–6. [CrossRef]
23. Jain, S.K.; Jain, P.; Singh, S.N. A fast harmonic phasor measurement method for smart grid applications. *IEEE Trans. Smart Grid* **2017**, *8*, 493–502. [CrossRef]
24. Razo-Hernandez, J.R.; Valtierra-Rodriguez, M.; Granados-Lieberman, D.; Tapia-Tinoco, G.; Rodriguez-Rodriguez, J.R. A phasor estimation algorithm based on Hilbert transform for P-class PMUs. *Adv. Electr. Comput. Eng.* **2018**, *18*, 97–104. [CrossRef]
25. Lee, Y.; Song, H. Decentralized load shedding method based on voltage stability margin index using synchrophasor measurement technology. *Electronics* **2018**, *7*, 277. [CrossRef]
26. Augusto-Duque, C.; Silveira, P.M.; Ribeiro, P.F. Visualizing time-varying harmonics using filter banks. *Electr. Power Syst. Res.* **2011**, *81*, 974–983. [CrossRef]
27. Urbina-Salas, I.; Razo-Hernandez, J.R.; Granados-Lieberman, D.; Valtierra-Rodriguez, M.; Torres-Fernandez, J.E. Instantaneous power quality indices based on single-sideband modulation and wavelet packet-Hilbert transform. *IEEE Trans. Instrum. Meas.* **2017**, *66*, 1021–1031. [CrossRef]
28. Roscoe, A.J.; Abdulhadi, I.F.; Burt, G.M. Filters for M class phasor measurement units. In Proceedings of the IEEE International Workshop on Applied Measurements for Power Systems (AMPS), Aachen, Germany, 26–28 September 2012; pp. 1–6. [CrossRef]